

**INFRARED PLANAR LASER-INDUCED
FLUORESCENCE IMAGING
AND APPLICATIONS TO IMAGING OF CARBON
MONOXIDE AND CARBON DIOXIDE**

Report no. TSD-140

Brian J. Kirby

June 2001

**INFRARED PLANAR LASER-INDUCED
FLUORESCENCE IMAGING
AND APPLICATIONS TO IMAGING OF CARBON
MONOXIDE AND CARBON DIOXIDE**

Report no. TSD-140

Brian J. Kirby

June 2001

© Copyright by Brian J. Kirby 2001
All Rights Reserved

I certify that I have read this dissertation and that in my opinion it is fully adequate, in scope and quality, as a dissertation for the degree of Doctor of Philosophy.

Ronald K. Hanson
(Principal Adviser)

I certify that I have read this dissertation and that in my opinion it is fully adequate, in scope and quality, as a dissertation for the degree of Doctor of Philosophy.

Christopher F. Edwards

I certify that I have read this dissertation and that in my opinion it is fully adequate, in scope and quality, as a dissertation for the degree of Doctor of Philosophy.

Jay B. Jeffries

Approved for the University Committee on Graduate Studies:

Abstract

This dissertation introduces infrared planar laser-induced fluorescence (IR PLIF) techniques for visualization of species that lack convenient electronic transitions and are therefore unsuitable for more traditional electronic PLIF measurements. IR PLIF measurements can generate high signal levels that scale linearly with both laser energy and species concentration, thereby demonstrating advantages over Raman and multiphoton PLIF techniques.

IR PLIF is shown to be a straightforward and effective tool for visualization of CO and CO₂ in reactive flows. The slow characteristic times of vibrational relaxation and the large mole fractions of CO and CO₂ in typical flows lead to high IR PLIF signal levels, despite the low emission rates typical of vibrational transitions. Analyses of rotational energy transfer (RET) and vibrational energy transfer (VET) show that excitation schemes in either linear (weak) or saturated (strong) limits may be developed, with the fluorescence collected directly from the laser-excited species or indirectly from bath gases in vibrational resonance with the laser-excited species. Use of short ($\sim 1 \mu\text{s}$) exposures (for CO) or short exposures combined with long-pulse, high-pulse-energy excitation (for CO₂) minimizes unwanted signal variation due to spatially-dependent VET rates.

Results are presented for flows ranging from room-temperature mixing to a benchmark CH₄ laminar diffusion flame. Linear excitation is appropriate for CO due to its slow vibrational relaxation. However, linear excitation is not well-suited for CO₂ imaging due to fast H₂O-enhanced VET processes and the attendant difficulty in interpreting the resulting signal. Saturated excitation using a CO₂ laser (or combined CO₂ laser-OPO) technique is most appropriate for CO₂, as it generates high signal and minimizes spatial variations in fluorescence quantum yield.

Since IR PLIF is applicable to most IR-active species, it has a high potential for expanding the diagnostic possibilities available to combustion researchers. Such diagnostics might include visualization of the fuel region of lifted flames, CO-formation regions in flames, or exhaust mixing processes in internal combustion engines as applied to residual-induced autoignition.

Acknowledgements

It is my pleasure to acknowledge the support and guidance of my primary advisor, Professor Ronald K. Hanson, who provided direction, encouragement, and insight for all aspects of this work. His creative ideas, sound critical thinking, and effort serves as a model for all of his students. His imprint on this research is clear.

I wish also to thank the members of the reading committee, Professor Christopher F. Edwards and Dr. Jay B. Jeffries, for useful suggestions regarding the text, as well as Professor M. Godfrey Mungal and Professor Robert L. Byer for their service on the examination committee. Jay Jeffries, in particular, was kind enough to read the very roughest drafts of this thesis; his patient and thorough guidance has been invaluable.

This research has been enhanced in innumerable ways by the students and staff at Stanford. Particular mention is due to Dr. Mark C. Thurber and Dr. Michael E. Webber, who were a constant source of advice and support throughout.

This research was supported by the Air Force Office of Scientific Research, with equipment funding from the Office of Naval Research.

Contents

Abstract	iv
Acknowledgements	vi
1 Introduction	1
1.1 Motivation	1
1.2 Thesis Scope and Overview	4
2 IR PLIF of Carbon Monoxide	5
2.1 Introduction	5
2.2 Experimental Setup and Techniques	6
2.3 Fluorescence Equation	8
2.4 Excitation Schemes	9
2.4.1 Absorption	11
2.4.2 Fluorescence	19
2.4.3 Sensitivity	28
2.5 Imaging Results	29
2.6 Conclusions: IR PLIF of CO	32
3 IR PLIF of Carbon Dioxide	35
3.1 Introduction	35
3.2 Linear Excitation Schemes	36
3.2.1 Notation	36
3.2.2 Excitation Schemes	36

3.2.3	Absorption	37
3.2.4	Fluorescence	38
3.2.5	Imaging Results—Linear Excitation	40
3.3	Saturated Excitation Schemes	40
3.3.1	CO ₂ Vibrational Manifold: Saturated Excitation	44
3.3.2	Characteristic Rates	45
3.3.3	Three-Temperature Model	47
3.3.4	Experimental Setup and Techniques: Saturated Excitation	53
3.3.5	Imaging Results—Saturated Excitation	55
3.3.6	Temperature-Independent Excitation Scheme	60
3.4	Conclusions: IR PLIF of CO ₂	63
4	Indirect Excitation Schemes	65
4.1	Introduction	65
4.2	Theory	67
4.2.1	Linear Excitation Schemes	68
4.2.2	Saturated Excitation	70
4.3	Results	71
4.3.1	Room-Temperature Mixing	71
4.3.2	Fuel-Product Overlap in a CO/Ar/H₂ flame	73
4.4	Conclusions: Indirect Excitation Schemes	74
5	Conclusions and Future Work	76
5.1	Future Work: extending IR PLIF to other species	76
5.1.1	IR PLIF of Methane	77
5.1.2	IR PLIF of Large Hydrocarbons	80
5.1.3	IR PLIF of Water	81
5.2	Future Work: IR PLIF in Varying Environments	81
5.2.1	Varying Pressures	82
5.2.2	Windows	83
5.2.3	Hot Surfaces	83
5.3	Conclusions	84

5.4	Summary of Results	87
A	IR PLIF Instrumentation	88
A.1	Infrared Imaging Test Bed	88
A.2	Nd:YAG-pumped OPO/OPA Tunable Infrared Source	89
A.2.1	System Overview	89
A.2.2	Nd:YAG Pumping	90
A.2.3	In-house modifications	91
A.2.4	OPO Performance Diagnostics	91
A.2.5	Alignment Techniques	92
A.2.6	OPO Performance–pulse energy	94
A.3	CO ₂ Laser	95
A.4	Infrared Cameras	96
A.4.1	Camera Timing	97
A.4.2	Camera Noise Performance	97
A.4.3	Camera Calibration	98
A.4.4	Camera Temporal Response	98
A.4.5	Camera Resolution	100
A.4.6	Collection Optics	100
A.5	IR Detectors	101
A.6	DAQ System	101
B	Rotational Energy Transfer	102
B.1	Introduction	102
B.2	Rotational States and Notation	102
B.3	RET processes	103
B.3.1	Elastic Dephasing	103
B.3.2	R-T Transfer	103
B.3.3	R-R Transfer	103
B.3.4	Relative significance of RET mechanisms	104
B.4	Relation between RET and Spectroscopic Parameters	104
B.5	RET Scaling Models	106

B.5.1	Modified Exponential-Gap	106
B.5.2	Energy-Corrected Sudden	107
B.6	Integration Technique and Scaling Law Parameters	107
C	Vibrational Energy Transfer	109
C.1	Introduction	109
C.2	Vibrational Manifolds and Notation	109
C.3	VET processes	111
C.3.1	V-T equilibration	112
C.3.2	Intermodal V-V equilibration	112
C.3.3	Intramodal V-V equilibration	112
C.3.4	Intermolecular V-V equilibration	113
C.4	VET model, Integration Technique	113
C.4.1	Thermodynamic Database	113
C.4.2	Initial Condition	114
C.4.3	Energy Transfer Rates and CHEMKIN	114
C.4.4	Vibrational Energy Base Transfer Rates	115
C.4.5	Vibrational Energy Transfer Rates—Curve Fits	119
C.4.6	Integration and Fluorescence Yield Calculation	119
	References	121

List of Tables

3.1	Acceptable fluence (< 10% error) shown for several CO ₂ excitation schemes at 1500 K.	38
5.1	Material properties for several optical materials.	83
B.1	MEG parameters for several gas mixtures.	108
C.1	Base rates for various V-T energy transfer processes.	120
C.2	Base rates for various V-V energy transfer processes.	120

List of Figures

1.1	Comparison of signal levels for IR PLIF as compared to Raman imaging for 1 atm pure CO.	3
2.1	Typical IR PLIF experimental setup.	6
2.2	Filtering properties of a cold CO gas filter.	10
2.3	Four-level model for analysis of pulsed excitation with rotational energy transfer.	13
2.4	Population fractions as a function of time for the four-level RET model. . .	15
2.5	Comparison of computational results and experimental measurements of LIF as a function of characteristic fluence.	17
2.6	Acceptable fluence shown as a function of temperature for 2ν excitation of CO.	18
2.7	CO excitation/collection scheme.	19
2.8	VET rates for model four-level system.	20
2.9	Characteristic times for vibrational energy transfer for CO as a function of temperature and collision partner.	25
2.10	Parametric effects on fluorescence quantum yield for CO.	26
2.11	Product of absorption cross section and fluorescence quantum yield for CO.	27
2.12	Calculated fluorescence signal as compared to noise levels for IR PLIF of CO.	28
2.13	Single-shot IR PLIF images of a CO vortex ring.	30
2.14	IR PLIF of turbulent CO/Ar jet in CO/Ar/N ₂ coflow.	31
2.15	CO/Ar/H ₂ flame and imaged region.	32
2.16	IR PLIF image of CO in the fuel region of a laminar diffusion flame.	33

3.1	Energy transfer processes which occur during laser excitation for 2.0 μm excitation of CO_2	37
3.2	Predicted CO_2 fluorescence quantum yield for linear excitation as a function of H_2O and CO_2 mole fraction.	39
3.3	CO_2 absorption cross section as a function of pumped line and temperature.	40
3.4	Single-shot IR PLIF images of CO_2 vortex rings.	41
3.5	Vibrational manifold showing energy transfer processes for CO_2 during and after laser excitation at 10.6 μm	43
3.6	Important energy transfer rates as a function of temperature for CO_2	45
3.7	Predictions of the three-temperature model for the laser-pumped ν_3 mode temperature (T_3^* , [K]) and the fluorescence yield (ψ_{sat} , [photons per million CO_2 molecules]) as a function of initial temperature	51
3.8	Comparison of LIF signal levels at constant CO_2 mole fraction as predicted by two models.	52
3.9	Effects of CO_2 and H_2O mole fraction on IR PLIF signal.	54
3.10	Experimental setup for saturated IR LIF PLIF measurements.	55
3.11	CO_2 IR PLIF imaging of an unsteady transverse 425 K CO_2 jet in an air coflow.	56
3.12	CO_2 IR PLIF imaging in a CO/H_2 flame.	57
3.13	Species mole fractions and temperature in a lifted $\text{CH}_4\text{-N}_2$ laminar diffusion flame.	59
3.14	Predictions for CO_2 fluorescence yield in a laminar diffusion flame.	60
3.15	Comparison between IR PLIF, Raman, and computed images of CO_2 mole fraction in a lifted laminar diffusion flame.	61
3.16	Comparison between IR PLIF, Raman, and computed data for CO_2 mole fraction in a lifted laminar diffusion flame.	61
3.17	Combined OPO- CO_2 laser excitation scheme.	62
3.18	LIF signal at constant CO_2 mole fraction as a function of temperature for two excitation schemes.	63

4.1	Simplified energy diagram of relevant energy transfer processes that affect PLIF signal following indirect excitation.	67
4.2	VET rates for model four-level system.	69
4.3	Single-shot IR PLIF images of CO/CO ₂ vortex rings.	72
4.4	Jet mixing visualized using excitation of CO and fluorescence from CO ₂	73
4.5	Images of fuel and fuel-product overlap in a CO/H ₂ flame.	74
5.1	Calculated CO and CH ₄ absorption spectra near 2.3 μm at 1 atm.	77
5.2	Calculated CH ₄ absorption spectra near 3.3 μm at 1 atm.	78
5.3	CH ₄ energy level diagram with laser excitation and fluorescence collection.	79
5.4	Predicted CH ₄ detectivity limits.	79
A.1	Tunable infrared excitation source.	89
A.2	Optimized output power for modified OPO system.	95
A.3	Typical CO ₂ laser pulse shape.	96
A.4	Camera temporal response.	99

Chapter 1

Introduction

1.1 Motivation

Planar laser-induced fluorescence (PLIF)[?, 1] is a non-intrusive, *in-situ*, optical diagnostic that can remotely image a selected molecular species in a fluid flow. Laser light is tuned spectrally to an absorption line of the molecular species, shaped geometrically into a thin sheet, and used to excite molecular transitions in the illuminated plane; fluorescence is then collected by a camera, interrogating the two-dimensional distribution of a molecular parameter. PLIF is a particularly attractive combustion flowfield imaging diagnostic owing to the strength of the fluorescence process, its species-selectivity, and its ability to provide spatially and temporally resolved, two-dimensional information. Because of this, PLIF has been successfully employed using electronic transitions in the visible and ultraviolet regions to visualize a variety of flow parameters, including species concentration [2], temperature [3], velocity [citepaul89], pressure [4], and reaction rate [5]. Much of this work has been summarized in a number of reviews [1, 6, 7]. Two-dimensional interrogation of these field properties can be used to evaluate mixing processes in subsonic [8] and supersonic [9] flowfields, visualize shocks [10], identify fuel [11] and reaction [12] zones in flames, and quantify heat release [13] and combustion-related toxin formation [14] in flames.

Because previous PLIF measurements have used UV or visible laser light to excite electronic transitions in molecules and collect UV or visible light associated with electronic fluorescence, PLIF techniques have historically been implemented only when the electronic

transitions of the interrogated species are compatible with available laser sources and CCD cameras. Fortunately, the UV spectra of many important combustion molecules such as OH [15], CH [12], NO [16], and O₂ [17] are compatible with common pulsed excimer laser, dye laser, or OPO systems, and PLIF imaging diagnostics have been developed to investigate these species.

In contrast, electronic PLIF measurements are not well suited for most combustion fuels and all of the primary combustion products (CO₂, H₂O, H₂, and CO), since they possess single-photon absorption transitions only in the vacuum ultraviolet. Because spatially resolved visualization of these species is so crucial, yet traditional PLIF diagnostics are not feasible, many attempts have been made to image these species using other techniques. Such efforts have included Raman scattering [18], Rayleigh scattering [19], multiphoton PLIF [20], laser-induced polarization anisotropy (polarization spectroscopy) [21], or degenerate four-wave mixing [22]. While these techniques have in some cases experienced limited success, in general none of these diagnostics has found widespread use due to fundamental limitations: Raman scattering is weak and generates low signal levels which are typically unsuitable for imaging; Rayleigh scattering is, in general, not species-selective; multiphoton absorption is weak, responds nonlinearly to laser power, and typically induces predissociative transitions; and laser-induced polarization anisotropy and DFWM, while successful for point measurements, typically do not scale successfully for planar imaging. A notable exception to this is multiphoton PLIF of CO, which has been used with some success for point measurements [23] and imaging [24] of CO in flames. However, of prominent combustion fuels and products (*e.g.*, CH₄, CO, CO₂, H₂O), CO is the only molecule with a non-predissociative multiphoton transition, and the multiphoton PLIF strategies developed for CO have not found widespread use for other species.

In contrast to UV/visible imaging diagnostics, for which the experimental tools had become mature as early as 1990, infrared imaging diagnostics have undergone rapid evolution in recent years, due primarily to improvements in performance of infrared focal plane arrays (FPAs). Improved FPAs, combined with more robust infrared nonlinear optical crystals and low-divergence pulsed pump lasers, have made it possible to consider extending planar laser-induced fluorescence (PLIF) imaging diagnostics to the infrared.

By using infrared lasers and cameras, PLIF imaging diagnostics using vibrational transitions for all infrared-active species become feasible. While there are challenges associated with the use of infrared transitions (most notably, the fluorescence emission rates in the infrared are low), many opportunities are afforded by modifying PLIF techniques to use infrared transitions. In this form, infrared planar laser-induced fluorescence (IR PLIF) [25, 26] uses an infrared laser source to excite vibrational transitions and an infrared camera to image the resulting vibrational fluorescence.

This dissertation will demonstrate that IR PLIF has advantages over Raman [18] and multiphoton PLIF [20, 27, 28] for imaging species that lack convenient UV transitions, because IR PLIF measurements can generate high signal levels that scale linearly with both laser energy and species concentration. For example, Figure 1.1 shows that signal levels for CO imaging using IR PLIF techniques exceed those using Raman techniques by several orders of magnitude. This dissertation presents initial results for atmospheric-pressure flows

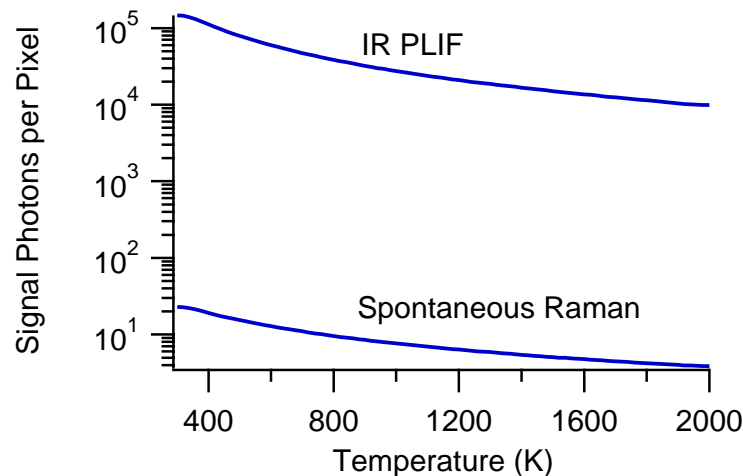


Figure 1.1: Comparison of signal levels for IR PLIF as compared to Raman imaging for 1 atm pure CO. $f/2$ optics; 4 cm \times 4 cm FOV; 1 cm sensor array; 70% filter throughput. For IR PLIF: 12 mJ@2.35 μ m, 85% quantum efficiency, 1 μ s exposure time; for Raman: 2 J@532 nm, 30% quantum efficiency.

using the first infrared (IR) PLIF diagnostics for CO and CO₂, the first detailed analysis of excitation schemes for these species, the first results using saturated laser excitation, and the

first techniques that use combined laser/VET pumping schemes. These diagnostic developments enable single-shot visualization of these species in a manner not before possible. Since IR PLIF is, in principle, applicable to all IR-active species, IR PLIF has high potential for expanding the diagnostic possibilities available to combustion researchers, which might include visualization of the preflame (fuel) region of lifted flames, CO formation regions in flames, or exhaust mixing processes in internal combustion engines.

1.2 Thesis Scope and Overview

The primary goals of this work are: 1) to introduce the infrared planar laser-induced fluorescence (IR PLIF) technique, 2) to present a model-based framework for designing and analyzing IR PLIF imaging techniques, 3) to develop and demonstrate effective and straightforward implementations of IR PLIF diagnostics, particularly for the visualization of CO and CO₂, and 4) to map out the most fruitful paths for future work in developing, modifying, and extending these techniques.

This dissertation is organized as follows: after this brief introduction (Chapter 1), the three major subsections of this work are described in turn: IR PLIF of CO (Chapter 2), IR PLIF of CO₂ (Chapter 3), and IR PLIF using indirect excitation schemes (Chapter 4). A final chapter (Chapter 5) draws conclusions and considers the implications of this dissertation for future work.

Background information that is of general importance to this dissertation is presented in appendices. Appendix A describes the equipment used in the experimental work. Appendix B discusses rotational energy transfer theory and its implementation to analyze IR PLIF excitation processes. Appendix C discusses vibrational energy transfer theory and its implementation for calculations of IR PLIF fluorescence yield.

Chapter 2

IR PLIF of Carbon Monoxide

2.1 Introduction

IR PLIF of carbon monoxide was selected for the first demonstration of the IR PLIF technique. Although its absorption and emission features are weaker than many other species (such as CO₂), CO is an attractive demonstration species owing to its well-known spectroscopic parameters [29], well-investigated energy transfer processes [30], and single vibrational mode. This chapter will combine imaging measurements with an exploration of the detailed collision dynamics for CO imaging schemes and present a model-based framework for interpreting current and future IR PLIF imaging efforts. While PLIF imaging has been employed for visualization of a variety of flow parameters, including species concentration [2], temperature [3], velocity [31], pressure [4], and reaction rate [5], this chapter will be structured solely around imaging of molecular concentration. Extensions to other flow parameters have been discussed in various reviews [1, 6, 7].

Interpreting IR PLIF images in a meaningful way requires that excitation schemes be designed so as to maximize signal while minimizing error sources such as laser scatter, laser attenuation, radiative trapping, or spatially non-uniform fluorescence quantum yield. Since the processes of laser pumping, energy transfer, and camera integration change when PLIF techniques are modified to employ vibrational transitions, the analysis of these processes must be reconsidered for linear IR PLIF measurements.

This chapter presents the framework for analysis of linear IR PLIF excitation schemes

as well as specific results for CO. In the following sections, typical experimental configurations as well as techniques for image post-processing and interpretation will be described; the excitation schemes being considered will then be discussed and the pulsed excitation process, the parametric dependences of the effective fluorescence quantum yield, and the sensitivity of IR PLIF imaging techniques will be evaluated. Results will then be presented for several flow configurations.

2.2 Experimental Setup and Techniques

A typical experimental setup is shown in Figure 2.1. Laser light that is resonant with

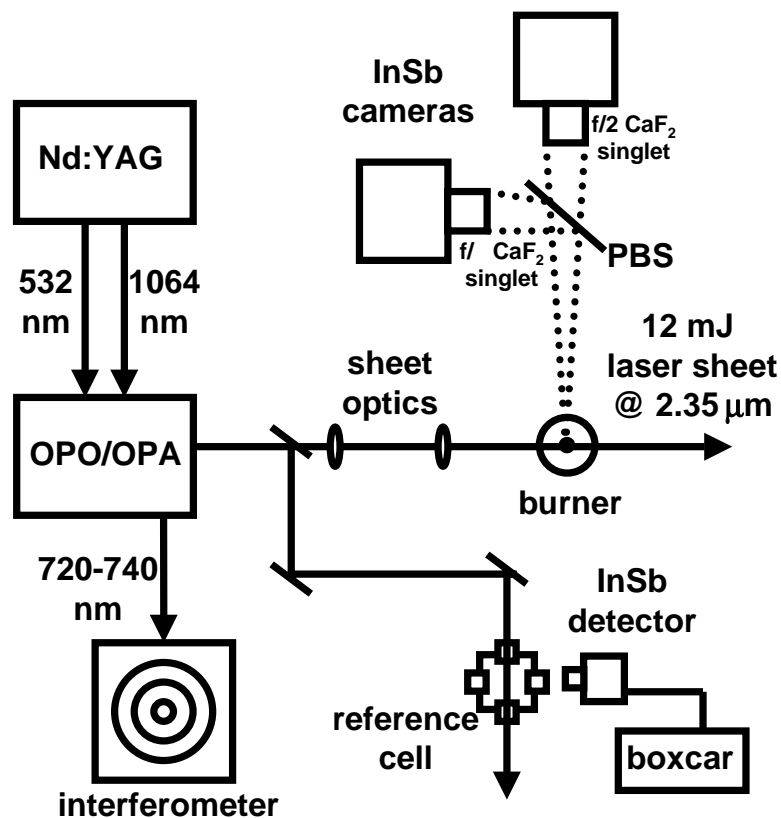


Figure 2.1: Typical IR PLIF experimental setup. PBS: pellicle beamsplitter.

vibrational transitions of CO is generated by the 10 Hz, nanosecond-pulse tunable infrared laser source discussed in Section A.2. The OPO is grating-tuned to absorption lines of the

overtone band of CO near $2.35 \mu\text{m}$ and centered on a specific line by passing the beam through a reference cell and maximizing LIF as measured by an InSb infrared detector and boxcar-averager. The beam is shaped using CaF_2 optics to form either a waist for single-point LIF measurements or a thin sheet for PLIF imaging. IR LIF signal is collected onto one or two LN_2 -cooled 256×256 InSb cameras (see Section A.4).

Post-processing is employed on images to eliminate a variety of error sources [1, 9, 25]. Fluorescence from a uniform flow or laser scatter off a surface is used to correct for inhomogeneities in the incident laser sheet. When performing this sheet correction, the uniform field image is binned along the direction of laser propagation to create a laser sheet function, spatial frequencies in the laser sheet function that are greater than 10 cm^{-1} are removed, and the experimental image is divided row-wise by the laser sheet function. No evidence of higher spatial frequencies ($k_x > 10 \text{ cm}^{-1}$) is observed in our laser sheet, so this filtering technique minimizes the noise introduced by sheet correction without generating a measurable error. Laser sheet inhomogeneity caused by laser attenuation in the imaged region is corrected for using known absorption cross-sections.

Background generated by A/D offsets or non-laser-induced emission is corrected for by subtracting a background image (collected without laser excitation) from the measured image. This is achieved with a single camera for steady flows. For unsteady flows, a dual-camera setup and a pellicle beamsplitter [32] are used. Here, techniques analogous to those in previous multi-camera PLIF studies (*e.g.*, [9] and references therein) are employed. Both cameras collect fluorescence from the same side of the image plane and the fluorescence is split between the two cameras with a $2 \mu\text{m}$ pellicle to ensure that the spatial separation of the two surface reflections at the focal plane ($< 4 \mu\text{m}$) is much less than a pixel width ($30 \mu\text{m}$). Identical collection optics are used at equal magnification, and the positions of the two image planes are aligned to within approximately one pixel of each other. Test images of a heated wire mesh are taken with both cameras and a spatial correlation between test images is used to transform one image onto another, correcting for any warping of the image plane caused by imperfections in the alignment, lenses, beamsplitters, and focal planes. Tests on this algorithm indicate that the images can be correlated to each other to within approximately 1/3 pixel; thus the spatial dynamic range of multiple-camera images is only very slightly degraded by the use of the multi-camera technique and the attendant

transformations. Since our PLIF images are primarily read-noise limited, SNR losses associated with dual-image techniques are modest. Spatial resolution perpendicular to the laser sheet is estimated to be $700 \mu\text{m}$ and is limited by laser sheet focusing optics, while in-plane resolution is limited by optical aberrations and pixel crosstalk and is estimated to be typically $1100 \mu\text{m}$ (~ 3 pixels). Resolution on this order is common from 100% fill factor focal planes, as they do not completely isolate pixels from their neighbors.

2.3 Fluorescence Equation

Fluorescence images are interpreted using the fluorescence equation, which is derived in this section for a linear excitation scheme. When using an integrating detector (*e.g.*, an infrared camera) and collection optics with efficiency η_c , LIF signal S_f is equal to the integral of the rate of laser-induced fluorescence \mathcal{F} over the exposure time τ , multiplied by the collection efficiency:

$$S_f = \int_0^\tau \mathcal{F}(t) dt \eta_c . \quad (2.1)$$

The rate of laser-induced fluorescence from each excited state j is given by the product of the laser-induced change in state population $\Delta N_j(t)$ in the measurement volume and the Einstein A emission rate from that state A_j . Summing over all states:

$$S_f = \sum_j \int_0^\tau \Delta N_j(t) A_j dt \eta_c . \quad (2.2)$$

In the linear (weak) excitation limit, the absorption process does not significantly perturb the system, and Equation 2.2 can be rearranged to separate the processes of absorption and emission. The number of absorbed photons $N_{p,\text{abs}}$ is given by the number of incident photons $N_{p,\text{inc}}$ times the absorbed fraction:

$$N_{p,\text{abs}} = N_{p,\text{inc}} n_{\text{abs}} \sigma \ell , \quad (2.3)$$

where n_{abs} is the number density (concentration) of the interrogated species, σ is its absorption cross-section, and ℓ is the length of the imaged region. The fluorescence quantum

yield ϕ_{lin} is then defined as the number of emitted photons normalized by $N_{\text{p,abs}}$:

$$\phi_{\text{lin}} = \sum_j \int_0^\tau \frac{\Delta N_j(t)}{N_{\text{p,abs}}} A_j dt . \quad (2.4)$$

With these definitions, the fluorescence equation can be written as:

$$S_{\text{f,lin}} = N_{\text{p,inc}} n_{\text{abs}} \sigma \ell \phi_{\text{lin}} \eta_c . \quad (2.5)$$

This format provides insight into the effect of parameters on fluorescence signal. $N_{\text{p,inc}}$ is dictated by laser pulse energy, η_c by the collection optics and camera, $n_{\text{abs}} \sigma \ell$ by the absorption properties of the interrogated species, and ϕ_{lin} by the magnitudes of excited state emission rates and the collisional interaction between the interrogated species and its environment. In particular, ϕ_{lin} embodies the effects of vibrational energy transfer processes with the bath gas. Fluorescence images can be converted to molecular concentration via Equation 2.5 by experimentally removing nonuniformities in $N_{\text{p,inc}}$ (via sheet correction) and η_c (via pixel calibration), and employing excitation schemes that generate a nearly uniform value for $\sigma \phi_{\text{lin}}$.

2.4 Excitation Schemes

The excitation scheme used for CO is designed to isolate the CO species concentration from other parameters and error sources (most notably spatial or thermal variations in σ and ϕ_{lin}) such that signal interpretation is straightforward. 8–15 mJ of energy is used to excite a rotational line of the first overtone ($2 \leftarrow 0$) band near $2.35 \mu\text{m}$, and fundamental emission ($2 \rightarrow 1$, $1 \rightarrow 0$) is collected at $4.7 \mu\text{m}$. The overtone absorption band is used so that laser scatter may be rejected with filters. In addition, absorption interferences are negligible in the $2.35 \mu\text{m}$ region except for a number of CO lines that overlap with $\text{CH}_4 \nu_3 + \nu_4$ band absorption lines— these lines should be avoided when imaging methane flames. Fluorescence at $4.7 \mu\text{m}$ is collected since it is the strongest fluorescence source. Bandpass interference filters are used to minimize emissions from soot and water and eliminate laser scatter and CO_2 emission. A cold gas filter [33–35] is used in flame experiments to reduce

emission associated with $(1 \rightarrow 0)$ transitions, which is the primary component of the background emission from hot CO. Since most of the LIF from nascent CO at flame conditions occurs between excited states $(2 \rightarrow 1)$, this filter effectively passes LIF and rejects flame luminosity. An example of CO gas filter performance is shown in Figure 2.2.

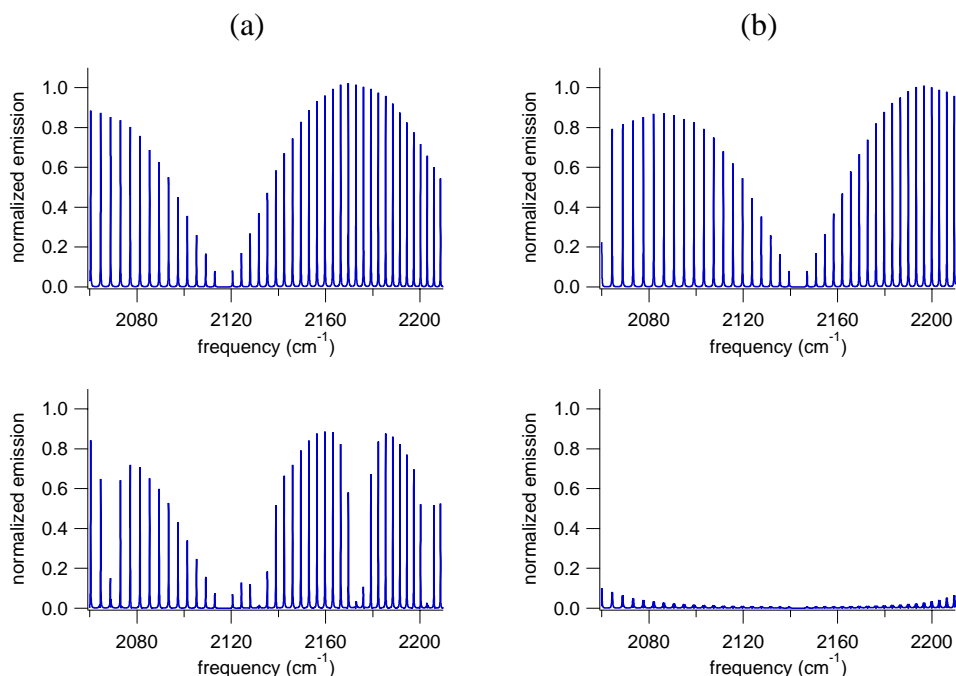


Figure 2.2: Filtering properties of a 1 cm pathlength of 300 K CO used to reject ambient gaseous emission. (a) $2 \rightarrow 1$ laser-induced fluorescence is shown before (top) and after (bottom) filtering. (b) $1 \rightarrow 0$ ambient fluorescence is shown before (top) and after (bottom) filtering. The cold gas filter strongly attenuates the ambient gas emission while leaving the $(2 \rightarrow 1)$ LIF mostly unaffected.

Since laser excitation occurs on nanosecond time scales and fluorescence integration occurs on microsecond timescales, the pulsed excitation process can be considered temporally separate from the vibrational relaxation process. Calculations of absorption and fluorescence are therefore presented in two different sections.

2.4.1 Absorption

Equilibrium Absorption Cross-Section

The absorption cross-section $\sigma(\nu)$ used in Equation 2.3 describes the probability that a photon at frequency ν will be absorbed by the interrogated molecule by providing the equivalent area if absorption were caused by a billiard-ball collision between a size zero particle (photon) and a finite cross-sectional area particle (the molecule). This cross-section can be written as a product of the Einstein B coefficient [cm], the Boltzmann fraction in the lower state $f_{v',j'}$, and the convolution of laser and absorption lineshapes g [cm]:

$$\sigma(\nu, P, T) = B f_{v',j'}(T) g(\nu, P, T). \quad (2.6)$$

Hence temperature dependence in σ is due to changes in Boltzmann fraction and lineshape convolution, while pressure dependence in σ is from the lineshape convolution only.

Boltzmann fraction. For heteronuclear diatomics, the Boltzmann fraction of a rotational state j in vibrational level v (assuming m_j states undistinguished) is given by

$$f_{v,j} = \frac{(2j + 1) \exp(-E_{v,j})/k_B T}{Q_{\text{rot}}(j, T) Q_{\text{vib}}(v, T)}. \quad (2.7)$$

In the rigid rotor and harmonic oscillator approximations, this becomes

$$f_{v,j} = \frac{(2j + 1) \exp(-j(j + 1)\Theta_r + v\Theta_v)/T}{T/\Theta_r (\exp(T/\Theta_v) - 1)}, \quad (2.8)$$

where Θ_r and Θ_v are characteristic temperatures [36] of rotation and vibration respectively.

Lineshape function. The molecular lineshape function φ describes the manner in which the molecular resonance is broadened by external factors. For narrow-linewidth laser excitation (which corresponds to all laser excitation in this report), the lineshape function's value at line center ($\varphi(0)$) is equal to g and is therefore the parameter of interest. For relatively nonpolar molecules such as CO and CO₂ and lines that are isolated at the pressure in question, φ is well-described by convolving the effects of Doppler (Gaussian) and lifetime (Lorentzian) broadening into a Voigt function. The Voigt function ignores velocity-class-dependent lifetimes, line mixing, and Dicke narrowing, all of which are minor for

these species and 1 atm conditions.

Simple relations [37] describe Doppler and lifetime (collisional) broadening mechanisms. Doppler broadening scales with molecular velocities and the Doppler lineshape FWHM is therefore proportional to $T^{1/2}$. Lifetime broadening for CO and CO₂ is dominated by rotational energy transfer (RET). For isobaric flows, collisional broadening FWHM scales in the gaskinetic limit as $T^{-1/2}$; more detailed analysis typically gives power-law exponents closer to -0.7 (CO) or -0.6 (CO₂).

In contrast to UV transitions, IR transitions are dominated by collisional broadening at 1 atm up to 1500 K. Even at higher temperatures, the effect at line center of Doppler broadening tends to be minor. Because of this, a power-law fit of line center values as a function of temperature can provide a simple (albeit phenomenological) functional form for g as a function of temperature:

$$g(T)/g(300\text{K}) = (T/300\text{K})^n . \quad (2.9)$$

Typical values for n are 0.6 (CO) or 0.5 (CO₂).

Dynamics of Absorption Cross-Section

Equation 2.3 tacitly assumes that the laser-induced perturbation of state distributions is small, so the absorption cross-section per CO molecule σ does not change during the laser pulse. To use Equation 2.5 to interpret IR PLIF images, then, this assumption must be confirmed, establishing that S_f is linear with $N_{p,inc}$. For the CO excitation scheme, experimental measurements and calculations of rotational energy transfer (RET) processes during the laser pulse have been used to confirm that fluorescence is in the linear regime and that standard PLIF experimental techniques and post-processing procedures may be used. These procedures, which include the sheet correction techniques described earlier in this chapter, can introduce errors if fluences are high enough to perturb state distributions and generate nonlinear absorption. By establishing that fluorescence is in the linear regime, these results confirm the accuracy of current experiments and can be used to project the success of future efforts which might employ more powerful laser systems, different sheet optics, or irradiated regions of different sizes.

Four-level model

In this section, we model the pulsed excitation process using a rate equation analysis that includes the effects of both laser pumping and collisional rotational energy transfer processes. Because VET for CO is much slower than RET, VET is ignored during the laser pulse. As a simplification, the pulsed excitation process is described using a four-level model (Figure 2.3). This is a standard model [38] in which the upper and lower

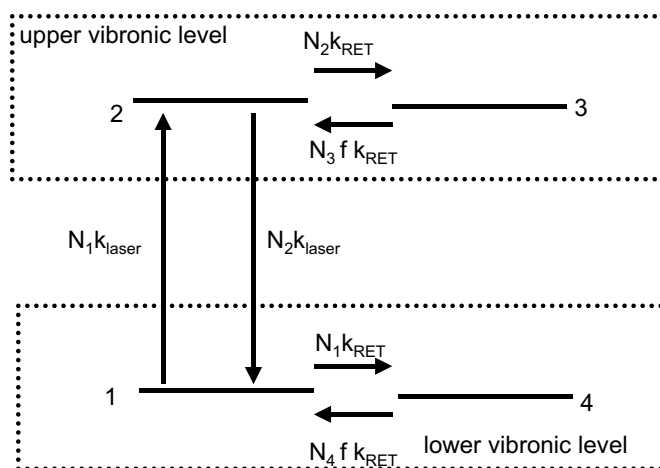


Figure 2.3: Four-level model for analysis of pulsed excitation with rotational energy transfer. The rotational bath (levels 3 and 4) is assumed to be equilibrated with the translational temperature. Energy transfer processes are shown with arrows.

levels of the transition are connected via the laser field. RET connects each of the laser-coupled levels to the rotational bath of their respective vibronic levels. States 1 and 2 are the lower and upper states, respectively, of the optical transition. All other rotational states in the vibronic levels are grouped into bath states 3 and 4, which correspond to the upper and lower levels, respectively. Laser pumping distributes molecules between levels 1 and 2, while RET drives the rotational populations toward a Boltzmann distribution in which states 1 and 2 each hold the Boltzmann fraction f of the total population of their vibronic level. For simplicity, the rotational degeneracy ratio $((2j + 1)/(2j + 3))$ for an $R(j)$ transition) is

neglected in this model. The rate equations for this system then become:

$$\begin{aligned}
 \frac{dN_1}{dt} &= -N_1 k_{\text{laser}} + N_2 k_{\text{laser}} - N_1 k_{\text{RET}} + N_4 f k_{\text{RET}} \\
 \frac{dN_2}{dt} &= N_1 k_{\text{laser}} - N_2 k_{\text{laser}} - N_2 k_{\text{RET}} + N_3 f k_{\text{RET}} \\
 \frac{dN_3}{dt} &= N_2 k_{\text{RET}} - N_3 f k_{\text{RET}} \\
 \frac{dN_4}{dt} &= N_1 k_{\text{RET}} - N_4 f k_{\text{RET}}
 \end{aligned} \tag{2.10}$$

$N_1 + N_2 + N_3 + N_4$ is constant since this is a closed system. During the laser pulse, the laser excitation depletes level 1 and overpopulates level 2. Thus the two-level system (levels 1 and 2) are driven towards equal populations, corresponding to infinite temperature. k_{RET} equilibrates levels 1 and 2 with bath states 3 and 4 (which are at the translational temperature T_{tr}). If k_{RET} is fast, the system will remain in equilibrium and the temperature of the level 1-level 2 system will remain equal to that of the level 3-level 4 system. In contrast, if k_{RET} is slow compared to k_{laser} then the level 1-level 2 system will have a higher temperature than the level 3-level 4 system. In addition, the relative magnitude of the laser pulse will dictate the extent to which the overall system temperature departs from the pre-laser temperature.

Transfer rates. If it is assumed that line broadening stems entirely from rotational energy transfer and that the RET rates are independent of vibrational level, the rate of transfer out of a specific rotational state (k_{RET}) may be inferred from line broadening:

$$k_{\text{RET}} = 2\pi c \Delta\nu_{c_i}, \tag{2.11}$$

where c is the speed of light [cm/s] and $\Delta\nu_{c_i}$ [cm^{-1}] is the HWHM collisional broadening of the pumped line with the given pressure and bath gas. The rate of laser pumping is given by:

$$k_{\text{laser}} = \sigma I / h\nu, \tag{2.12}$$

where I is the irradiance [W/cm^2] and $h\nu$ is the photon energy [J]. Level populations as a function of time are displayed for a sample case in Figure 2.4. At this large fluence ($600 \text{ mJ}/\text{cm}^2$), the nonequilibrium is clear in the ratio of populations in levels 2 and 3. With no laser energy (at the beginning and end of the pulse), the ratio of levels 2 and 3 is

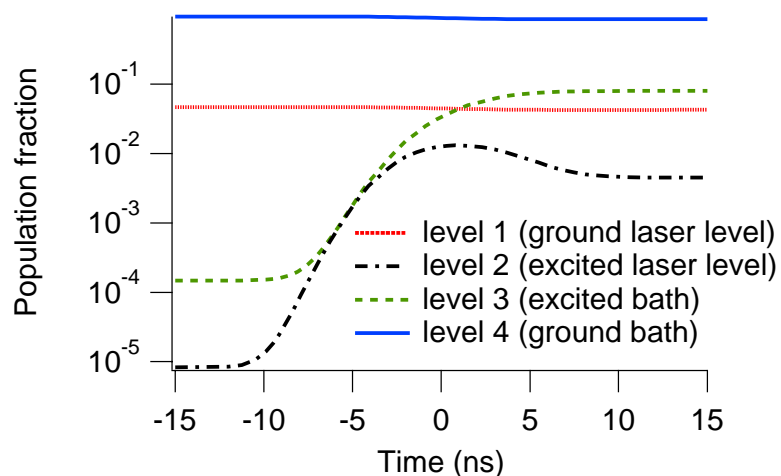


Figure 2.4: Population fractions as a function of time for the four-level RET model. $T=300$ K, $R(13)$ excitation in the 2ν band, 600 mJ/cm^2 fluence, 6 ns FWHM laser pulse.

dictated by equilibrium and is indicated (on this logarithmic plot) by the distance between their lines on the plot. In contrast, at high irradiance (during the peak of the laser pulse), the laser dominates over RET and level 2 is overpopulated. Here the ratio between the level populations departs from its equilibrium value.

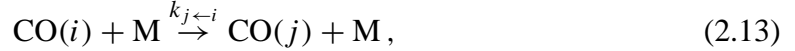
Qualitatively, the result of this simple model is that the system is linear (laser-induced perturbations are small) if the number of absorbed photons is small as compared to the number of absorbers in the interrogated volume and if k_{RET} is also greater than k_{laser} .

Detailed model

The four-level model is useful for conceptual purposes and is suitable for approximately determining the effects of RET on departure from linear absorption; however, it assumes that all rotational state populations except for the laser-coupled states are in equilibrium, and at high fluences might be expected to overpredict the effectiveness of RET as compared to a detailed analysis. Thus, to evaluate the quantitative accuracy of this model, an integration of state-to-state rate equations is also used and the two approaches are compared.

For the detailed (state-to-state) approach, each rotational state j is considered (m_j states, though, are not distinguished). State-to-state RET rates (as well as their scaling

relations) for CO have been studied in the context of line broadening and mixing, and rates given by these scaling laws can be employed straightforwardly and confidently for a detailed analysis. For a particular laser pulse, the laser transition is accounted for using the known Einstein B coefficient and the time-dependent laser intensity. For $2.35 \mu\text{m}$ excitation of CO, state-to-state RET rates were modeled using a modified exponential-gap (MEG) scaling law akin to one used for studies of CO Raman line mixing [39, 40]. The MEG scaling was chosen since it is straightforward to implement and successfully reproduces line broadening and mixing in CO. In the form of MEG implemented here, endothermic RET rates were fit for collisionally induced rotational state changes:



through the use of the equation:

$$k_{j \leftarrow i} = A \left(\frac{296}{T} \right)^n \left(\frac{1 + E_i/k_B T \delta}{1 + E_i/k_B T} \right)^2 \exp(-\beta \Delta E/k_B T). \quad (2.14)$$

Here $k_{j \leftarrow i}$ is the transition rate from rotational state i to j ; E_i is the energy of state i [J]; T is temperature [K]; $\Delta E \equiv E_j - E_i$, k_B is Boltzmann's constant [J/K]; and A [s^{-1}], β , δ , and n are fitting parameters. Exothermic reaction rates follow from detailed balance. MEG parameters are fit for a particular bath gas so that the summed state transfer rates match measured or calculated HWHM line broadening values from [40–43]:

$$2\pi c \Delta \nu_{c_i} \equiv \sum_{\substack{j=1 \\ j \neq i}}^{\infty} k_{j \leftarrow i}. \quad (2.15)$$

Elastic dephasing and resonant R-R transfer can be ignored since both pathways have been shown to have negligible effect on CO line mixing and broadening [39, 44]. Rotational transfer rates in $v = 2$ are assumed identical to those in $v = 0$ since CO IR and Raman linewidths are constant with vibrational level [40, 44, 45] (see Appendix B).

Given state-to-state RET rates, a spatial and temporal integration of state populations during pulsed excitation may be used to predict the dependence of LIF signal magnitude

on fluence. The predictions of the four-level model as well as the detailed, state-resolved model (which uses the MEG scaling law) were confirmed experimentally by measuring single-point LIF intensity as a function of pulse energy and comparing to the model predictions. A 250 mm focal length CaF_2 spherical lens was used to focus the $2.35 \mu\text{m}$ beam down to an approximately Gaussian waist with FWHM of $330 \mu\text{m}$ and Rayleigh range of 43 mm. By focusing to a single point, fluences approximately 300 times higher than those typically used in imaging experiments can be achieved; large fluences cause non-Boltzmann distributions and more thoroughly test the RET model. The temporal profile of the near-IR (731 nm) OPO output was measured with a fast photodiode (Thorlabs DET-210), and the result after instrument function deconvolution (~ 6 ns FWHM Gaussian) was used as the temporal profile of the $2.35 \mu\text{m}$ pulse for the purposes of the calculations.

Calculations with the MEG scaling law (parameters for this mixture: $A=4.2 \times 10^8 \text{ s}^{-1}$, $\beta=1.35$, $\delta=1.17$, $n=0.69$) are compared in Figure 2.5 with results of the four-level model and the experimental data. The good agreement between experiment and the MEG scaling law model indicates that the MEG scaling law analysis is quantitatively accurate and can be used to predict absorption processes. The four-level model is satisfactory at the lower

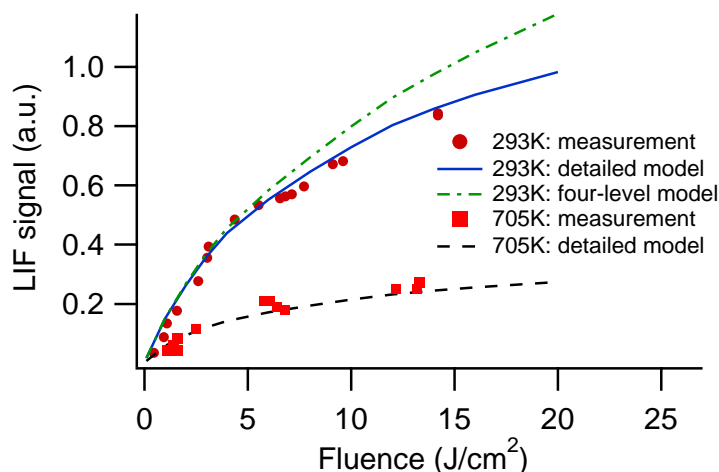


Figure 2.5: Comparison of computational results and experimental measurements of LIF as a function of characteristic fluence, defined as pulse energy divided by square of beam waist FWHM. Measured LIF signal is relative. 293 K ($R(8)$ excitation) and 705 K ($R(12)$ excitation) experimental values are all scaled by a single constant factor, which is chosen to best match the computation.

fluences shown in this figure (which are still much higher than those used in planar measurements), but deviates by as much as 20% at the highest fluences. The four-level model is therefore deemed appropriate for estimating the linear excitation regime, but state-to-state resolution is required to accurately model highly nonlinear IR LIF excitation at high fluences which might be used for point measurements.

Having matched the modeled RET rates to transition linewidths and confirmed that the rate equation analysis accurately predicts the growth of signal intensity with increasing fluence, we use the MEG scaling law calculations to confirm that our experimental parameters for IR PLIF imaging lead to linear fluorescence. Note that, for the purposes of this confirmation, the four-level model and the MEG scaling law calculations give identical results. We define the acceptable fluence as the maximum fluence for which the predicted errors in LIF signal caused by laser perturbation of state populations are below 10%, and we plot acceptable fluences as a function of temperature in Figure 2.6 for a typical set of experimental parameters. The acceptable fluence range decreases with temperature due to

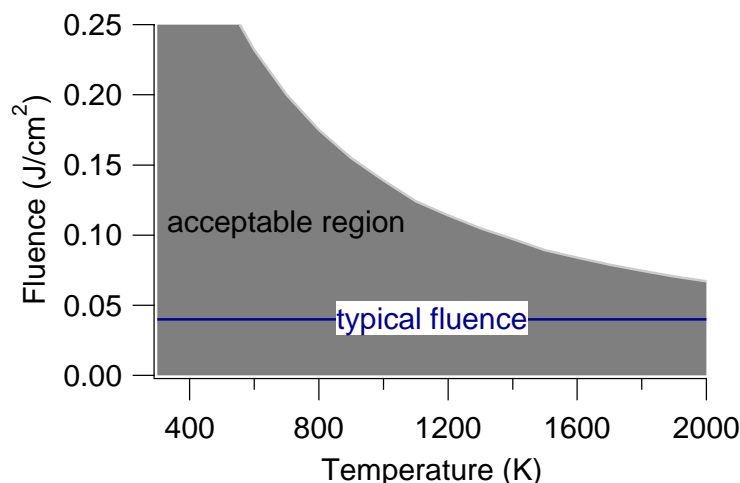


Figure 2.6: Acceptable fluence shown as a function of temperature. Assumed experimental parameters: 1 atm, trace CO in air, excitation of the strongest R line, factor of two spatial variation of irradiance across the image due to laser sheet profile nonuniformity and beam focussing, $500 \mu\text{m}$ sheet thickness. MEG RET model is used. Results using the four-level model are essentially identical for these fluences.

decreased collision rates and smaller RET cross-sections. For comparison, a typical value

for laser fluence during planar excitation is shown, indicating that current experiments are within the linear regime as defined above. The perturbation of the state distributions is not significant enough to affect interpretation of PLIF signal. This conclusion is essential to IR PLIF imaging of CO—despite the high pulse energies, a simple, linear analysis may be used to interpret PLIF signal, enabling the use of a focused (non-collimated) sheet and standard sheet-correction techniques.

2.4.2 Fluorescence

Having used RET calculations to confirm that typical fluences in IR PLIF experiments generate fluorescence within the linear regime, we use VET calculations to evaluate the effective fluorescence quantum yield ϕ_{lin} . As described earlier, the goal of excitation/collection scheme design is to make the value of $\sigma\phi_{\text{lin}}$ uniform throughout the image.

In contrast to electronic PLIF measurements, for which the excited state population can typically be modeled with good accuracy by an exponential decay with a single characteristic decay rate, the decay of the laser-induced vibrational nonequilibrium is not always exponential and can be dictated by several different types of energy transfer processes. Selected VET processes for the CO excitation scheme are shown schematically in Figure 2.7.

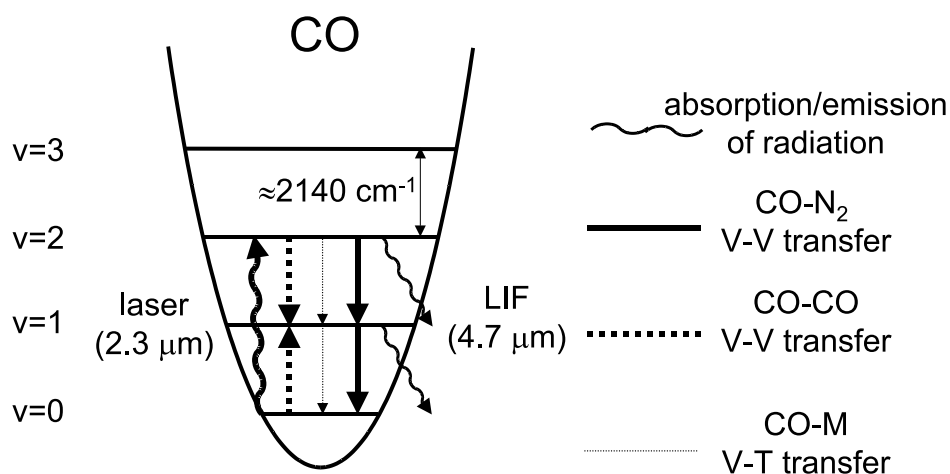


Figure 2.7: CO excitation/collection scheme with attendant VET processes.

Depending on the rates of these processes and the camera exposure time, the fluorescence

quantum yield ϕ_{lin} will not always take on a form for IR PLIF measurements which is similar to that used for electronic PLIF measurements. In order to describe the functional form expected for IR PLIF fluorescence quantum yield, the current section will discuss two systems: (1) a model four-level system which is greatly simplified and thereby helps to clarify the limiting behavior of IR PLIF schemes; and (2) a fully resolved vibrational system whose modeling requires numerical integration but that accurately represents the vibrational manifolds of PLIF species and their collisional partners in combustion systems.

For the purposes of generating a qualitative understanding of how ϕ_{lin} depends on VET rates, results are first presented for a model four-level system with energy levels and rates shown in Figure 2.8. This model system treats molecular species as two-level systems

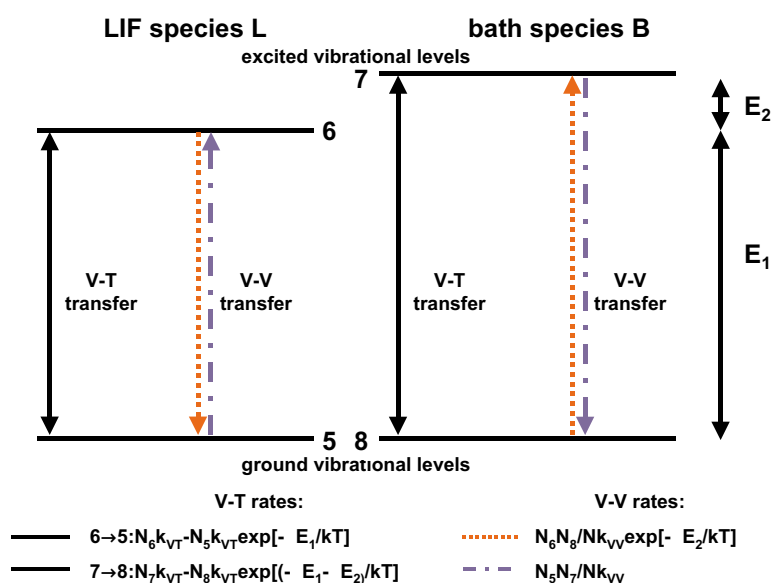
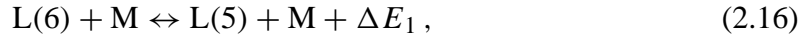


Figure 2.8: VET rates for model four-level system. Radiative transfer is a minor energy transfer mechanism and is omitted from this figure. These levels are thus numbered 5–8 to differentiate them from the levels in the four-level RET model levels.

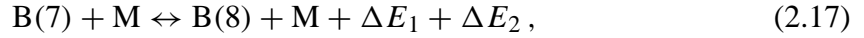
and considers two diatomic species: the LIF species L (the species that is excited by the laser and whose fluorescence is collected by the camera) and a near-resonant bath species B (a species that does not interact with the laser but has excited vibrational levels that are near-resonant with the excited levels of the LIF species). In treating species as two-level

diatomic systems, this model system eliminates intramodal V-V relaxation (which would be present if more than two levels were considered) and intermodal V-V relaxation (which would be present if polyatomics were considered). Note that, in contrast to the four-level model used to examine the pulsed excitation process (Figure 2.3), each level in Figure 2.8 is an ensemble of all rotational states in the vibrational level. For LIF measurements in a pure gas, levels 7 and 8 are not used, and the system is effectively two-level.

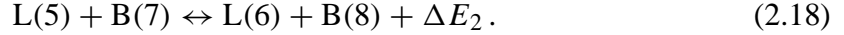
Following laser excitation that populates level 6, the system equilibrates with other species via vibration-to-vibration (V-V) processes at a characteristic rate denoted as k_{VV} and equilibrates with the translational temperature via vibration-to-translation (V-T) processes at a characteristic rate denoted as k_{VT} . V-T transfer proceeds via the following mechanisms:



with forward rate $N_6 k_{VT}$ and backward rate $N_5 k_{VT} \exp(-\Delta E_1/k_B T)$; and



with forward rate $N_7 k_{VT}$ and backward rate $N_8 k_{VT} \exp[-(\Delta E_1 + \Delta E_2)/k_B T]$. V-V transfer proceeds via:



with forward rate $N_5 N_7 / N k_{VV} \exp(-\Delta E_2/k_B T)$ and backward rate $N_6 N_8 / N k_{VV}$. In all cases, M implies any molecule. The rate equations for this system are:

$$\begin{aligned} dN_5/dt &= N_6 k_{VT} - N_5 k_{VT} \exp(-\Delta E_1/k_B T) \\ &\quad - \frac{N_5 N_7}{N} k_{VV} + \frac{N_6 N_8}{N} k_{VV} \exp(-\Delta E_2/k_B T) \\ dN_6/dt &= N_6 k_{VT} - N_5 k_{VT} \exp(-\Delta E_1/k_B T) \\ &\quad + \frac{N_5 N_7}{N} k_{VV} - \frac{N_6 N_8}{N} k_{VV} \exp(-\Delta E_2/k_B T) \\ dN_7/dt &= N_8 k_{VT} - N_7 k_{VT} \exp[-(\Delta E_1 + \Delta E_2)/k_B T] \\ &\quad - \frac{N_5 N_7}{N} k_{VV} + \frac{N_6 N_8}{N} k_{VV} \exp(-\Delta E_2/k_B T) \\ dN_8/dt &= N_8 k_{VT} - N_7 k_{VT} \exp[-(\Delta E_1 + \Delta E_2)/k_B T] \\ &\quad + \frac{N_5 N_7}{N} k_{VV} - \frac{N_6 N_8}{N} k_{VV} \exp(-\Delta E_2/k_B T) \end{aligned} \quad (2.19)$$

While the major simplifications associated with the model four-level system prevent it from matching the exact behavior of a complete vibrational relaxation system, the model system's simplicity facilitates straightforward discussion of ϕ_{lin} and its approximate dependence on experimental and physical parameters.

The fluorescence quantum yield (Equation 2.4) reduces to simpler expressions in certain limits when the model four-level system from Figure 2.8 is analyzed. Assuming, for simplicity, that the excited state is unpopulated before laser pumping, Equation 2.4 becomes

$$\phi_{\text{lin}} = \int_0^\tau A \frac{N_6(t)}{N_{\text{p,abs}}} dt . \quad (2.20)$$

Here $N_{\text{p,abs}} = N_6(t = 0)$ is the number of absorbed photons, or equivalently, the number of molecules excited by the laser. Equation 2.20 simplifies further in certain limits, several of which are discussed in the following paragraphs.

Fast equilibration of pumped mode with translational mode. When the collisional V-T decay is fast compared to the camera exposure time and V-V equilibration is not present, the fluorescence quantum yield simplifies to a ratio of emission and collisional transfer rates. For example, the collisional decay time $1/k_{\text{VT}}$ of CO_2 vibrational levels in 1 atm of H_2O is ~ 10 ns and minimum camera exposure times are 300 ns. For this case, $\tau \rightarrow \infty$, and Equation 2.20 simplifies to the familiar ratio of emission and collision rates:

$$\phi_{\text{lin}} = \int_0^\infty A \exp(-k_{\text{VT}}t) dt = A/k_{\text{VT}} . \quad (2.21)$$

Short exposure time. When the camera exposure time is much shorter than the characteristic time of vibrational equilibration, vibrational level populations do not change during the exposure time, and the fluorescence quantum yield is simply the product of the emission rate and the exposure time. For example, IR PLIF of room temperature CO might employ an integration time of $\sim 0.5\text{--}10 \mu\text{s}$, while the vibration-to-translation (V-T) energy transfer which depletes the vibrational energy occurs on millisecond time scales. In this case, $k_{\text{VT}} \leftarrow 0$, and Equation 2.20 simplifies to

$$\phi_{\text{lin}} = \int_0^\tau A \exp(-k_{\text{VT}}t) dt = \int_0^\tau A dt = A\tau . \quad (2.22)$$

Fast intermolecular vibrational equilibration; slow translational equilibration. When the system exchanges vibrational energy between molecules quickly, but loses vibrational energy to the translational and rotational modes slowly, the V-V transfer is quickly equilibrated, while the V-T transfer is frozen. In this case, $k_{VT} \rightarrow 0$ and $k_{VV} \rightarrow \infty$. Thus only k_{VV} terms in Equations 2.19 are retained, and the equilibrium between levels 6 and 7 is described by detailed balance. Setting temporal derivatives equal to zero, eliminating k_{VT} terms, and combining Equations 2.19, we find:

$$\frac{N_5 N_7}{N} = \frac{N_6 N_8}{N} \exp(-\Delta E_2 / kT). \quad (2.23)$$

The vibrational energy, which was initially held by the LIF molecules in level 6, is now shared between LIF and bath species in proportion to their mole fractions:

$$\frac{N_6}{\chi_L} = \frac{N_7}{\chi_B} \exp(\Delta E_2 / k_B T), \quad (2.24)$$

Here it is assumed that the vibrational excitation is small, therefore $N_5/N \approx \chi_L$ and $N_8/N \approx \chi_B$, where χ_L is the mole fraction of the LIF species L and χ_B is the mole fraction of the bath gas species B. Noting that, for $k_{VT} \rightarrow 0$, $N_6 + N_7 = N_{p,abs}$, and substituting Equation 2.24 into Equation 2.20, it can be shown that the vibrational energy in the fluorescing molecule is diluted by the bath gas, attenuating the PLIF signal:

$$\phi_{lin} = A\tau \frac{\chi_L}{\chi_L + \chi_B \exp(-\Delta E_2 / k_B T)}. \quad (2.25)$$

For large ΔE_2 , Equation 2.25 becomes Equation 2.22, while for small ΔE_2 , this simplifies to:

$$\phi_{lin} = A\tau \frac{\chi_L}{\chi_L + \chi_B}. \quad (2.26)$$

While the above results apply rigorously only to the model four-level system and thus give only semi-quantitative results for real systems, they serve to identify which parameters will be important for PLIF signal and which excitation schemes will be most successful. IR PLIF signal is most easily interpreted if the limit in Equation 2.22 is reached, since signals are independent of collisional environment. In cases with rapid resonant V-V transfer (CO

in N_2 , CO_2 in N_2), fluorescence quantum yield may scale approximately with mole fraction as described by Equation 2.26, making quantitative interpretation more challenging but increasing image contrast since LIF signal depends on mole fraction more strongly than linearly. In all cases, the presence of a rapid V-T quencher (*e.g.*, H_2O for IR PLIF of CO_2) can lead to PLIF signals which are inversely proportional to VET rates (Equation 2.21).

The limits described in Equations 2.21–2.25 are useful conceptual guidelines but are only approximate; ϕ_{lin} can be quantitatively evaluated only by integrating Equation 2.4. Starting with an initial condition which assumes a laser-induced vibrational nonequilibrium, our detailed VET model (Appendix C) uses a rate equation formulation and the CHEMKIN interface [46] to solve for the vibrational level populations as a function of time. The model assumes translational and rotational equilibrium (*i.e.*, a common rotational and translational temperature) since these modes equilibrate very quickly as compared to the camera integration time. To use the CHEMKIN interface and solver for vibrational energy transfer, the thermodynamic database input is modified to treat vibrational levels as individual species, and curves are fit to experimental or computational transfer rate data from a variety of references (see Appendix C for details). Key energy transfer rates for CO in a typical mixture for a mixture corresponding to a fuel-rich flame are shown graphically in Figure 2.9 (note for comparison that the characteristic time for radiative transfer is approximately 14 ms). Note that V-V transfer is the most important mechanism, while V-T transfer is important only in collisions with H_2O . The CHEMKIN interface provides reverse reaction rates consistent with detailed balance. Roughly 80 vibrational levels and 14,000 energy transfer processes are used.

The detailed VET model has been used to compute ϕ_{lin} for CO following 2ν excitation. Figure 2.10 shows temperature-dependent fluorescence quantum yield as a function of camera exposure time, strength of excitation, CO mole fraction, and H_2O mole fraction. For short exposures, the system approaches the no-quench limit of Equation 2.22, while for longer exposures, the effects of energy transfer processes are evident (Figure 2.10a). Exposure times near $1 \mu\text{s}$ are a good compromise between minimization of ϕ_{lin} variations and maximization of signal levels, and exposures near $1 \mu\text{s}$ are typically used for flame experiments. Strength of excitation (defined here as the fraction of molecules in the lower vibrational level which are pumped to the upper level) does not affect ϕ_{lin} for

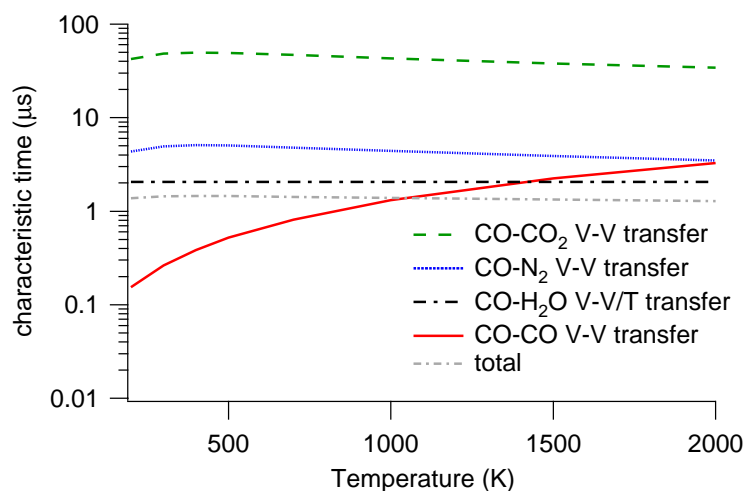


Figure 2.9: Characteristic times for vibrational energy transfer for CO as a function of temperature and collision partner. Characteristic times are shown for a 1 atm mixture of 5% CO, 10% CO₂, 10% H₂O in N₂. O₂ and inert gases are inefficient VET partners and are not considered.

CO, since translational heating during the exposure time is negligible (Figure 2.10b). The fluorescence quantum yield ϕ_{lin} shows minor dependence on CO mole fraction at high temperatures (Figure 2.10c). In this case, increased CO mole fraction minimizes the effects of vibrational energy dilution by resonant bath gases (CO₂, N₂) as expressed in Equation 2.25. These dilution effects become more prominent as temperature increases, since the increased translational energy decreases the effect of the energy gap associated with transfer from CO to N₂ and CO₂ (about 200 cm⁻¹ or 300 K energy defect). At the CO levels which are observed in most hydrocarbon flames (<5%), the maximum variation of ϕ_{lin} with CO mole fraction for a 1 μs exposure is ±7%. Note that this variation is much less than that predicted by Equation 2.25, which sets an upper bound for these effects. H₂O accelerates translational equilibration at all temperatures, and for a 1 μs exposure ϕ_{lin} varies by ±15% as water mole fraction is varied from 0–20% (Figure 2.10d). In both cases, variations are significantly smaller for 1 μs exposures than they are in the long-exposure limit (Equation 2.21). Note that in all cases the fluorescence quantum yield decreases with increasing temperature due to increases in VET rates.

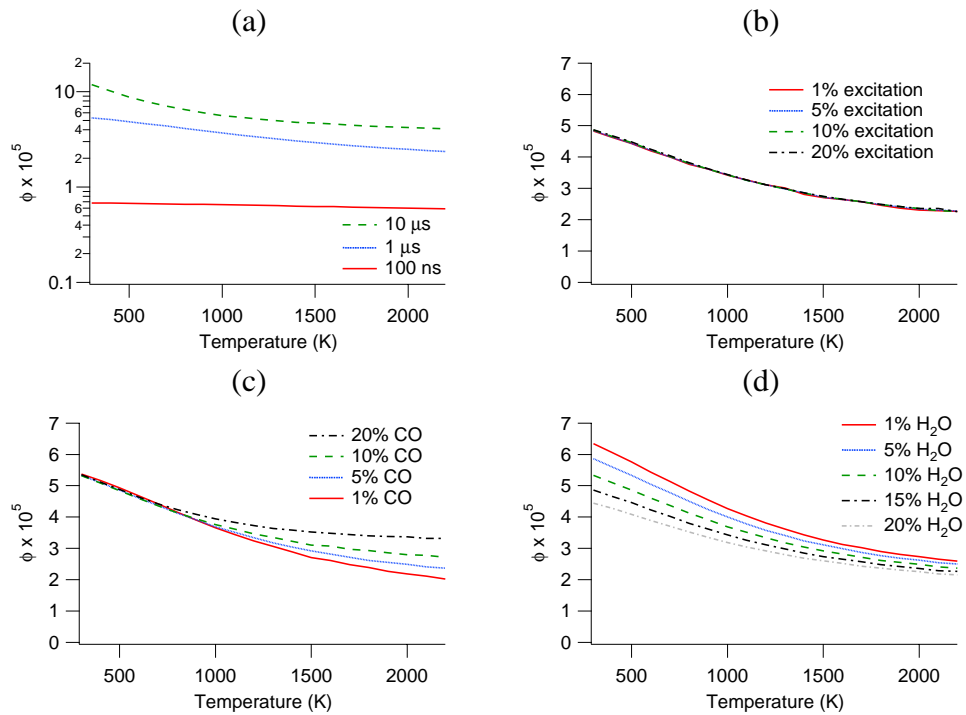


Figure 2.10: Effects of (a) exposure time, (b) strength of excitation, (c) CO mole fraction, (d) H₂O mole fraction on ϕ_{lin} for CO. Nominal parameters: 1 μs exposure, 10% excitation, mixture constituents 5% CO, 15% H₂O, 15% CO₂ in N₂. In each graph, one parameter is varied from the nominal value while other values are held constant. For comparison, note that in the no-quench limit, $A\tau = 7 \times 10^{-5}$ for a 1 μs exposure.

The above results show that the effects of varying bath gas composition are manageable, and that, with an appropriate exposure time, a single curve (Figure 2.10b) describes the dependence of ϕ_{lin} with temperature to a good approximation. With this in mind, excitation of specific rotational lines may be chosen to minimize the variation of signal levels in a particular temperature range. Thus, with an appropriate excitation line, PLIF signal levels are proportional only to species concentration and images may be interpreted in a straightforward fashion. Figure 2.11 shows the product of the fluorescence quantum yield ϕ_{lin} and the absorption cross-section σ as a function of temperature. By choosing a particular rota-

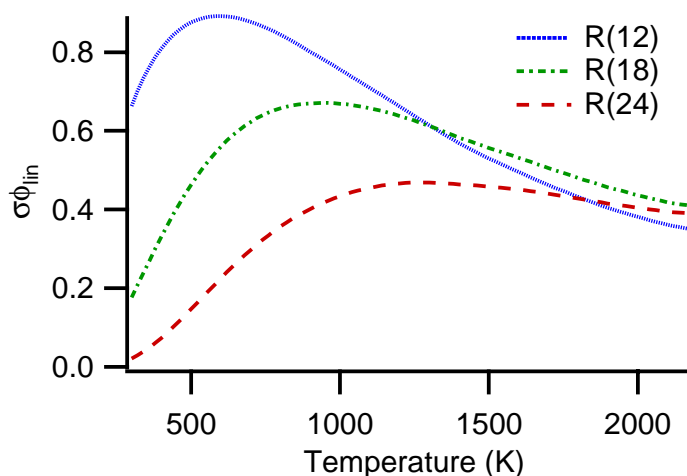


Figure 2.11: Product of absorption cross section and fluorescence quantum yield for CO (normalized to $R(7)$ line at 300 K) as a function of pumped line and temperature at 1 atm. The gas mixture is the same as was used for Figure 2.10. Spectrally narrow laser excitation at line center is assumed. From this graph, lines may be chosen which have roughly constant σ ($\pm 15\%$) in various regions ranging from room temperature to 2200 K.

tional line, $\phi_{\text{lin}}\sigma$, and therefore PLIF signal per CO molecule, can be made approximately independent of temperature within certain temperature ranges. Specifically, the $R(24)$ line generates signal which is constant to within $\pm 12\%$ over the 800–2200 K range and the $R(12)$ line generates signal which is constant to within $\pm 15\%$ over the 300–800 K range.

2.4.3 Sensitivity

We evaluate the sensitivity of IR PLIF techniques by comparing signal levels to noise that comes from A/D conversion (read noise) and background subtraction (shot noise). In contrast to electronic PLIF measurements, IR PLIF measurements are often read-noise-limited due to the high read noise associated with typical IR focal plane arrays. Recall that read noise for our camera systems is approximately 500 photoelectrons per pixel. Shot noise from background subtraction is a function of the experiment; typical values can be as high as 1000 photoelectrons at high temperatures if spectrally wide filters are used or if soot is present. Signal levels for IR PLIF measurements suffer from the low Einstein A coefficients associated with infrared transitions (for example, A for CO vibrational emissions from $v = 2$ to ground is 70 s^{-1} ; A for typical electronic transitions $\approx 1 \times 10^6$), but the slow collisional relaxation for vibrational transitions allows fluorescence to be integrated for a longer time. Figure 2.12 plots signal levels for two excitation lines as given in the figure caption as a function of temperature. Note that signal from both excitation lines is

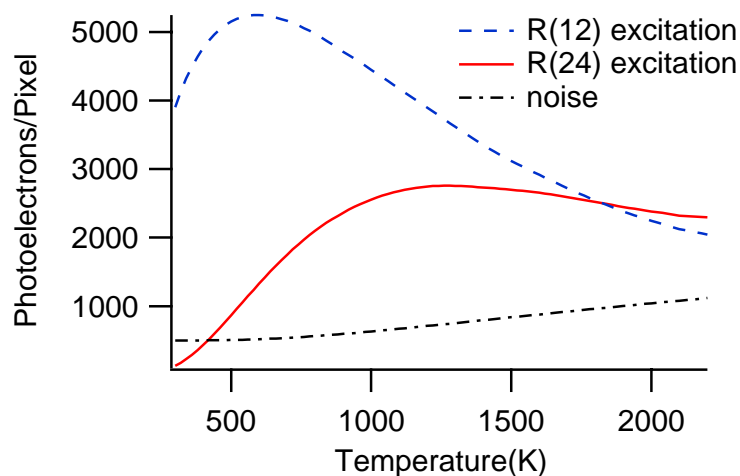


Figure 2.12: Calculated fluorescence signal as compared to noise levels for IR PLIF of CO. $n_{\text{CO}} = 1.7 \times 10^{17} \text{ cm}^{-3}$, corresponding to 5% CO at 2200 K, 1 atm. Bath gas 15% H_2O , 15% CO_2 , balance N_2 . $1 \mu\text{s}$ exposure, 10 mJ excitation pulse, $8 \text{ cm} \times 8 \text{ cm}$ image.

well above read noise. This plot shows that single-shot imaging of nascent levels of CO is possible using IR PLIF.

2.5 Imaging Results

Several flow conditions are used to demonstrate IR PLIF of CO, ranging from room-temperature mixing flows to laminar flames. Room-temperature mixing flows illustrate the ability of the technique to generate high-SNR images in a controlled environment, and imaging in higher-temperature environments demonstrate that imaging capabilities may be extended to flows of interest to the combustion community.

The first demonstration flow is a 6 mm diameter, room-temperature, forced jet, in which a valve is quickly opened and closed, superimposing an impulse onto a laminar jet flow, thus forming one or more vortex rings. A sample time series of single-shot images is shown in Figure 2.13. This flow is the most straightforward, as it is isothermal and the CO concentration is high, leading to easily-obtained, high-SNR images. Here the fluorescence quantum yield can be affected slightly by changes in CO and N₂ mole fraction, so signal in Figure 2.13 corresponds to PLIF signal and is a qualitative flow marker.

In order to demonstrate the technique for quantitative interpretation of IR PLIF signals, a turbulent CO/Ar jet in a CO/Ar/N₂ coflow was imaged from x/D of 0 to 10. The same excitation and collection scheme used to generate Figure 2.13 was employed with nominal pulse energy of 12 mJ. A sample result is shown in Figure 2.14.

Since the CO concentration in the coflow was known, the images are essentially self-calibrating. Post-processing steps are as follows: PLIF signal in the coflow is fixed to the known coflow mole fraction, thereby calibrating the collection optics and correcting for sheet intensity variations; laser attenuation is corrected for using known absorption cross-sections; and a comprehensive model of fluorescence quantum yield (Appendix C is used to adjust for the (relatively minor) fluorescence quantum yield variations. For these images, the 2 mm diameter central jet ($Re = 2800$) consisted of 50% CO/50% Ar, while the weak coflow consisted of 1.7% CO/1.7% Ar/96.6% N₂. Signal level in this image is quantitatively related to CO mole fraction as given by the color table. Values of CO mole fraction in the potential core are reasonably constant and match the expected value of 50%. In addition, averaged cuts as the jet approaches the far-field regime ($x/D = 8$ is shown in the figure) agree with the expected Gaussian profile and FWHM far-field spreading rates for a turbulent jet.

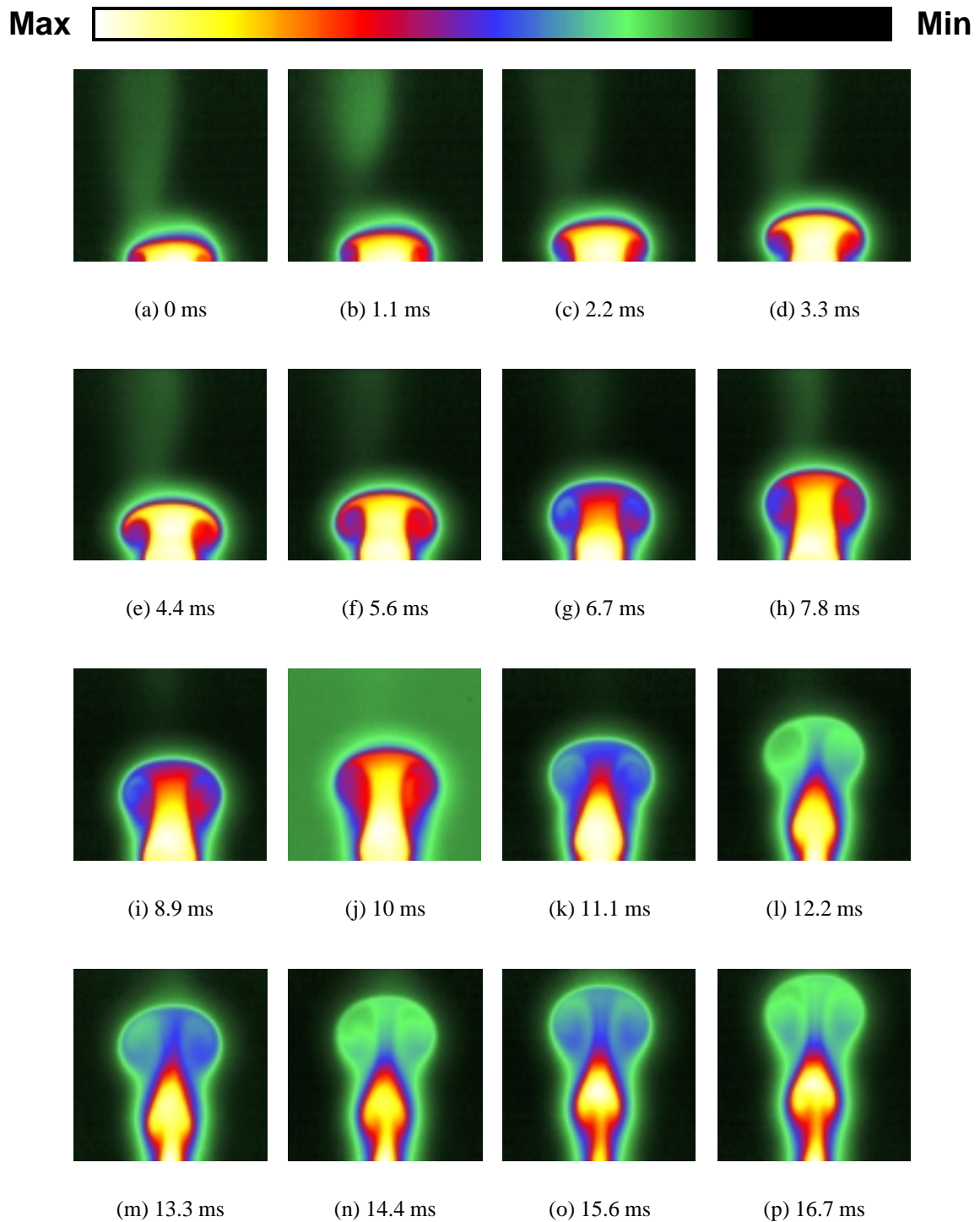


Figure 2.13: Single-shot IR PLIF images of a vortex ring developing from a 6 mm tube. Jet fluid is 50%CO/50%Ar. Ambient gas is air. 12 mJ at $2.35 \mu\text{m}$ is used to excite the CO. Integration time is $20 \mu\text{s}$. Images are collected at 10 Hz and the flow is phase-locked to allow a time series to be generated. PLIF signal in this isothermal, isobaric flow is proportional to CO mole fraction or concentration.

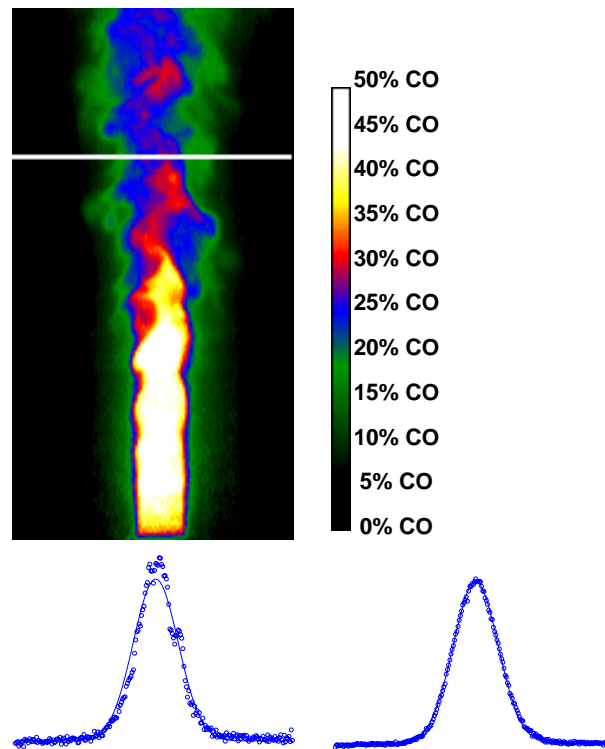


Figure 2.14: Turbulent CO/Ar jet in CO/Ar/N₂ coflow. Top: Corrected single-shot instantaneous image. White line indicates $x/D = 8$. Bottom: normalized cuts at $x/D = 8$ for instantaneous (left) and averaged (right) images are shown in comparison with the Gaussian curve which best fits the averaged data. Integration time is $5 \mu\text{s}$.

Representative peak SNR ratios for room-temperature images (Figures 2.13 and 2.14) range from 150–200. Signal levels of the images presented here can be used to infer a detection limit (SNR=1) for the present experimental setup of 1350 ppm at 300 K.

A 50%CO/50%Ar-fueled laminar diffusion flame (2% H₂ added for stability, air coflow) was used to demonstrate imaging of CO (fuel) in a flame condition. This flame (Figure 2.15) could be perturbed to explore unsteady effects as desired, although only steady results are presented here. Figure 2.16 shows typical CO imaging results. In these images,

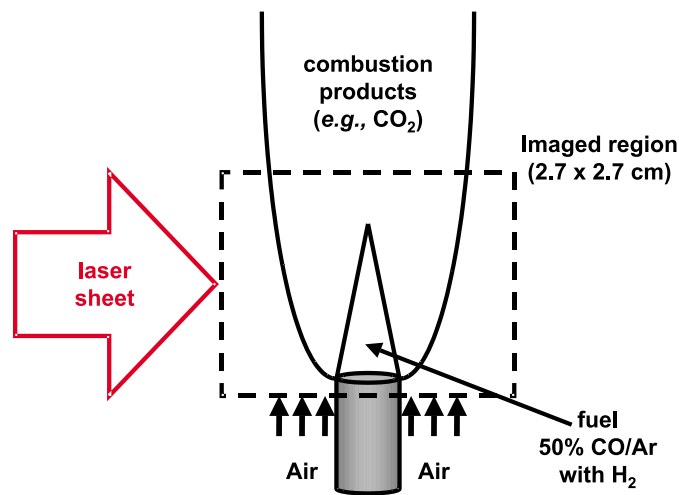


Figure 2.15: CO/Ar/H₂ flame and imaged region.

CO represents fuel and, since the $R(7)$ line is used, signal is weighted to low-temperature regions. The fuel region is clearly identified by the CO PLIF signal (which scales with CO concentration).

2.6 Conclusions: IR PLIF of CO

This chapter has introduced the IR PLIF technique, along with specific analysis and results for IR PLIF imaging of CO. Design procedures for excitation schemes as well as analysis required to interpret IR PLIF imaging of CO have been presented. Excitation at 2.35 μm followed by a 1 μs camera integration at 4.7 μm generates high signal levels while eliminating laser scattering, laser attenuation, radiative trapping, and fluorescence quantum

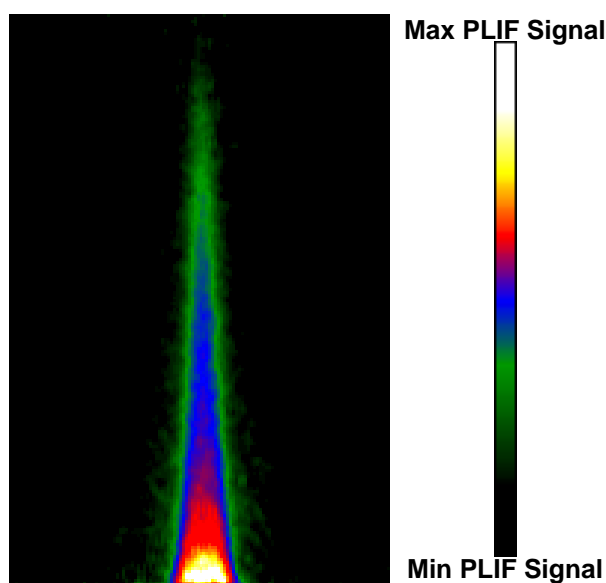


Figure 2.16: Single-shot CO PLIF image upon excitation of the $R(7)$ line of CO for a steady laminar coflowing CO/H₂ flame. Signal indicates the presence of CO (fuel).

yield variations. A model four-level system is presented to conceptually describe the dependence of IR PLIF signal. This model highlights differences in IR LIF dependence based on the relative length of time scales for camera exposure, V-T transfer, and V-V transfer. Integration of vibrational level populations as calculated with a rate equation analysis has been used to quantify fluorescence quantum yield and its dependence on bath gas temperature and species constituents. For CO, the vibrational energy transfer is slow enough that microsecond-scale integration times provided by our IR camera system effectively freeze the vibrational populations and make the fluorescence quantum yield approximately independent of the collisional environment. The $R(12)$ and $R(24)$ lines may be used to generate nearly temperature-independent signal within the 300–800 K and 800–2200 K regions, respectively. A detailed rate equation analysis of the transient absorption process in the presence of RET shows that typical experimental fluences reside within the linear regime and standard PLIF post-processing techniques may be used. While the detailed MEG scaling law analysis is required to properly predict LIF signal at very high fluences which may be employed for single-point measurements, a simple four-level (two-rate) model is sufficient to confirm linearity of LIF signal for planar imaging.

Calculations of signal and noise levels indicate that IR PLIF is sensitive enough to enable single-shot imaging of nascent CO in flames. Results are presented for room-temperature mixing flows and fuel visualization of laminar diffusion flames, showing the potential for IR PLIF for imaging of CO.

Chapter 3

IR PLIF of Carbon Dioxide

3.1 Introduction

While CO (Chapter 2) is an attractive demonstration species, IR PLIF of CO₂ has the highest potential impact as a combustion diagnostic owing to the current lack of an imaging diagnostic capable of measuring nascent CO₂ on a single-shot basis in combustion flows. For example, CO₂ imaging can be applied to aid model development through study of canonical flames or aid visualizing important CO₂ mixing processes such as those pertinent to residual-induced autoignition.

CO₂'s fluorescence performance differs from CO due to its three vibrational modes, near-perfect resonance of one mode with N₂ vibrations, and its affinity for vibrational energy exchange in the presence of H₂O. These differences are observed in the absorption and fluorescence properties of CO₂ and motivate changes from the excitation schemes used for CO.

The analytical framework for treatment of linear excitation schemes and experimental setup outlined in Chapter 2 is applied in this chapter to CO₂. In doing so, a number of challenges associated with applying linear schemes for CO₂ imaging are revealed. These challenges motivate the use of saturated schemes (which use a high-pulse-energy TEA CO₂ laser) to simplify IR PLIF image interpretation. The analytical framework for treatment of saturated excitation schemes for CO₂ is then presented to elucidate the effect of strong excitation on IR PLIF images.

3.2 Linear Excitation Schemes

This section will discuss linear excitation schemes in a manner similar to that of Chapter 2. This analysis will highlight a number of challenges associated with linear excitation schemes for CO₂, and will motivate a discussion of saturated excitation schemes for CO₂ which is then to follow.

3.2.1 Notation

When describing CO₂ energy levels, we use notation analogous to that of HITRAN [29]; a discussion of CO₂ level notation can be found in Appendix C as well as Ref. [47]. In addition to this standard notation, compact notation is also used here to denote groups of vibrational levels as units; for example, a level symbol that does not specify axial spin momentum (*e.g.*, 110) is used to indicate the group of levels corresponding to that energy (in this case, 11⁰0_I, 11⁰0_{II}, and 03³0).

3.2.2 Excitation Schemes

Several excitation options are available for CO₂, including combination bands at 2.0 μm (20⁰1_{II} ← 00⁰0) and 2.7 μm (10⁰1_{II} ← 00⁰0) and difference bands at 9.6 μm (00⁰1 ← 10⁰0_{II}) and 10.6 μm (00⁰1 ← 10⁰0_I). In all cases, fluorescence is collected via the fundamental ν₃ band at 4.3 μm. Absorption interferences at the laser wavelength are minor at 9.6 μm, 10.6 μm, and 2.0 μm for hydrocarbon flames. Excitation at 2.7 μm, though, poses experimental challenges, as laser attenuation due to ambient water and CO₂ is strong and must be eliminated by purging CO₂ and H₂O from the beam path between the laser and the imaged plane. Experiments to date using our OPO source have employed 2.0 μm excitation.

As was the case for CO (Chapter 2), analysis of RET and VET processes for CO₂ excitation will be used to evaluate the linearity of CO₂ excitation schemes and the parametric dependences of PLIF signal. This analysis is described in the following sections.

3.2.3 Absorption

Energy transfer processes during the laser pulse will be examined so as to confirm the validity of Equation 2.5 for application to IR PLIF images of CO_2 . In doing so, this analysis establishes the range of validity of Equation 2.5 and the assumption that the fluorescence signal S_f is linear with the number of incident photons $N_{p,inc}$.

A rate equation analysis including RET and VET has been used to define the range of acceptable fluences (fluences which generate $< 10\%$ error due to perturbed state distributions) for a number of excitation wavelengths. Energy transfer processes for the $2.0 \mu\text{m}$ excitation scheme are shown on an energy level diagram in Figure 3.1. Unlike CO, CO_2

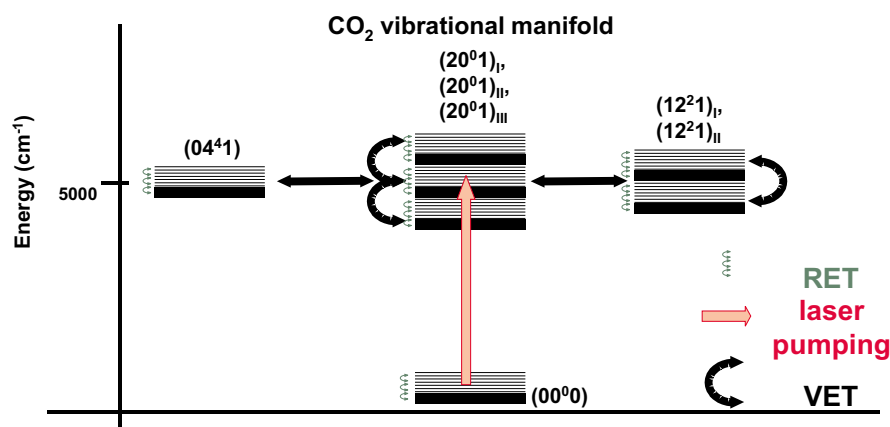


Figure 3.1: Energy transfer processes which occur during laser excitation for the sample case of $2.0 \mu\text{m}$ excitation of CO_2 .

has many vibrational levels in close proximity, and the vibrational transfer between these levels is fast. Vibrational energy transfer must therefore be considered for CO_2 since vibrational transfer rates between near-resonant states in CO_2 can be within a factor of ten of rotational transfer rates. For $2.0 \mu\text{m}$ excitation, the pertinent energy transfer processes are (a) collisional rotational energy transfer in the lower 00^0_0 and upper 20^0_1 vibrational levels of the laser transition and (b) vibrational energy transfer between the nine vibrational levels in the 20^0_1 manifold. Excitation pulses at $2.7 \mu\text{m}$, $9.6 \mu\text{m}$ and $10.6 \mu\text{m}$ can be analyzed in a similar fashion except for differences in lower and upper vibrational level degeneracies.

Vibrational levels not connected by the laser transition are assumed to be in rotational

equilibrium. For the levels perturbed directly by the laser pulse, state-to-state RET rates are used. CO₂ RET is described using a simple MEG scaling with rates inferred from line broadening or mixing. Details are discussed in Appendix B.

The strengths of each absorption band leads to a different acceptable fluence (< 10% error) limit, which is listed in Table 3.1 for a typical set of experimental parameters. For

Excitation Scheme	Acceptable Fluence
2.0 μm	1.160 J/cm ²
2.7 μm	0.015 J/cm ²
9.6 μm	0.025 J/cm ²
10.6 μm	0.031 J/cm ²
typical experimental fluence	0.040 J/cm ²

Table 3.1: Acceptable fluence (< 10% error) shown for several CO₂ excitation schemes at 1500 K. Assumed experimental parameters are the same as for Figure 2.6.

CO₂, 2.0 μm excitation leads to fluorescence that is linear with laser pulse energy (since, of the bands listed, its absorption is weakest), while excitation pulses at 2.7 μm , 9.6 μm , or 10.6 μm depart from linearity at modest fluences and are more appropriate for saturated excitation techniques [48].

3.2.4 Fluorescence

For CO₂, fluorescence is collected at 4.3 μm , corresponding to single-quantum changes in asymmetric stretch (ν_3) energy. The laser-induced excess of ν_3 energy is depleted by non-resonant intermodal V-V transfer (upon collisions with any molecule M) and by near-resonant transfer (upon collisions with CO and N₂). Because non-resonant transfer plays an important role in the vibrational relaxation of CO₂, H₂O's enhanced V-T transfer rates strongly affect CO₂ vibrational relaxation [49]. Also, because the characteristic time for CO₂-N₂ V-V transfer is on the order of 100 ns [50], N₂ dilutes CO₂ LIF signal as described by Equation 2.26. Figure 3.2 shows the impact of these effects on the fluorescence quantum yield. Most dramatically, at low CO₂ mole fraction, V-V transfer quickly removes energy

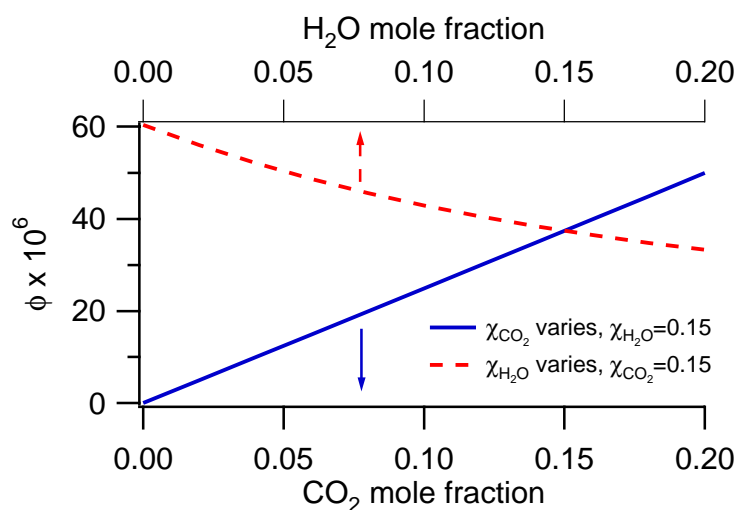


Figure 3.2: Predicted CO_2 fluorescence quantum yield ϕ for linear excitation and $1 \mu\text{s}$ exposure. Nominal gas mixture is 15% H_2O , 15% CO_2 , balance N_2 , 1000 K. Curves show effect as mole fraction of CO_2 or H_2O is changed.

from CO_2 and stores it in N_2 . In the limit as CO_2 mole fraction approaches zero, this process becomes dominant and the fluorescence quantum yield approaches A/k_{VV} , which for CO_2 - N_2 collisions is quite low. From this result, it is clear that a uniform CO_2 fluorescence quantum yield can not be readily achieved in combustion environments.

The variations in ϕ_{lin} caused by N_2 and H_2O mole fraction variations are compounded by the thermal dependence of the absorption cross-section of CO_2 (Figure 3.3). In this figure it is clear that the absorption cross-section decays rapidly as the temperature increases for all but the very-high-energy levels. As is typical for triatomics, CO_2 's vibrational partition function increases much more rapidly than that of a diatomic such as CO .

Taken together, collider-dependent fluorescence quantum yield and temperature-dependent absorption cross-section make nanosecond-pulse excitation of CO_2 in the linear regime only suitable for qualitative visualization. While these results limit the potential utility of linear IR PLIF imaging techniques for CO_2 , they motivate laser-saturated techniques [48], which have the potential to greatly simplify interpretation of CO_2 IR PLIF images. Laser-saturated techniques are discussed in Section 3.3.

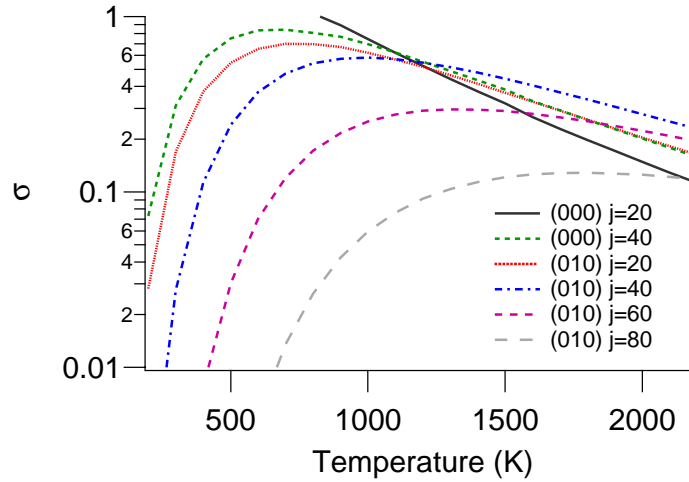


Figure 3.3: CO₂ absorption cross section (normalized to $R(30)$ line at 300 K) as a function of pumped line and temperature (for R transitions). Legend indicates the lower vibrational level (00^00 or 01^10) and rotational state. Spectrally narrow laser excitation is assumed.

3.2.5 Imaging Results—Linear Excitation

Excitation at $2.0 \mu\text{m}$ has been employed using the OPO system to visualize CO₂ in a room-temperature mixing process (Figure 3.4). In this figure, a forced 6-mm jet flow similar to that of Figure 2.13 was used to generate vortex rings of jet fluid (40%CO₂/60%Ar) which interact and cause the jet fluid to mix with the ambient air. Signal is indicative of the presence of CO₂. Typical maximum SNR in these images is 120, from which a minimum detectable mole fraction of 3300 ppm may be inferred. Excitation at $2.0 \mu\text{m}$ generates high signal levels in room-temperature flows without high water levels.

3.3 Saturated Excitation Schemes

This section will describe how saturated excitation simplifies interpretation of PLIF signals, provide a simple model for the saturated PLIF signal dependence, and support the validity of this model with a detailed rate equation analysis. Recall from Chapter 2 that, in the linear excitation regime, the fluorescence equation can be written as

$$S_{f,\text{lin}} = N_{p,\text{inc}} n_{\text{abs}} \sigma \ell \phi_{\text{lin}} \eta_c. \quad (3.1)$$

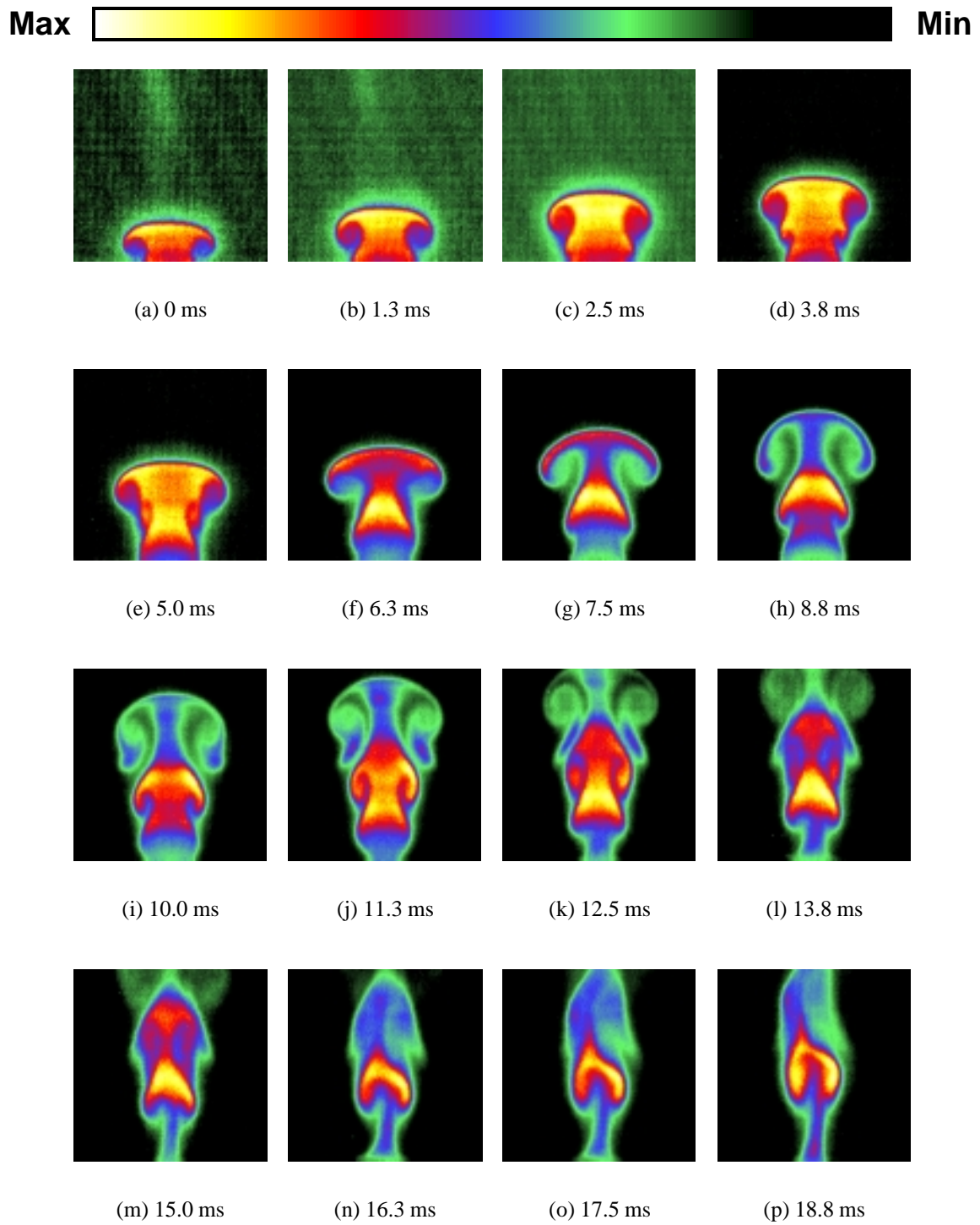


Figure 3.4: Single-shot IR PLIF images of vortex rings developing from a 6 mm tube. Jet fluid is 40%CO₂/60%Ar. Ambient gas is air. 8 mJ at 2.0 μm is used to excite the CO₂. Integration time is 20 μs . Images are collected at 10 Hz and the flow is phase-locked to allow a time series to be generated.

Successful linear PLIF techniques require that ϕ_{lin} be nearly independent of the bath gas species so that S_f can be directly related to a meaningful flow quantity (*e.g.*, n_{abs} or χ) via Equation 3.1. This is easily achieved for some species (*e.g.*, CO[32]; see Chapter 2). However, as was shown in Section 3.2, ϕ_{lin} for CO₂ varies significantly as a function of N₂ and H₂O mole fraction in the bath gas. Thus linear IR PLIF is difficult to quantify in combustion environments.

Saturated excitation is applied in this section to simplify signal interpretation for IR PLIF of CO₂. By saturating the laser transition with a high-pulse-energy laser, the upper and lower level populations are driven to be equal (neglecting small differences in state degeneracies) and are thus nearly constant throughout the pulse. This leads to different modeling techniques and simpler relations between CO₂ mole fraction and fluorescence signal.

For saturated fluorescence, it is more convenient to use a fluorescence yield ψ_{sat} which is defined as the number of emitted photons normalized by the number of absorbing molecules $n_{\text{abs}}V$ in the irradiated volume:

$$\psi_{\text{sat}} = \sum_j \int_0^\tau \frac{\Delta N_j(t)}{n_{\text{abs}}V} A_j dt . \quad (3.2)$$

Note that ψ_{sat} is an overall fluorescence yield, defined as fluorescence photons per molecule of the interrogated species, in contrast to ϕ_{lin} , which is a fluorescence *quantum* yield, defined as fluorescence photons per absorbed photon. With this definition for ψ_{sat} , the fluorescence equation takes a simple form:

$$S_{f,\text{sat}} = \psi_{\text{sat}} n_{\text{abs}}V \eta_c . \quad (3.3)$$

Since, for isobaric flows, we are most often interested in mole fractions rather than concentration, we can use the definition of mole fraction ($\chi_{\text{abs}} = n_{\text{abs}}/n$) and the ideal gas law ($P = nk_{\text{B}}T$) to rearrange this equation and show fluorescence signal as a function of the mole fraction:

$$S_{f,\text{sat}} = \frac{\psi_{\text{sat}}}{T} \chi_{\text{abs}} \frac{PV}{k_{\text{B}}} \eta_c . \quad (3.4)$$

Since V and η_c are easily calibrated experimentally, ψ_{sat}/T is the only parameter (in

02^20) is rapid, so the lower vibrational level is also repopulated through VET. Slower inter-modal VET processes repopulate the system after laser excitation but are slow as compared to the laser excitation process.

While a full description of state-to-state energy transfer including RET and VET can be used for precise calculations of ψ_{sat} , an investigation of the characteristic rates of energy transfer for this system shows that this system is approximately described by a simple three-temperature model. The structure of the CO_2 vibrational manifold and characteristic rates of vibrational energy transfer processes will be discussed in the following sections and will motivate a three-temperature model that describes the temperature dependence of IR PLIF signal.

3.3.1 CO_2 Vibrational Manifold: Saturated Excitation

The vibrations of CO_2 are coupled and anharmonic, exhibit Fermi-resonance (between ν_1 and $2\nu_2$), and are in some cases degenerate (ν_2). Thus the vibrational wavefunctions are not accurately described using harmonic oscillator wavefunctions, and vibrational level notation must distinguish between Fermi-resonant levels and levels with different angular momentum (see Appendix C and Ref. [47]). Despite their spectroscopic importance, though, these details may be ignored for calculations of energy transfer among the lower vibrational levels, since they do not significantly affect state populations or transfer rates. Detailed calculations later in the chapter will confirm that a harmonic oscillator analysis is accurate for calculation of fluorescence yield.

For the purposes of evaluating laser-perturbed state distributions and the fluorescence yield ψ_{sat} , we assume that the vibrational energy levels of CO_2 are described by four independent and harmonic vibrational modes (nondegenerate ν_1 and ν_3 , doubly degenerate ν_2). For each vibrational mode, we define a characteristic temperature Θ such that the product of the Boltzmann constant k_B and the characteristic temperature is equal to the vibrational energy spacing [36]. For CO_2 , $\Theta_1 = 2000$ K, $\Theta_2 = 960$ K, and $\Theta_3 = 3380$ K. Because each mode is treated as harmonic, the quantum number of each vibrational level is an approximate measure of how many quanta of vibrational energy the vibrational level

possesses in each vibrational mode. Furthermore, since each mode is treated as being independent, it can be considered to have its own energy distribution which is unaffected by the distribution of the energy of other modes. For example, the distribution of ν_3 quanta among the CO_2 molecules is treated as independent of the distribution of ν_1 or ν_2 quanta and, if Boltzmann, can be described with a vibrational temperature T_3 .

3.3.2 Characteristic Rates

The three-temperature model discussed in the upcoming section is motivated by the relative magnitudes of the characteristic rates of (1) laser pumping, (2) equilibration of the rotational state distribution with the translational temperature, (3) intramodal equilibration of individual modes, (4) equilibration of ν_1 with ν_2 , and (5) intermodal equilibration between the ν_3 mode and the other modes. These characteristic rates are plotted in Figure 3.6 as a function of temperature for CO_2 .

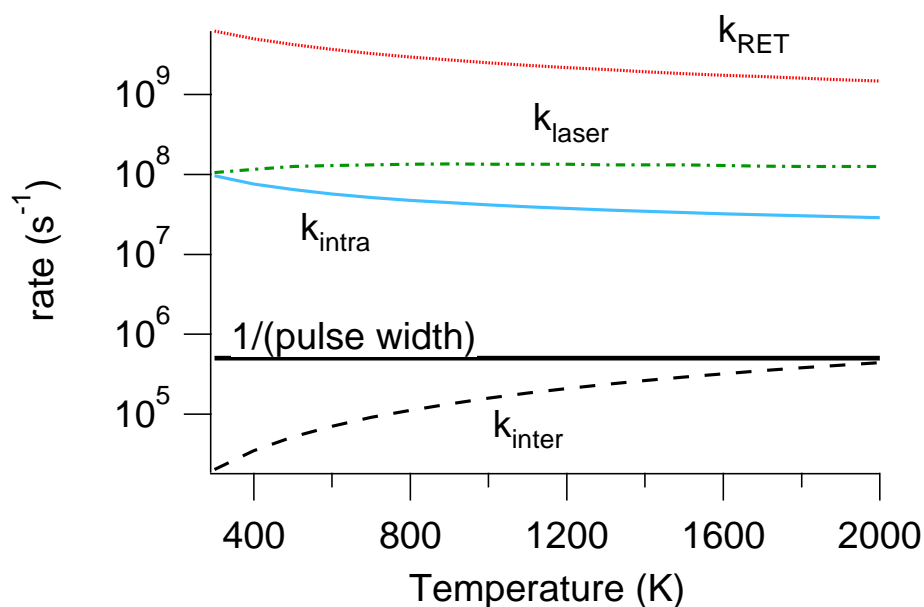


Figure 3.6: Important energy transfer rates as a function of temperature for CO_2 . k_{laser} is calculated assuming $dE/dt = 2.5 \times 10^6$ J/s, sheet dimensions $500 \mu\text{m} \times 4$ cm. For the line shape convolution integral, the laser was modeled as a 300 MHz Gaussian.

The characteristic rate of laser pumping, k_{laser} , is given by:

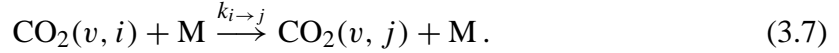
$$k_{\text{laser}} = \sigma I / h\nu, \quad (3.5)$$

where I is the irradiance [W/cm^2] and $h\nu$ is the photon energy [J]. k_{laser} is the characteristic rate at which CO_2 molecules in the $10^0 0_{\text{I}}$ level are pumped to the $00^0 1$ level.

The characteristic rate of RET, k_{RET} , is defined as the rate of equilibration of the lower state of the laser transition with the bath of rotational states in the lower vibrational level:

$$k_{\text{RET}} \equiv \sum_{\substack{j=1 \\ j \neq i}}^{\infty} k_{i \rightarrow j} = 2\pi c \nu_{c_i}, \quad (3.6)$$

Here the summed RET rate is proportional to the HWHM collisional broadening coefficient of the pumped line ν_{c_i} [cm^{-1}] times the speed of light c [cm/s]. $k_{i \rightarrow j}$ is the rate of transfer between rotational states i and j :



Elastic dephasing and R-R (rotation-rotation) interactions have been ignored in Equation 3.6 since elastic dephasing is a negligible contribution to broadening and R-R considerations are not required to satisfactorily describe RET in CO_2 [52–54].

Characteristic rates of inter- and intramodal energy transfer are defined using prototypical energy transfer reactions for CO_2 . Because ν_1 and ν_2 behave to a good approximation as a single mode, we group near-resonant energy transfer between ν_1 and ν_2 with intramodal processes for purposes of this discussion. The transfer between the $10^0 0_{\text{I}}$, $10^0 0_{\text{II}}$, and $02^2 0$ levels is the most important intramodal process for the $10.6 \mu\text{m}$ pumping scheme, and the rate of the $\text{CO}_2(02^2 0) + \text{M} \leftrightarrow \text{CO}_2 10^0 0_{\text{I}} + \text{M}$ reaction is taken as k_{intra} , characteristic of intramodal equilibration for display in Figure 3.6. Intermodal equilibration between the ν_3 mode and other modes occurs primarily through $\text{CO}_2 00^0 1 + \text{M} \leftrightarrow \text{CO}_2 11^0 0_{\text{I}} + \text{M}$ and similar reactions, all of which are much less efficient [50, 55]. This sum of intermodal energy transfer rates (k_{inter}) is plotted in Figure 3.6 as representative of intermodal equilibration.

3.3.3 Three-Temperature Model

Because of the relative magnitudes of the rates shown in Figure 3.6, the most convenient interpretation of the laser-induced state distributions is a three-temperature model which employs the harmonic oscillator approximation. This model will lead to a relation for the fluorescence yield ψ_{sat} as a function of temperature.

The magnitudes of the rates shown in Figure 3.6 imply that the five temperatures (T_{tr} , T_{rot} , T_1 , T_2 , T_3) are all well-defined and collapse to three independent temperatures which define the nonequilibrium (laser-perturbed) vibrational distribution. RET is very fast, so the rotational distribution in each vibrational level is Boltzmann with a well-defined rotational temperature equal to the translational temperature. Thus, even though the laser pumps only the $j = 20$ state directly, all rotational states in the 10^0_1 vibrational level are available for excitation since RET couples them to the lower states of the laser transition. Rapid intramodal relaxation implies that each vibrational mode has an individual Boltzmann distribution and therefore a well-defined temperature. Furthermore, energy transfer between the ν_1 mode and the ν_2 mode is fast (and $T_1=T_2$) due to the accidental degeneracy between ν_1 and $2\nu_2$. From these observations, we can conclude that T_{tr} , T_{rot} , T_1 , T_2 , and T_3 are all well defined; furthermore $T_{\text{tr}}=T_{\text{rot}}$ and $T_1=T_2$. Accordingly, only three independent parameters (T_{tr} , T_1 , T_3) are required to describe the laser-generated nonequilibrium rovibrational distribution in the CO_2 molecules.

In addition to being a compact descriptor of the vibrational level population distribution, the vibrational temperature is conveniently related to the infrared emission rates owing to the dependence of emission rates on vibrational level. Consequently, vibrational temperatures, in addition to being well-defined, are the most compact and useful parameters for describing PLIF signal levels. For each vibrational mode, the emission rate of photons at the fundamental energy $k_{\text{B}}\Theta$ can be related in a straightforward manner to that mode's vibrational temperature T_{vib} . First, we note that the Einstein A coefficients for fundamental emission from level v to level $v - 1$ in a harmonic oscillator are proportional to v :

$$A_{v \rightarrow v-1} = vA, \quad (3.8)$$

Where $A \equiv A_{1 \rightarrow 0}$ is the rate of emission from $v = 1$ to $v = 0$ ($A \approx 420 \text{ s}^{-1}$ for the ν_3

mode of CO₂). For simplicity, we assume that emission rates are independent of rotational state. Then the ensemble-averaged emission rate corresponding to fundamental ($\Delta v=1$) transitions is given as a sum of the emission rates for each vibrational level, weighted by each level's population fraction N_v/N :

$$A_{\text{avg}} = \sum_v \frac{N_v}{N} A_{v \rightarrow v-1} = \sum_v \frac{N_v}{N} v A. \quad (3.9)$$

The vibrational energy per molecule e of a harmonic oscillator vibrational level is also proportional to the quantum number v :

$$e = k_B v \Theta, \quad (3.10)$$

and similarly the ensemble-averaged energy per molecule e_{vib} in a harmonic oscillator mode is given by a population-fraction-weighted sum of vibrational level energies:

$$e_{\text{vib}} = \sum_v \frac{N_v}{N} k_B v \Theta. \quad (3.11)$$

Since Equations 3.9 and 3.11 have the same functional form, the ensemble-averaged emission rate per molecule corresponding to single-quantum emission can be shown to be proportional to the energy in that vibrational mode:

$$A_{\text{avg}} = A \frac{e_{\text{vib}}}{k_B \Theta}. \quad (3.12)$$

Equation 3.12 thus relates the fundamental emission from a vibrational mode to the energy contained within that mode.

Given Equation 3.12, the emission rate can be related directly to temperature. The energy of a nondegenerate harmonic oscillator mode can be written as a function of the mode's vibrational temperature [36]:

$$e_{\text{vib}} = \frac{k_B \Theta}{\exp(\Theta/T_{\text{vib}}) - 1}. \quad (3.13)$$

From Equations 3.12 and 3.13, the average fundamental emission rate per molecule for a

vibrational mode can be described as a simple function of the vibrational temperature T_{vib} :

$$A_{\text{avg}} = A \frac{1}{\exp(\Theta/T_{\text{vib}}) - 1}. \quad (3.14)$$

Equation 3.14 can be used to describe the fluorescence yield ψ_{sat} in terms of the laser-induced change in the ν_3 temperature T_3 . Before laser pumping, the system is at equilibrium at temperature T , and the translational, rotational, and vibrational temperatures are equal: $T_{\text{tr}} = T_1 = T_3 \equiv T$. During laser pumping (for which we denote temperatures with an asterisk), the system is driven into a nonequilibrium distribution. Each absorbed $10.6 \mu\text{m}$ photon removes one molecule from the $10^0 0_1$ level (which has one ν_1 quantum of symmetric stretch energy) and places it in the $00^0 1$ level (which has one ν_3 quantum of antisymmetric stretch energy). Consequently the laser excitation causes the ν_1 mode to lose energy and the ν_3 mode to gain energy, and during laser excitation $T_1^* < T_{\text{tr}}^* < T_3^*$. The effect of the laser is to generate a nonequilibrium T_3^* with an attendant increase in emission at $4.3 \mu\text{m}$.

If the laser-perturbed ν_3 temperature T_3^* is assumed constant throughout the pulse, the fluorescence yield ψ_{sat} can be written simply as the difference between laser-perturbed and ambient emission rates multiplied by the exposure time τ :

$$\psi_{\text{sat}} = \left(A_{\text{avg}, T_3^*} - A_{\text{avg}, T} \right) \tau \quad (3.15)$$

Hence the fluorescence yield is given by

$$\psi_{\text{sat}} = A\tau \left[\frac{1}{\exp(\Theta_3/T_3^*) - 1} - \frac{1}{\exp(\Theta_3/T) - 1} \right]. \quad (3.16)$$

Note that the term in brackets is the increase in ν_3 mode energy per molecule caused by laser pumping, normalized by the vibrational energy spacing $k_{\text{B}}\Theta_3$.

Since the pulse energy is high and $k_{\text{laser}} > k_{\text{inter}}$, simple results for the laser-perturbed ν_3 temperature T_3^* can be obtained by ignoring V-T and intermodal V-V transfer and assuming that the excitation fully saturates the transition. In this case, the laser drives the populations in the $10^0 0_1$ and $00^0 1$ levels to be equal. Assuming harmonic oscillators, the vibrational population fractions f of the $10^0 0_1$ and $00^0 1$ levels are simple functions of the vibrational

temperatures and the total vibrational partition function Q_{vib} [36]:

$$f_{11^0 0_1} = \frac{\exp(-\Theta_1/T_1^*)}{Q_{\text{vib}}}, \quad (3.17)$$

$$f_{00^0 1} = \frac{\exp(-\Theta_3/T_3^*)}{Q_{\text{vib}}}. \quad (3.18)$$

Since the populations in the $11^0 0_1$ and $00^0 1$ states are equal during strong laser excitation, from Equations 3.17 and 3.18 we infer that, under conditions of laser-induced saturation, $\Theta_3/T_3^* = \Theta_1/T_1^*$. With this relation, a straightforward analysis leads to a relation for T_3^* as a function of T .

Recall that, before laser excitation, the system is at equilibrium at temperature T , hence $T=T_{\text{tr}}=T_1=T_3$. T_{rot} and T_2 need not be specified since $T_{\text{rot}}=T_{\text{tr}}$ and $T_2=T_1$. During laser excitation, the system is nonequilibrium, so the distribution must be described by three temperatures (T_{tr}^* , T_1^* , T_3^*). From conservation of vibrational energy we have:

$$e_{\text{vib}}^* = e_{\text{vib}} + \frac{N_{\text{p,abs}}}{N} k_{\text{B}} (\Theta_3 - \Theta_1), \quad (3.19)$$

which states that the difference between the vibrational energies during (e_{vib}^*) and before (e_{vib}) laser pumping is equal to the number of photons absorbed per molecule ($N_{\text{p,abs}}/N$) times the photon energy ($k_{\text{B}} (\Theta_3 - \Theta_1)$). The number of absorbed photons is given by the difference between the ν_3 mode energy during and before the laser pulse:

$$\frac{N_{\text{p,abs}}}{N} k_{\text{B}} \Theta_3 = \frac{k_{\text{B}} \Theta_3}{\exp(\Theta_3/T_3^*) - 1} - \frac{k_{\text{B}} \Theta_3}{\exp(\Theta_3/T) - 1} \quad (3.20)$$

The vibrational energies for CO_2 may be written as follows (note that ν_2 is doubly degenerate):

$$e_{\text{vib}} = \frac{k_{\text{B}} \Theta_1}{\exp(\Theta_1/T_1) - 1} + \frac{2k_{\text{B}} \Theta_2}{\exp(\Theta_2/T_2) - 1} + \frac{k_{\text{B}} \Theta_3}{\exp(\Theta_3/T_3) - 1} \quad (3.21)$$

$$e_{\text{vib}}^* = \frac{k_{\text{B}} \Theta_1}{\exp(\Theta_1/T_1^*) - 1} + \frac{2k_{\text{B}} \Theta_2}{\exp(\Theta_2/T_2^*) - 1} + \frac{k_{\text{B}} \Theta_3}{\exp(\Theta_3/T_3^*) - 1}. \quad (3.22)$$

Equations 3.20, 3.21 and 3.22 may then be substituted into Equation 3.19. Using both

$T_1^* = T_2^*$ and $T_3^*/\Theta_3 = T_1^*/\Theta_1$, we obtain:

$$\frac{\Theta_1}{\exp(\Theta_1/T)-1} + \frac{2\Theta_2}{\exp(\Theta_2/T)-1} + \frac{\Theta_1}{\exp(\Theta_3/T)-1} = \frac{\Theta_1}{\exp(\Theta_3/T_3^*)-1} + \frac{2\Theta_2}{\exp(\Theta_3\Theta_2/\Theta_1 T_3^*)-1} + \frac{\Theta_1}{\exp(\Theta_3/T_3^*)-1} . \quad (3.23)$$

Equation 3.23 can be solved for T_3^* as a function of T , and Equation 3.16 can then be used to predict the fluorescence yield.

The results for T_3^* and ψ_{sat} as a function of temperature are shown in Figure 3.7. Both properties increase with temperature. These results are independent of bath gas constituents and have temperature dependence that, while significant since the transition occurs between excited states, is easily calculated *a priori*. Saturation of the absorption transition

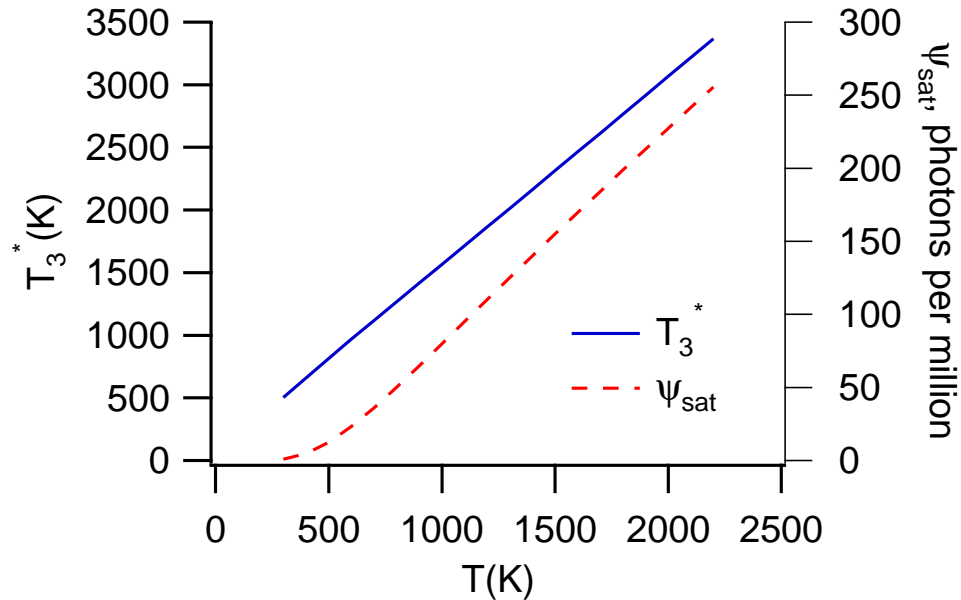


Figure 3.7: Predictions of the three-temperature model for the laser-pumped ν_3 mode temperature (T_3^* , [K]) and the fluorescence yield (ψ_{sat} , [photons per million CO_2 molecules]) as a function of initial temperature .

minimizes laser intensity dependence, since stimulated emission competes with stimulated absorption. Collecting laser-prompt fluorescence (*i.e.*, collecting fluorescence only during the laser pulse) minimizes vibrational energy transfer rate dependence, since the upper vibrational level population during the exposure is controlled by the saturated excitation, and

vibrational level dynamics play only a second-order role. Thus ψ_{sat} is essentially unaffected by the efficiency of VET mechanisms that deplete the upper vibrational level. This independence with regard to VET rates is in contrast to ϕ_{lin} , which can be inversely proportional to excited state deexcitation rates (see Chapter 2), and makes saturated excitation an attractive means of simplifying PLIF signal interpretation.

Detailed VET modeling confirms the quantitative accuracy of the three-temperature model and its simplifying effect on the interpretation of PLIF signal. The detailed VET model discussed in Appendix C (approximately 80 vibrational levels and 14,000 energy transfer processes) has been used with pump laser source terms to integrate excited state lifetimes over the camera exposure time and generate predictions for ψ_{sat} as a function of flow parameters. Results for pure CO₂ are shown in Figure 3.8, which compares predictions from the simple three-temperature model to results of two detailed calculations. These

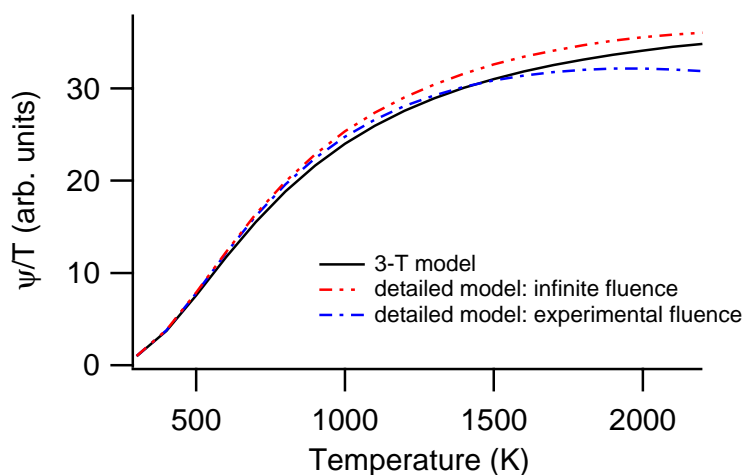


Figure 3.8: Comparison of LIF signal levels at constant CO₂ mole fraction as predicted by the three temperature model and a detailed rate equation model. For the detailed model, results are shown for both finite (corresponding to typical PLIF experiments) and infinite fluences.

detailed calculations for this case were performed with and without anharmonicity in the CO₂ vibrational manifold with negligible effect and show that the three-temperature model successfully matches fluorescence signal predicted by a detailed VET model. Hence the approximations of the three-temperature model (vibrational modes which are independent

and harmonic, $T_1=T_2$, $T_{\text{tr}}=T_{\text{rot}}$) are deemed accurate.

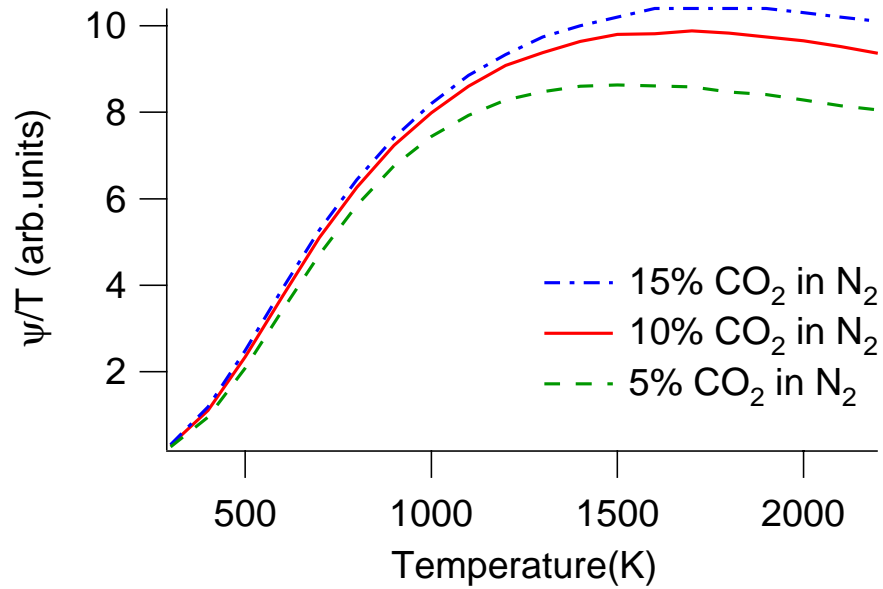
In addition to confirming the validity of the three-temperature model, the detailed rate equation model predicts the variation of IR PLIF signal with laser power or changes in the collisional bath. The IR PLIF signal generated by the laser fluences used experimentally are almost completely saturated—experimental signal levels are within 15% of those expected for completely saturated (infinite fluence) excitation. Changes in laser intensity, CO₂ mole fraction, or H₂O mole fraction that change signal levels by one or two orders of magnitude in the linear limit [32] do not strongly affect signal (typically within $\pm 15\%$) in the saturated limit. Evidence of this is presented in Figure 3.9, which shows how ψ_{sat}/T changes as CO₂ and H₂O concentrations are varied. These CO₂ and H₂O variations lead to changes in VET rates over two orders of magnitude. Thus saturated excitation techniques may confidently be applied to flows with large variations in CO₂, N₂, or H₂O levels which would render uninterpretable the LIF signal resulting from linear excitation.

3.3.4 Experimental Setup and Techniques: Saturated Excitation

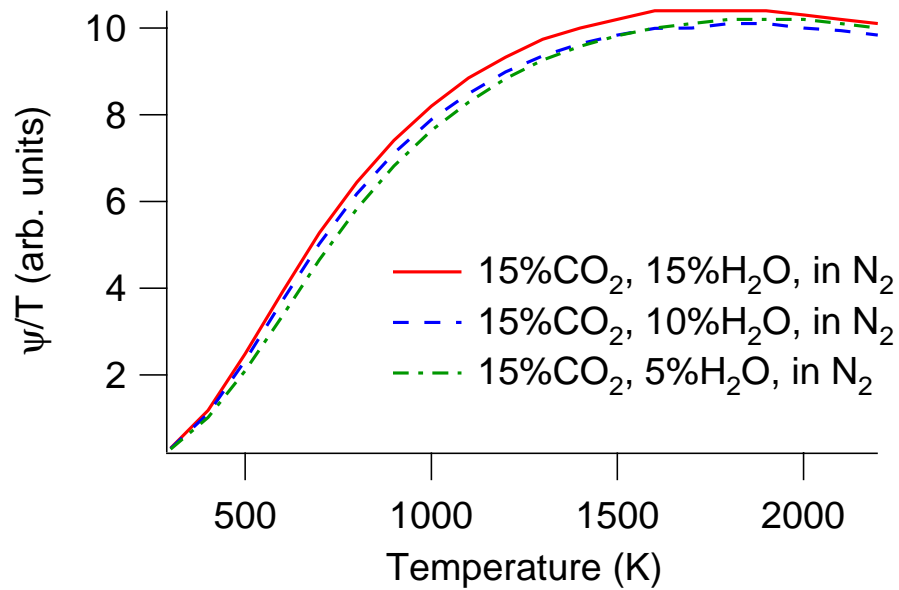
The basic experimental setup shown in Figure 3.10 is used to demonstrate the utility of TEA CO₂ laser excitation and confirm the validity of the previous analyses. The CO₂ laser¹ generates pulses at 10.6 μm with energy up to 5 J. These pulses correspond primarily to the P(20) transition of the $00^0_1 \rightarrow 10^0_1$ emission band at 944.194 cm^{-1} , with small contributions (10%) from the P(18) and P(22) transitions at 945.980 and 942.383 cm^{-1} respectively.

For imaging experiments, the CO₂ laser output was expanded and formed into a sheet using aluminum-coated or BaF₂ optics. Sheet thickness was 570 μm at the focal point with an effective Rayleigh range of 3 cm. Local laser fluence throughout the images varied by a factor of two due to laser spatial profile nonuniformity and sheet focusing. Spatial resolution perpendicular to the laser sheet is estimated to be 1200 μm due in part to saturation effects (which give the spatial distribution of LIF signal a larger FWHM than the beam waist FWHM). For the 11 cm \times 11 cm images here, in-plane resolution is limited by optical aberrations and pixel crosstalk and is estimated to be 1400 μm .

¹Lasertechnics Blazer 2000



(a)



(b)

Figure 3.9: IR PLIF signal normalized by CO₂ mole fraction for saturated excitation of CO₂. Effects of CO₂ and H₂O mole fraction. (a) effect of CO₂. (b) effect of H₂O.

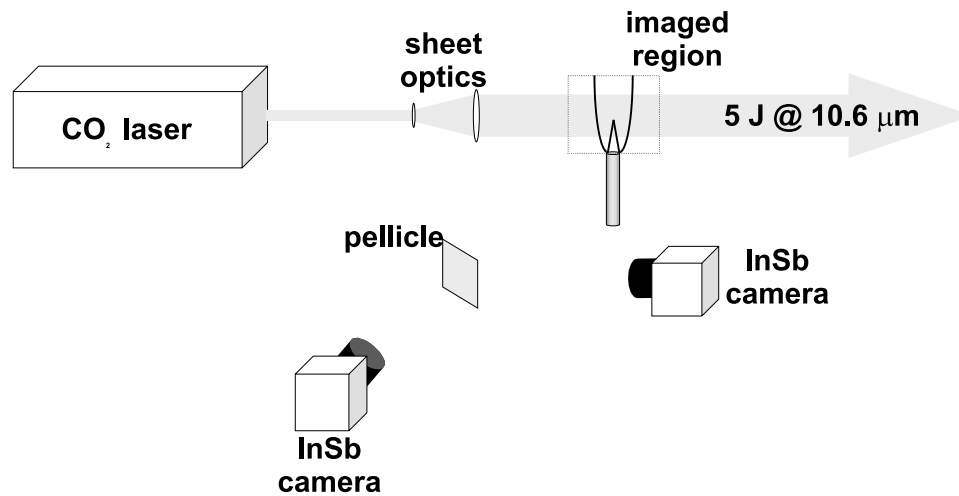


Figure 3.10: Experimental setup for saturated IR LIF PLIF measurements.

Fluorescence was imaged through 4.1–4.5 μm interference filters onto one or two 256×256 InSb cameras² with quantum efficiency of 0.85, variable exposure time (minimum 300 ns), and 14-bit dynamic range. Only one camera is required to generate the IR PLIF image; however, in flows with luminous backgrounds, a second camera is triggered before the laser pulse and used to record and subsequently reject flow luminosity that is present in the absence of laser excitation. Details of dual-image techniques have been described previously [9, 26]. Since IR PLIF signal in the saturated limit is proportional to the sheet thickness, IR PLIF images of the flowfield are also normalized by averaged reference images of a uniform-concentration, isothermal flowfield. This normalization eliminates spatial signal variations caused by changes in sheet thickness.

3.3.5 Imaging Results—Saturated Excitation

Saturated IR PLIF imaging of CO₂ is presented in this section for two demonstration flows, which show the ability of saturated IR PLIF of CO₂ to visualize both low- and high-temperature flows. Following this, visualization of a laminar diffusion flame with known solution is used to address the quantitative accuracy of saturated IR PLIF measurements.

²Santa Barbara Focalplane SBF 134

Demonstration Flows

PLIF images are presented for two simple test cases. As a low-temperature demonstration, a 425 K, unsteady, transverse CO₂ jet ($d = 7$ mm) in an air crossflow was imaged using a two-camera technique; background luminosity is quite minor ($S/B = 20$) for this flow but was nonetheless removed with the second camera. Exposure times of $2 \mu\text{s}$ were used. The background image was triggered $4 \mu\text{s}$ before the PLIF image, giving an overall temporal resolution of $6 \mu\text{s}$. A sample result is shown in Figure 3.11. Signal

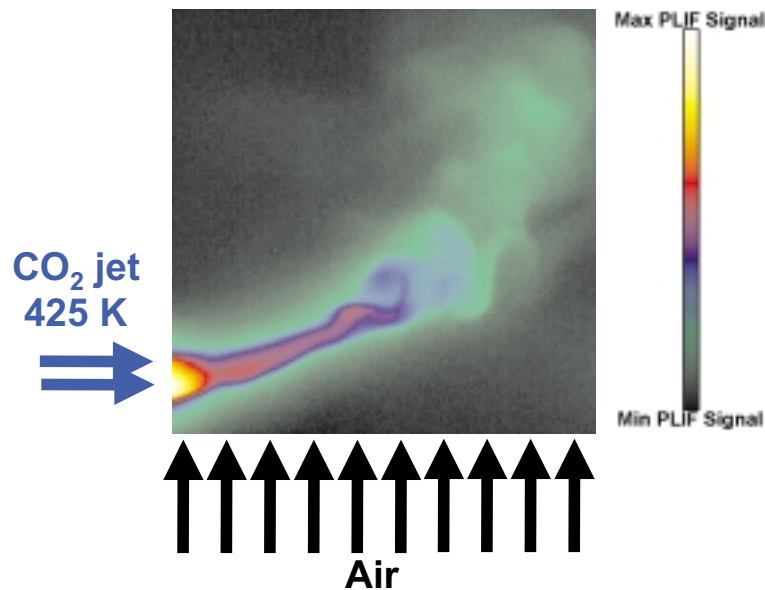


Figure 3.11: CO₂ IR PLIF imaging of an unsteady transverse 425 K CO₂ jet in an air coflow.

is proportional to CO₂ concentration, with minor variations caused by variations in fluorescence yield. For this flow, which features large gradients, the effect of fluorescence yield variations on the apparent structure of the flow is minor. Peak SNR for these single-shot images is typically 50, and the minimum detectable concentration at 425 K, 1 atm is 2.7×10^{17} molecules/cm³ (1000 ppm mole fraction). Signal in these images is proportional to the CO₂ mole fraction and ψ_{sat}/T .

In addition to visualization of low-temperature mixing processes such as shown in Figure 3.11, IR PLIF imaging using a CO₂ laser is capable of visualizing high-temperature

flows. CO_2 was imaged in a flame fueled primarily by a 50%CO/50%Ar mixture (2% H_2 added for stability). A single-camera technique was used in this case, since the flow was steady and images at camera framing rates (in this case 20 Hz) could be reliably subtracted. The camera was exposed for the first $1 \mu\text{s}$ of the laser pulse. Results are shown in Figure 3.12. Peak SNR for single-shot images is typically ~ 6 , and the minimum

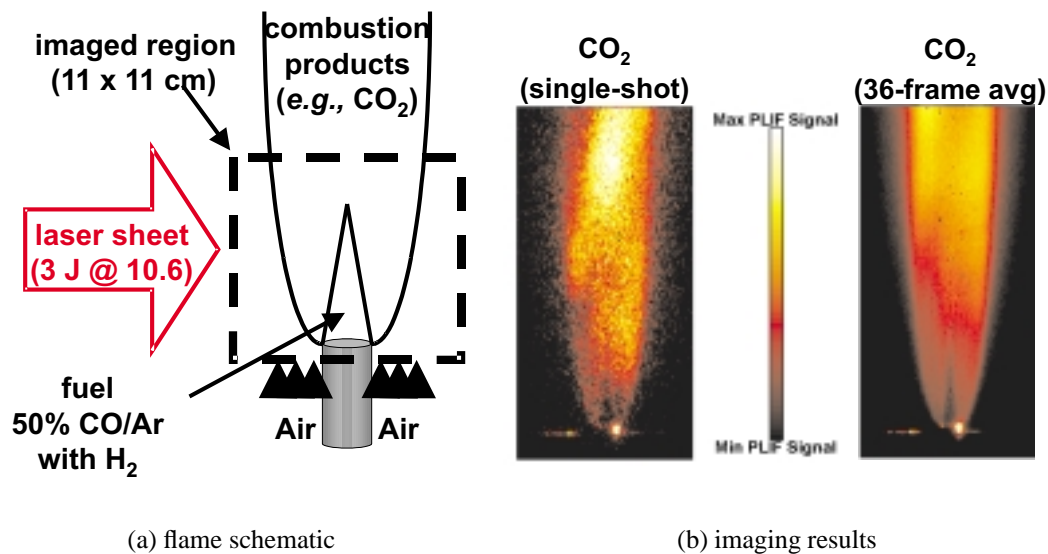


Figure 3.12: CO_2 IR PLIF imaging in a CO/ H_2 flame.

detectable concentration at flame conditions is 1.4×10^{17} molecules/ cm^3 (2% CO_2 mole fraction). Again, signal levels in these images are proportional to the CO_2 mole fraction and ψ_{sat}/T . Note that, while ψ_{sat}/T varies significantly in Figure 3.11, for nascent CO_2 at flame temperatures ψ_{sat}/T is nearly constant, making the fluorescence in Figure 3.12 nearly proportional to the CO_2 mole fraction.

Lifted Laminar $\text{CH}_4\text{-N}_2$ Coflow Diffusion Flame

A laminar coflow diffusion flame (fuel:65% CH_4 /35% N_2 , 4 mm dia., 35 cm/s; coflow: air, 50 mm dia., 35 cm/s) was chosen as a demonstration flame to facilitate quantitative comparison between IR PLIF measurements and accepted results. This lifted, non-sooting flame facilitates computation by eliminating surface quenching and solid-phase chemistry,

and facilitates laser measurements by eliminating blackbody radiation and reducing the impact of laser scatter off burner surfaces and soot particles. Furthermore, since the flame is steady, Raman measurements which in general generate low signal levels can be extensively averaged and line measurements can be overlaid into images. Because of these factors, this flame has been studied computationally and experimentally by researchers at Yale University (principal investigators M.B. Long and M.D. Smooke) and the major species and temperature are well known. Because of this, this flame and the results from Ref. [56] were chosen as a benchmark against which IR PLIF measurements can be compared.

For the purpose of justifying the use of these data as a benchmark, images of computational and experimental results from Ref. [56] for temperature and major species mole fractions in this flame are shown in Figure 3.13. The computational results are generated using standard CFD techniques along with either a simplified kinetic mechanism or GRI-Mech 2.11. Experimental results are generated using 1-D measurements of Rayleigh and Raman scattering that are averaged and overlaid to form images. 170 measurements are overlaid, each an average of 5000 shots. Some limitations of these results may be noted, particularly some minor differences in lift-off height and flame width and somewhat poor agreement for CO and H₂. However, the generally good match between these data sets creates high confidence in their accuracy and makes these values a suitable benchmark against which IR PLIF measurements may be quantitatively compared. Furthermore, these data can be used in conjunction with the vibrational energy transfer modeling discussed in Appendix C to predict the CO₂ fluorescence yield throughout the image and therefore predict the signal levels expected from a CO₂ saturated IR PLIF image. In doing so, the accuracy of the fluorescence quantum yield modeling can be evaluated as well as the ability of the IR PLIF technique to visualize CO₂.

To predict the spatial dependence of fluorescence yield, fluorescence yield was calculated for a variety of species concentrations and temperatures, and results were interpolated as needed to estimate fluorescence yield throughout the image region. Since the computational results are essentially noiseless, they were selected over the Raman measurements for this purpose. Predicted fluorescence quantum yield is shown in Figure 3.14. This figure shows that temperature variations have the most significant effect on the fluorescence quantum yield; however, for the majority of the CO₂-containing region of this flame the

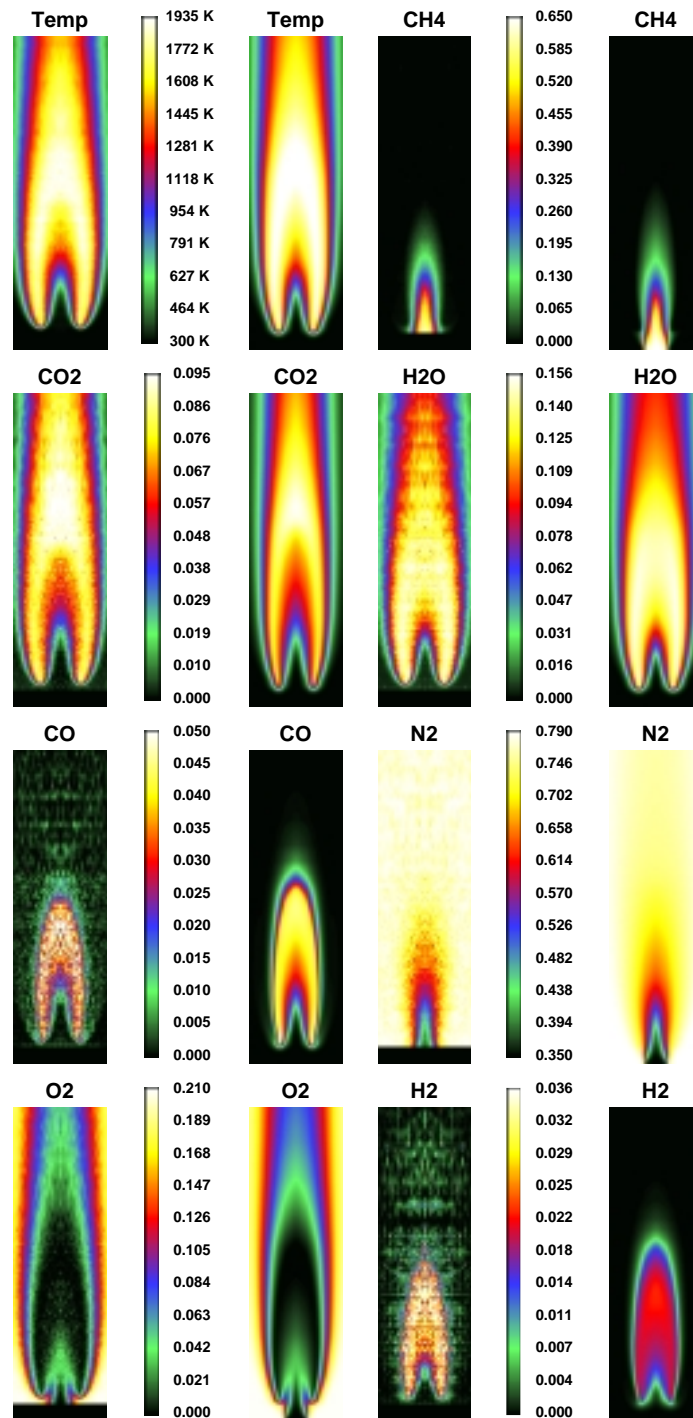


Figure 3.13: Lifted $\text{CH}_4\text{-N}_2$ laminar diffusion flame in air coflow. Temperature [K] and major species mole fractions. For each parameter, Raman images are shown at left and computational data is shown to right. Raman images are generated by averaging and overlaying 850,000 laser shots, corresponding (for a 10 Hz laser) to an approximately 24 hour measurement time. Data from Ref. [56] courtesy of M.B. Long and M.D. Smooke.

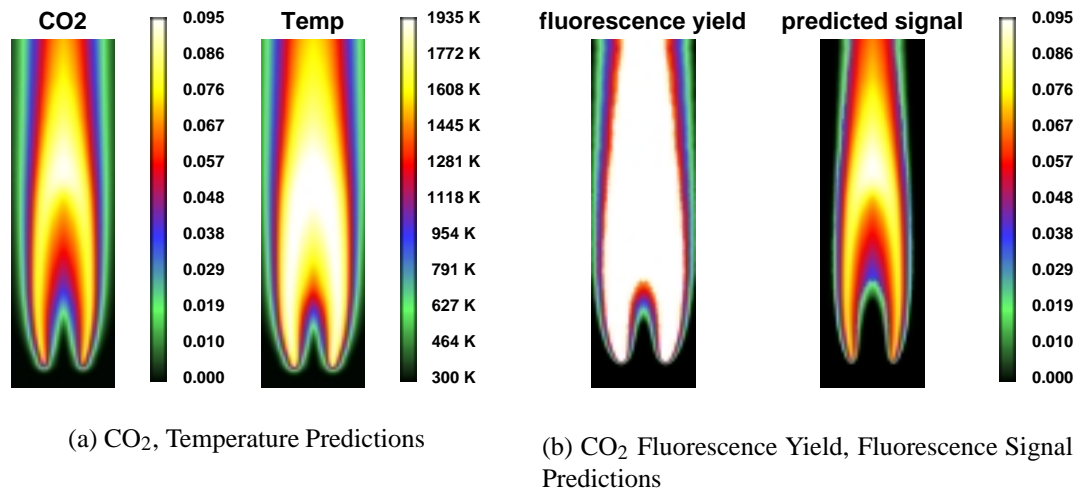


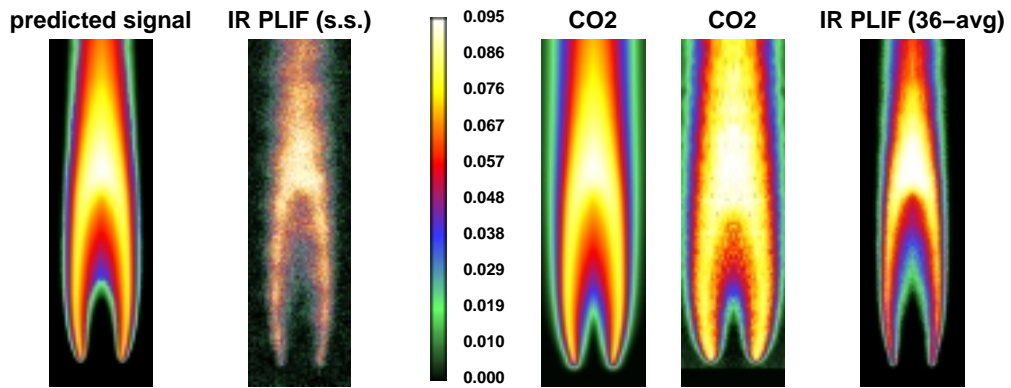
Figure 3.14: Predictions for CO₂ fluorescence yield using the computational data from Figure 3.13 and the fluorescence yield calculations from Appendix C.

fluorescence quantum yield is nearly uniform.

IR PLIF of CO₂ was performed on this flame so the results could be compared to the computational and Raman experiments of Ref. [56]. Results are shown in Figure 3.15 and 3.16. In this case, CO₂ is imaged with SNR=6. A 36-frame average is also presented to facilitate comparison between measured and expected values. As seen in the figure, IR PLIF is able to visualize nascent CO₂ on a single-shot basis with quantitative accuracy comparable to the noise levels. To our knowledge IR PLIF is the only measurement technique with this capability; while the Raman measurements of Ref. [56] are well-suited for quantitative measurements if extensive averaging on a steady flame is acceptable, IR PLIF has the potential to enable straightforward, single-shot visualization of CO₂ in steady and unsteady combustion flows.

3.3.6 Temperature-Independent Excitation Scheme

As is seen in Figure 3.8 indicated earlier, the CO₂ laser excitation scheme leads to fluorescence signal with significant temperature dependence below 1000 K. While this effect is moderate for images of nascent CO₂ in combustion flows (1500-2300 K), mixing processes with varying temperature and cold CO₂ regions motivate design of excitation



(a) Predicted and measured CO_2 IR PLIF signal.

(b) CO_2 predictions/measurements from computations, Raman, IR PLIF.

Figure 3.15: Comparison between IR PLIF, Raman, and computed images of CO_2 mole fraction in a lifted laminar diffusion flame. IR PLIF images are composites of three images.

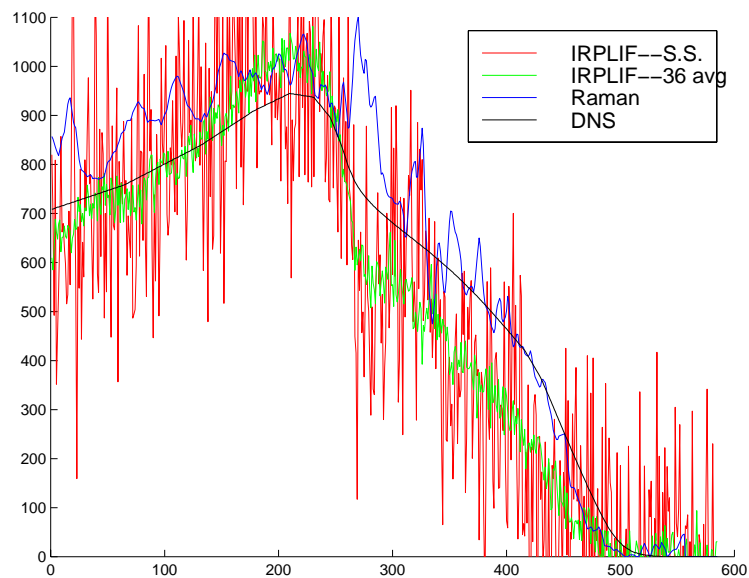


Figure 3.16: Comparison between IR PLIF, Raman, and computed data for CO_2 mole fraction in a lifted laminar diffusion flame. Centerline cut from images in Figure 3.15.

schemes temperature-independent PLIF signal levels. This may be achieved by combining OPO pumping of the $20^0 1_{II} \leftarrow 00^0 0$ transition at $2.0 \mu\text{m}$ with the CO_2 laser pumping of the $00^0 1 \leftarrow 10^0 0$ transition at $10.6 \mu\text{m}$, as is shown in Figure 3.17. Experimental

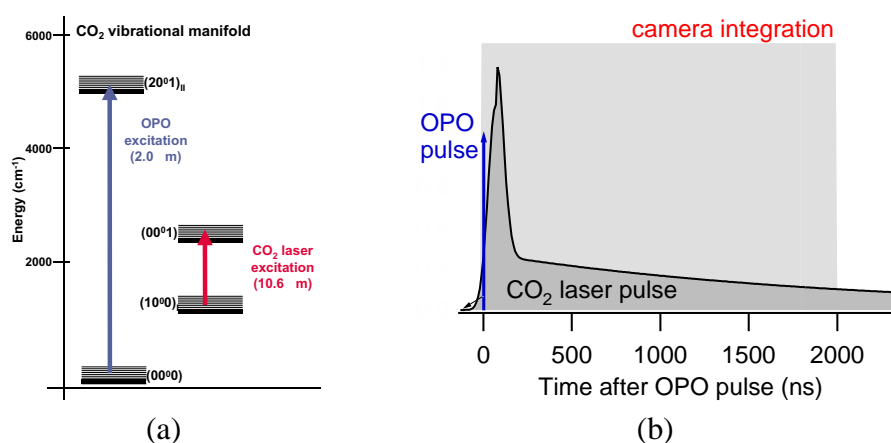


Figure 3.17: Combined OPO- CO_2 laser excitation scheme. (a): excitation steps shown on an energy level diagram. (b): excitation steps shown on a timing diagram.

realization of the $2.0 \mu\text{m}$ pumping scheme is discussed in [32]. The OPO excitation pulse (approximately simultaneous with the start of the CO_2 laser pulse but only 6 ns in length) effectively increases T_1^* ; fast coupling of the $20^0 1_{II}$ and $10^0 0$ states via intramodal energy transfer then leads to an increase in signal. Detailed calculations indicate that experimentally convenient fluences can be chosen such that ψ_{sat}/T is roughly constant with temperature over the range 300–2200 K. We confirmed this by measuring single-point LIF signals at constant mole fraction (which are proportional to ψ_{sat}/T) as a function of temperature and comparing them to the results of the detailed calculation (Figure 3.18). Temperatures up to 900 K were explored. The laser was focused to a $500 \mu\text{m}$ waist using a 150 mm ZnSe spherical lens and LIF was measured in the potential core of a heated 10% CO_2/Ar jet. As can be seen in Figure 3.18, the experimental data match the predictions well. The effect of the OPO excitation step is clear at low temperatures, for which the Boltzmann fraction of the pumped rovibronic state is large and the $2.0 \mu\text{m}$ laser pumping is efficient. At higher temperatures, the effect of the OPO step decreases as the Boltzmann fraction of the pumped rovibronic state decreases; the signal is then dominated by the CO_2 laser pumping. Uniform response with temperature over the wide range shown in Figure 3.18 is

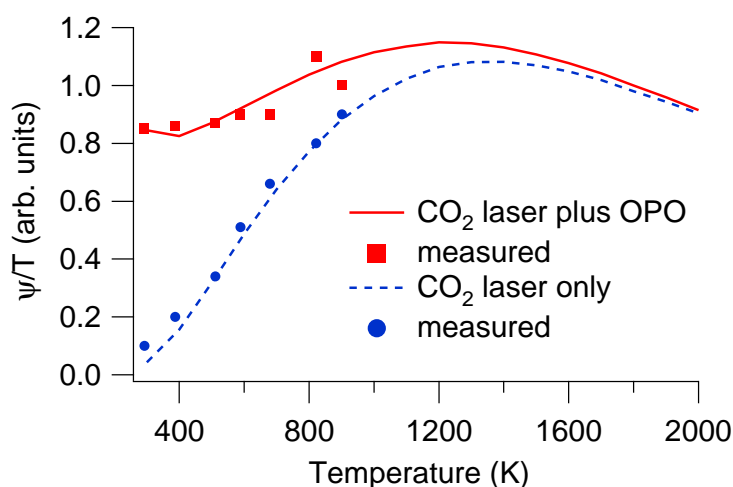


Figure 3.18: LIF signal at constant CO₂ mole fraction as a function of temperature for two excitation schemes. Comparison of calculations with measured results. CO₂ laser excitation is employed in the saturated regime. OPO excitation uses fluence of 20 mJ/cm² on the R(30) line of the 20⁰1_{II} ← 00⁰0 transition. CO₂ laser fluence of 10 J/cm² is used, although excitation is insensitive to this value. Experimental results are relative, and a single normalization parameter is used to match both experimental sets to the calculation.

not achievable using linear excitation (see Section 3.2 or Ref. [32]).

3.4 Conclusions: IR PLIF of CO₂

In this chapter we have presented new IR PLIF imaging techniques for CO₂ which use OPO (2.0 μm) or CO₂ laser (10.6 μm) excitation. For CO₂, 2.0 μm excitation (followed by collection at 4.3 μm) is the best option for linear fluorescence measurements, as it avoids laser attenuation from H₂O and CO₂ (which is observed at 2.7 μm) and nonlinear absorption (which is predicted for typical experimental fluences at 2.7 μm, 9.6 μm, and 10.6 μm). Preliminary results have been presented with 2.0 μm excitation for a 300 K mixing flow; however, the quantitative accuracy of CO₂ images following linear excitation is limited by CO₂'s rapidly-varying partition function and effects of spatially-varying H₂O and N₂ mole fractions on fluorescence quantum yield. The complexity of image interpretation for CO₂ using linear excitation motivates consideration of high-pulse-energy excitation and saturated fluorescence [48].

To simplify CO₂ IR PLIF image interpretation and increase signal levels at flame conditions, saturated IR PLIF imaging techniques for CO₂ have been presented which use a high-pulse-energy TEA CO₂ laser. An examination of energy transfer rates has shown that all rotational states of several vibrational levels ($10^0 0_I$, $10^0 0_{II}$, and $02^2 0$) are pumped indirectly by the TEA laser, since its 2 μ s pulse length is long enough to allow substantial RET and VET to occur during the laser pulse. This energy redistribution along with fast intramodal transfer justifies the use of a simple three-temperature model for analyzing state distributions. When combined with short exposure times provided by our infrared cameras, the long, high-energy pulse makes the fluorescence signal easily interpretable in the context of the three-temperature model. Imaging results from a 425 K unsteady transverse CO₂ jet and a laminar coflowing CO/H₂ diffusion flame have been presented, with minimum detectable concentrations of 2.7×10^{17} and 1.4×10^{17} molecules/cm³ respectively. IR PLIF images of a benchmark lifted, CH₄/N₂-fueled laminar coflow diffusion flame compare well with previous computational and Raman scattering results, and highlight the ability of simple, inexpensive CO₂ lasers to generate high IR PLIF signals suitable for single-shot, high-SNR imaging in a variety of flows.

IR PLIF schemes based on TEA laser excitation alone generate signal that increases with temperature. Calculations over the 300–2200 K range have been confirmed by single-point LIF measurements over the 300–900 K range and show that the addition of an OPO excitation step at 2.0 μ m which pumps the $20^0 1_{II} \leftarrow 00^0 0$ transition may be implemented to generate a fluorescence yield that is nearly independent of temperature over the 300–2200 K range.

Chapter 4

Indirect Excitation Schemes

4.1 Introduction

Recent developments in infrared modifications of PLIF imaging techniques, using both linear [25, 26] and saturated [48] excitation (Chapters 2 and 3), have provided new diagnostic tools for imaging CO and CO₂ in flows of interest to the combustion community. As part of this development, several unique properties of vibrational PLIF measurements have been noted which distinguish it from more traditional electronic PLIF measurements. In particular, the vibrational energy from laser excitation is typically exchanged between species (V-V transfer) more quickly than it equilibrates with translational modes (V-T transfer). This property enables IR PLIF excitation schemes that use a laser source to excite one species (denoted the donor molecule) then collect fluorescence from a different species (denoted the acceptor molecule). These schemes, denoted here as indirect excitation schemes, require that the donor and acceptor be in near-resonance, but offer different benefits than direct excitation and open up new diagnostic possibilities. While the physics behind the dominance of resonant V-V processes over V-T processes has been well known for decades by those studying vibrational energy dynamics, its implication for IR PLIF imaging diagnostics has not yet been explored.

The potential benefits of indirect excitation schemes are threefold: (1) PLIF schemes

that require collisional energy transfer can rigorously mark molecular mixing in under-resolved imaging systems; (2) indirect excitation schemes give PLIF signal that is proportional to the product of species concentrations, which gives the potential for imaging of reaction rates; and (3) collisional energy transfer enables visualization of multiple species with a single laser pulse, which can be used to image multiple species simultaneously or to enable excitation of species with high-pulse-energy, fixed-wavelength laser sources that do not overlap their absorption features. These issues are discussed in the following paragraphs.

Molecular Mixing. Motivated by a desire to rigorously evaluate degree of molecular mixing despite spatially unresolved images, imaging techniques using near-resonant exchange of electronic energy [57] or bath-gas dependent quenching [58, 59] have been proposed. In each case, the generation of phosphorescence (for the former) or elimination of fluorescence (for the latter) required collisions between two particular species and therefore rigorously established mixing on a molecular level, regardless of whether the highest spatial frequency of the scalar field was resolved by the imaging system. In the context of IR PLIF, using an imaging technique that employs near-resonant exchange of vibrational energy to indirectly excite a second species establishes molecular mixing rigorously.

Reaction Rate Imaging. Since traditional PLIF parameters such as species mole fraction or temperature do not always effectively address reaction issues [13], efforts are in place to demonstrate imaging of reaction rate and other indicators [5]. Reaction rates are a product of concentrations of two species (with additional temperature dependence); since PLIF imaging using indirect excitation schemes gives results proportional to species concentration products, it holds the potential to facilitate reaction rate imaging.

Multispecies Imaging; Non-resonant laser excitation. Since V-V transfer enables excitation of species without absorption features resonant with the laser frequency, multiple species may be imaged with a single laser independent of any spectral overlap between the species. Nonresonant excitation enables these species to be imaged simultaneously, and enables species to be imaged despite a lack of resonance with the laser. Since infrared PLIF techniques at high temperatures are in many cases facilitated by high-pulse-energy laser excitation in the saturated regime [48], fast VET allows other species, *e.g.*, CO to be indirectly excited by a CO₂ laser via exchange with CO₂.

This chapter will introduce the theory of indirect excitation schemes and present preliminary imaging results demonstrating the feasibility of IR PLIF imaging using indirect laser/VET pumping. Features that differ from the direct excitation schemes in Chapters 2 and 3 will be highlighted.

4.2 Theory

A simplified energy diagram is shown in Figure 4.1, illustrating a typical IR PLIF excitation scheme and the relevant energy transfer processes that affect PLIF signal. As

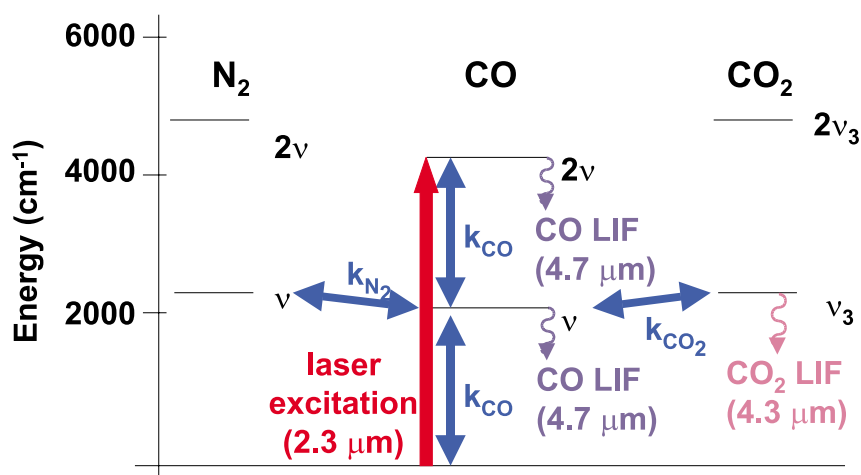


Figure 4.1: Simplified energy diagram of relevant energy transfer processes that affect PLIF signal following indirect excitation.

shown in the figure, infrared laser excitation of combination, difference, or overtone transitions perturbs the vibrational distribution of the pumped species and the nonequilibrium fundamental emission is collected using IR cameras. Vibrational energy transfer processes control the magnitude and spectral distribution of the emission.

As was discussed in Chapter 2, V-V transfer tends to be fast as compared to V-T transfer due to the small energy gaps involved. Infrared (vibrational) PLIF techniques are thus of note in that vibrational energy is exchanged between molecules more quickly than it is converted to rotational and translational energy. This is analogous to the behavior of certain ketones for spin-forbidden (phosphorescent) electronic transitions [57], but is in

marked contrast to typical electronic fluorescence schemes for di- and triatomics for which E-E transfer is relatively inefficient [60].

In modifying the techniques of Chapters 2 and 3 for application using indirect schemes, the fluorescence quantum yield ϕ or the fluorescence yield ψ need be modified, while other parameters remain the same. The following sections will discuss the changes in ϕ and ψ due to indirect excitation.

4.2.1 Linear Excitation Schemes

Recall that, for linear (weak) excitation, the fluorescence quantum yield is defined as the number of emitted photons normalized by the number of absorbed photons:

$$\phi_{\text{ind}} = \sum_j \int_0^\tau \frac{\Delta N_j(t)}{N_{\text{p,abs}}} A_j dt. \quad (4.1)$$

The fluorescence quantum yield of the indirectly excited species is denoted as ϕ_{ind} for indirect schemes, and the excited states j and Einstein coefficients A_j are understood to apply to the indirectly excited species. With these definitions, the fluorescence equation is written as:

$$S_{\text{f,ind}} = N_{\text{p,inc}} n_{\text{abs}} \sigma \ell \phi_{\text{ind}} \eta_c. \quad (4.2)$$

Note that n_{abs} is the number density of the absorbing species while ϕ_{ind} is evaluated for the fluorescing species. Because this form separates the effects of laser energy, absorption, and collection efficiency from the energy transfer processes, the only parameter which changes between Equations 2.5 and 4.2 is that ϕ_{lin} is replaced with ϕ_{ind} .

To generate relations for ϕ_{ind} , the model four-level system from Chapter 2 may again be used (Figure 2.8 is repeated here as Figure 4.2). In this case, however, the species are denoted donor and acceptor, and fluorescence is collected from the acceptor molecules. In the limit of fast V-T transfer or short exposure times, the acceptor molecules emit little or no fluorescence and indirect excitation schemes are not useful. However, when the system exchanges vibrational energy between molecules quickly, but loses vibrational energy to the translational and rotational modes slowly, the V-V transfer is quickly equilibrated, while the V-T transfer is frozen. In this case, the equilibrium between levels 6 and 7 is described

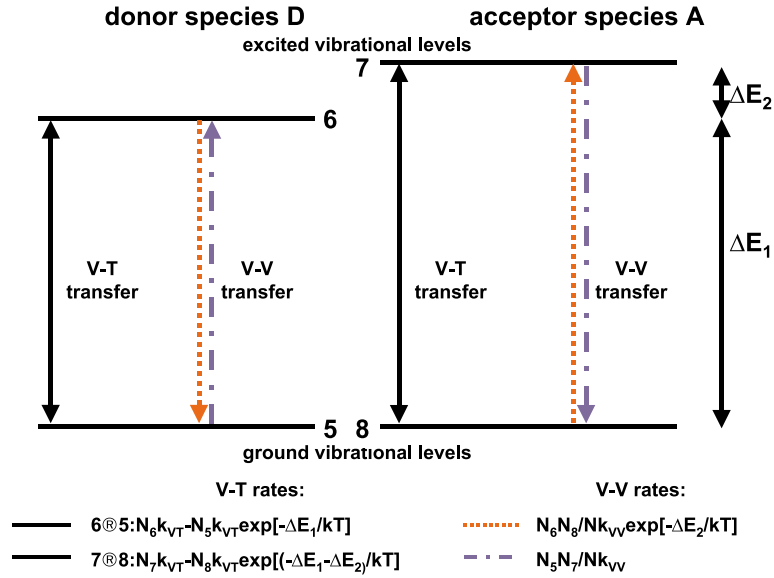


Figure 4.2: VET rates for model four-level system. Radiative transfer is a minor energy transfer mechanism and is omitted from this figure.

by detailed balance:

$$N_5 N_7 / N = N_6 N_8 / N \exp(-\Delta E_2 / kT). \quad (4.3)$$

The vibrational energy, which was initially added to the donor molecules via laser excitation, is now shared between donor and acceptor species in proportion to their mole fractions:

$$N_6 / \chi_D = N_7 / \chi_A \exp(-\Delta E_2 / k_B T), \quad (4.4)$$

Here again it is assumed that the vibrational excitation is small, therefore $N_5 / N \approx \chi_D$ and $N_8 / N \approx \chi_A$, where χ_D is the mole fraction of the donor species D and χ_A is the mole fraction of the acceptor gas species A. The fluorescence from the acceptor molecule is then given by (cf. Equation 2.25):

$$\phi_{\text{lin}} = A\tau \frac{\chi_A \exp(-\Delta E_2 / k_B T)}{\chi_D + \chi_A \exp(-\Delta E_2 / k_B T)}. \quad (4.5)$$

And for small ΔE_2 , this simplifies to (cf. Equation 2.26):

$$\phi_{\text{lin}} = A\tau \frac{\chi_A}{\chi_D + \chi_A}. \quad (4.6)$$

Since the absorption is proportional to the absorber (donor) mole fraction and the fluorescence yield is proportional to $\chi_A/(\chi_D + \chi_A)$, the fluorescence signal is proportional to the product of mole fractions:

$$S_f \propto \frac{\chi_D \chi_A}{\chi_D + \chi_A}. \quad (4.7)$$

For CO-CO₂ schemes, Equation 4.7 predicts that signal levels will be proportional to $S_f \propto \chi_{\text{CO}} \chi_{\text{CO}_2} / (\chi_{\text{CO}} + \chi_{\text{CO}_2})$. When either $\chi_{\text{CO}_2} \gg \chi_{\text{CO}}$, S_f becomes proportional to χ_{CO} . This accurately represents many hydrocarbon flames.

4.2.2 Saturated Excitation

The relations of the previous sections show that indirect excitation has the potential to visualize multiple species; however, the challenges associated with linear PLIF of CO₂ are general for most species. Therefore, indirect excitation schemes in which the absorber is saturated have the most potential for success in hot flows with high water mole fraction. This feature motivates discussion of saturated indirect excitation schemes.

As was the case for linear excitation, the theory for saturated excitation must be adapted to account for indirect schemes. This section will discuss an CO₂-CO indirect excitation scheme since it is compatible with CO₂ laser excitation. For saturated indirect excitation, fluorescence yield ψ_{ind} is defined as the number of emitted photons normalized by the number of absorbing molecules $n_{\text{abs}}V$ in the irradiated volume:

$$\psi_{\text{ind}} = \sum_j \int_0^\tau \frac{\Delta N_j(t)}{n_{\text{abs}}V} A_j dt \eta_c. \quad (4.8)$$

Where j and A_j again refer to excited states and emission rates,, respectively, of the fluorescing species.

Recall from Section 3.3.3 that the fluorescence yield for CO₂ upon saturated excitation

is:

$$\psi_{\text{satCO}_2} = A_{\text{CO}_2} \tau \left[\frac{1}{\exp(\Theta_3/T_3^*) - 1} - \frac{1}{\exp(\Theta_3/T) - 1} \right]. \quad (4.9)$$

this relation stems from the assumptions that the transition is saturated, and vibrational temperatures are well-defined. If the CO is assumed to be in vibrational equilibrium with the ν_3 mode of CO_2 , the fluorescence yield for CO upon saturated excitation of CO_2 is given simply by:

$$\psi_{\text{indCO}} = A_{\text{CO}} \tau \left[\frac{1}{\exp(\Theta/T_3^*) - 1} - \frac{1}{\exp(\Theta/T) - 1} \right]. \quad (4.10)$$

Where Θ is the characteristic temperature of the CO vibrational mode. Since Θ for CO is nearly equal to Θ_3 for CO_2 , CO signal when excited indirectly by laser-saturated CO_2 molecules performs almost identically to CO_2 molecules. However, since the emission rates for CO ($A \approx 35 \text{ s}^{-1}$) are significantly lower than those for CO_2 ($A \approx 420 \text{ s}^{-1}$), CO imaging using this technique can be expected to be less sensitive.

4.3 Results

Preliminary results are presented in this section to demonstrate the feasibility of IR PLIF measurements using indirect excitation.

4.3.1 Room-Temperature Mixing

Excitation of CO at $2.35 \mu\text{m}$ followed by near-resonant V-V transfer to CO_2 has been used to visualize CO_2 in a room-temperature mixing process (Figure 4.3). In this figure, a forced 6-mm jet flow similar to that of Figures 2.13 and 3.4 was used to generate vortex rings of jet fluid (24% CO_2 /38% CO/38% Ar) which then mix with the ambient air. Typical maximum SNR in these images is 200 and is limited in this case by the quality of the pixel responsivity calculation. A minimum detectable mole fraction of 960 ppm CO_2 may be inferred from the measured signal levels.

While the flow in Figure 4.3 generates high-SNR images due to the large mole fractions, the unique properties of indirect excitation schemes are demonstrated by showing a flow in

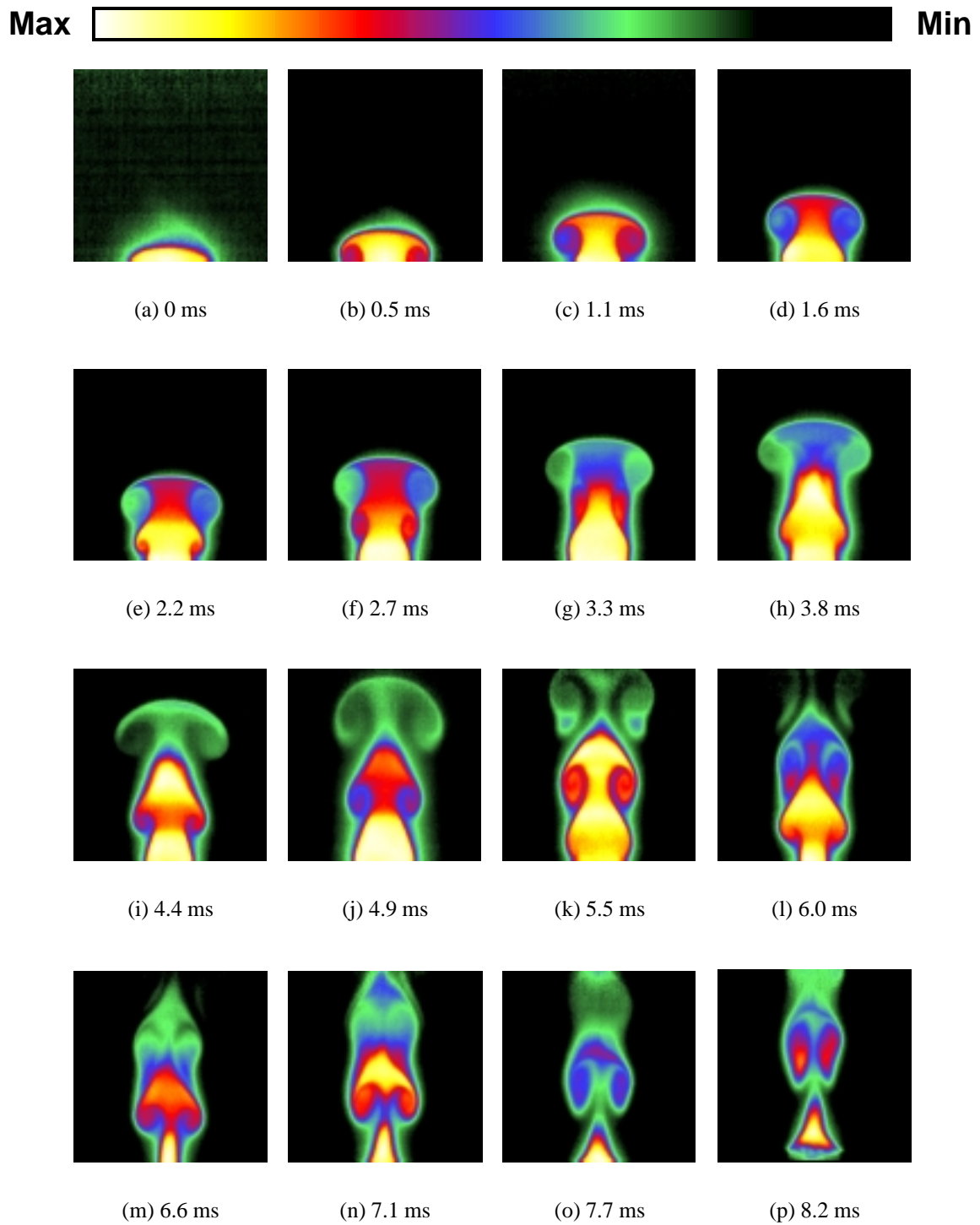


Figure 4.3: Single-shot IR PLIF images of vortex rings developing from a 6 mm tube. Jet fluid is 24%CO₂/38%CO/38%Ar. Ambient gas is air. 12 mJ at 2.35 μ m is used to excite the CO. Integration time is 20 μ s. Images are collected at 10 Hz and the flow is phase-locked to allow a time series to be generated.

which the donor species mixes with the acceptor species. A room-temperature CO_2 jet in a coflow of 50% CO/Ar was visualized by using $2.35 \mu\text{m}$ laser light to excite the $R(7)$ line of the 2ν band of CO . Fluorescence from CO_2 at $4.3 \mu\text{m}$ is collected by the camera. Results are shown in Figure 4.4 . Fluorescence in this case indicates jet fluid which has mixed with

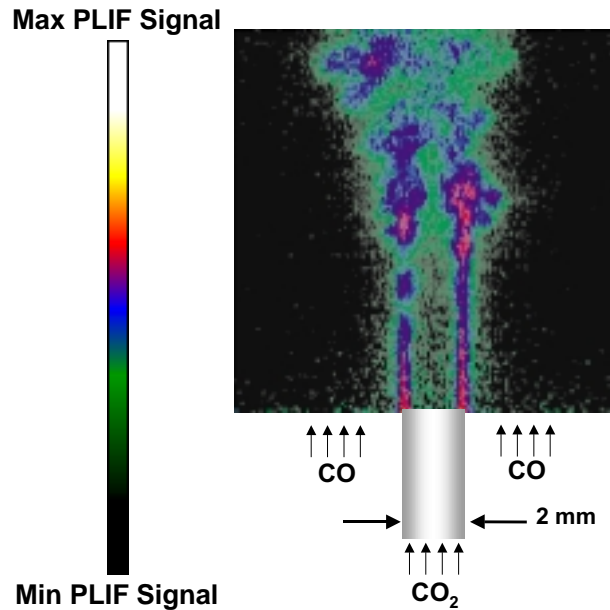


Figure 4.4: CO_2 jet in CO coflow visualized using OPO excitation of CO ($9 \text{ mJ}@2.35 \mu\text{m}$) and resonant V-V transfer to CO_2 . $1 \mu\text{s}$ exposure time. Signal indicates jet fluid that has mixed with the coflow.

the coflow.

4.3.2 Fuel-Product Overlap in a $\text{CO}/\text{Ar}/\text{H}_2$ flame

As a high-temperature demonstration, a steady laminar diffusion flame fueled primarily by a 50% $\text{CO}/50\% \text{Ar}$ mixture (2% H_2 added for flame stability) was imaged using OPO excitation of CO . In this case, the $R(12)$ line of the 2ν band of CO was excited using 12 mJ pulses generated by the OPO system. With a $4.6\text{--}5.1 \mu\text{m}$ filter, the camera recorded CO signal, which is proportional to $[\text{CO}]$ plus a temperature-dependent cross-section. With a $4.1\text{--}4.5 \mu\text{m}$ filter, the camera recorded CO_2 signal, which is proportional to $[\text{CO}][\text{CO}_2]$, and the temperature-dependent absorption cross-section. Results are shown in Figure 4.5.

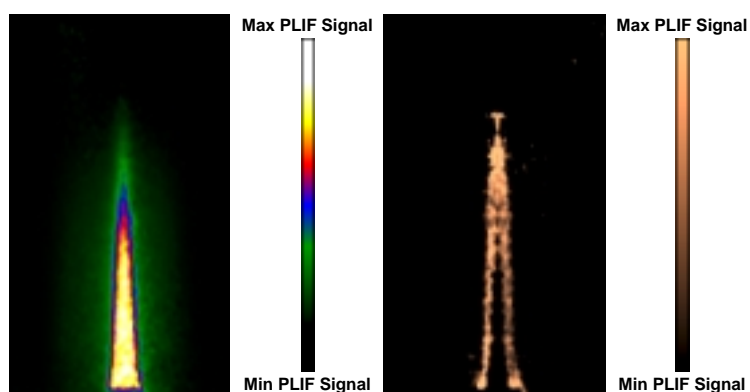


Figure 4.5: Images of fuel (CO) and fuel-product overlap (CO_2) in a CO/H_2 flame. Left: single-shot CO image. Right: 25-frame average CO_2 image. 9 mJ excitation at $2.35 \mu\text{m}$ is used for both images.

Given the signal dependences on concentration, the CO image indicates the fuel region while the CO_2 image indicates the overlap of fuel and product regions. In this flow, CO persists through the flame region, but the fuel-product interface appears as a thin sheet due to the temperature dependence introduced by the absorption cross-section (see Figure 2.11) and number density.

4.4 Conclusions: Indirect Excitation Schemes

This chapter has presented the theoretical framework and preliminary results for new IR PLIF imaging techniques for CO and CO_2 which use OPO or CO_2 laser excitation followed by rapid V-V transfer to excite species vibrationally. Indirect excitation opens up possibilities for sub-resolution measurement of mixing, reaction rate imaging, multispecies imaging, and saturated excitation of species not resonant with high pulse-energy lasers.

Indirect excitation schemes require rapid V-V transfer stemming from near-resonance in the vibrational frequencies of the acceptor and donor species. Fortunately for combustion applications, CO and CO_2 exhibit this near-resonance, enabling either species to serve as an acceptor or donor for indirect excitation.

Depending on the type of excitation scheme (linear or saturated), ϕ or ψ need be modified to account for changes in the fluorescence signal owing to collection of fluorescence

from the acceptor rather than the donor molecule. In both cases, this modification is relatively straightforward in common limits.

Linear excitation schemes that excite CO and collect CO₂ fluorescence give signal that is proportional to the quantity $\chi_{\text{CO}}\chi_{\text{CO}_2}/(\chi_{\text{CO}} + \chi_{\text{CO}_2})$; this quantity has been shown to match well the relative distribution of χ_{CO} in the lifted laminar diffusion flame studied in Chapter 3. Saturated schemes that excite CO₂ and collect CO fluorescence can be explained using vibrational arguments analogous to the three-temperature model of Section 3.3.3. Such schemes give the potential for straightforward measurements of CO mole fraction in certain flames.

Results are presented in two room-temperature mixing flows that show the ability of indirect excitation schemes to generate high signal and to provide sub-resolution measurements of molecular mixing. A laminar coflow diffusion flame fueled by a 50%CO/50%Ar mixture is also used to demonstrate visualization of fuel (directly excited CO) and the fuel-product interface (indirectly excited CO₂).

Chapter 5

Conclusions and Future Work

This dissertation has introduced IR PLIF as a new diagnostic method. In addition, this work has presented the first demonstrations of infrared (IR) PLIF measurements of CO and CO₂, the first detailed analysis of LIF diagnostic strategies for these species, the first results using saturated laser excitation, and the first techniques that use a combination of laser and energy transfer excitation processes. These diagnostic developments enable single-shot visualization of these species in reactive atmospheric pressure flows in a manner not before possible. Since IR PLIF is, in principle, applicable to all IR-active species, IR PLIF has high potential for expanding the diagnostic possibilities available to combustion researchers. Such diagnostics might include visualization of the preflame (fuel) region of lifted flames, CO formation regions in flames, or exhaust mixing processes in internal combustion engines as applied to residual-induced autoignition studies.

The following sections will offer suggestions for future work, then outline the conclusions from Chapters 3–5 and summarize the results.

5.1 Future Work: extending IR PLIF to other species

While this dissertation limits the discussion to imaging of CO and CO₂, IR PLIF has the potential to visualize any species with infrared absorption features. Three areas for future IR PLIF target species, namely methane, water, and large hydrocarbons, are discussed in the following sections.

5.1.1 IR PLIF of Methane

Initial IR PLIF results suggest that CH_4 measurements are feasible in a variety of combustion flows, especially to characterize the pre-flame region of lifted flames. Such measurement capability provides tools to assist modelers attempting to establish correlation or causality between flow properties (*e.g.*, stoichiometry, strain rate) and flame location/stability. IR PLIF of CH_4 has the potential to eliminate the need for flow tracers that might only approximate fuel location, or that might affect flow properties and kinetic mechanisms.

Excitation

Depending on the image size and CH_4 mole fraction, excitation of CH_4 may be achieved via the $\nu_3 + \nu_4$ absorption bands near $2.3 \mu\text{m}$ (Figure 5.1) or the ν_3 band at $3.3 \mu\text{m}$ (Figure 5.2). As can be seen from Figures 5.1 and 5.2, the CH_4 absorption spectra have Q

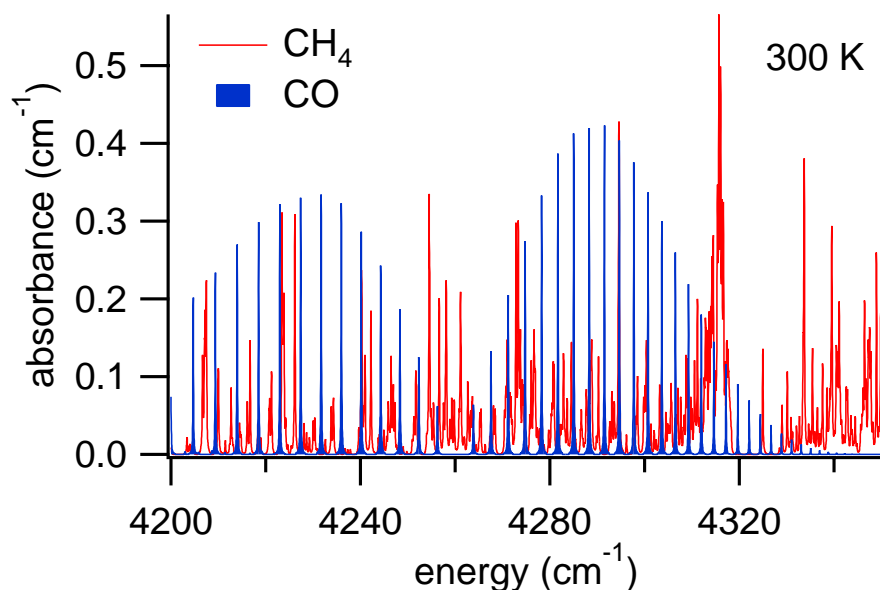


Figure 5.1: Calculated (using HITRAN96 [29]) CO and CH_4 absorption spectra near $2.3 \mu\text{m}$ at 1 atm . The CO absorption feature corresponds to the 2ν absorption band, while the CH_4 feature corresponds to the $\nu_3 + \nu_4$ band.

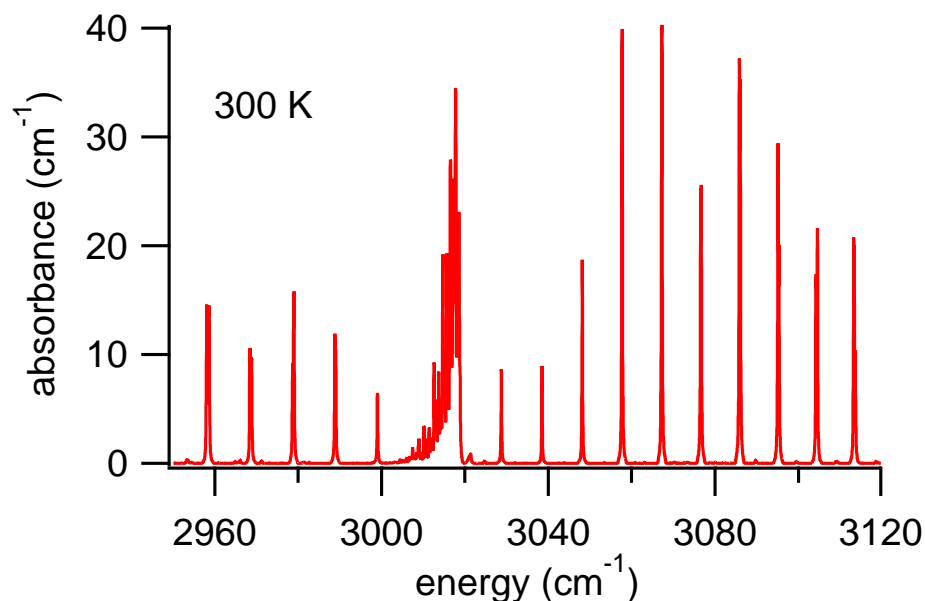


Figure 5.2: Calculated (using HITRAN96 [29]) CH_4 ν_3 band absorption spectra near $3.3 \mu\text{m}$ at 1 atm.

branches which enable excitation with broadband sources if desired. Figure 5.1 also indicates that CO absorption, while present in this spectral region, may be avoided at moderate pressures. Fluorescence can be collected at the ν_3 ($3.3 \mu\text{m}$) or ν_4 ($7.6 \mu\text{m}$) fundamentals. A sample excitation/collection scheme is shown in Figure 5.3, in which excitation at $3.3 \mu\text{m}$ is followed by fluorescence at both $3.3 \mu\text{m}$ and $7.6 \mu\text{m}$.

Vibrational Energy Transfer and Fluorescence Collection

Collecting the fundamental ν_4 emission near $7.6 \mu\text{m}$ is ideal owing to the long ν_4 collisional lifetime in methane ($\sim 1.6 \mu\text{s}$ at 1 atm[30]). Low signal levels are to be expected from fluorescence collected at the fundamental ν_3 emission wavelength ($3.3 \mu\text{m}$) since near-resonant intermodal V-V transfer to the $2\nu_2$, $2\nu_4$, and $\nu_2+\nu_4$ levels is rapid [30, 61]. Calculations with the ν_4 lifetime and emission rate lead to the promising detectivity calculations shown in Figure 5.4, which compare favorably with those achievable through CH_4 Raman imaging efforts. These calculations assume a long exposure time, with fluorescence quantum yield given by $\phi_{\text{lin}} = A/Q$ and $Q(300\text{K}) = 6 \times 10^5$. This collection

scheme can employ strong fundamental transitions for both excitation ($3.3 \mu\text{m}$) and collection ($7.6 \mu\text{m}$), but detection requires short-exposure mercury cadmium telluride (HgCdTe) focal plane technology, which is not as well-developed as that for indium antimonide. Since long-wave infrared (LWIR) cameras with advanced gating capabilities comparable to our current IR cameras will likely become available in the next year or two, they should enable CH_4 visualization using this technique.

5.1.2 IR PLIF of Large Hydrocarbons

While the theory presented in this thesis is primarily suited for analysis of small (diatomic or triatomic) species, high-pulse-energy laser excitation of broadband-absorbing hydrocarbons has potential due primarily to the ease of the excitation process.

Large hydrocarbons in general exhibit fast vibrational energy transfer [62], so high-pulse energy lasers will most likely be required to successfully visualize large hydrocarbons. Many large hydrocarbons (including most paraffins and ketones) have absorption features at $10.6 \mu\text{m}$ or $9.6 \mu\text{m}$ consistent with the output of a high-pulse-energy CO_2 laser and features at $5.3 \mu\text{m}$ consistent with the output of a high-pulse-energy CO laser.

Also, for those species that have accessible ultraviolet transitions, ultraviolet excitation may be used leading to vibrational nonequilibrium which is then observed via IR fluorescence. This has been performed in a preliminary fashion using 266-nm excitation of acetone [63]. Such schemes have the advantage that their signal should be independent of whether the excited electronic state is predissociative, although it should be noted that electronic techniques are most likely preferred for species with accessible electronic transitions.

Saturated excitation is difficult for large hydrocarbons owing to the extremely fast VET rates. For these molecules, the most fruitful analytical technique will most likely be an energy conservation analysis in which the energy input from the laser and energy output from V-T equilibration reach a steady-state during which broadband fluorescence due to the nonequilibrium vibrational energy may be collected.

5.1.3 IR PLIF of Water

Due to water's ubiquity as a combustion product, IR PLIF imaging of water has the potential for high impact. Excitation of water is quite straightforward, as H₂O has strong absorption bands near 1.4 μm , 1.8 μm , and 2.7 μm . In the interest of allowing for red-shifted fluorescence at 2.7 μm as well as minimizing adverse effects of laser attenuation, the 1.4 μm and 1.8 μm bands are the most likely excitation bands. Since H₂O is by far the strongest absorber in this spectral region, interfering species would be expected to have little or no effect on PLIF signal.

V-T transfer in H₂O is very fast (see Appendix C), so H₂O can be expected to face the same challenges for linear excitation that are faced by CO₂, namely that the fluorescence quantum yield will be a strong function of the local H₂O concentration, and that the vibrational and rotational partition function changes with temperature will make it difficult to design schemes that provide for straightforward image interpretation. As was the case for CO₂ at combustion conditions, successful IR PLIF imaging of H₂O will most likely involve saturated excitation using a high-pulse-energy laser or high-pulse-energy Raman-shifted laser. H₂O fluorescence could be collected at 2.7 μm or 6.3 μm , each of which would be expected to have similar relaxation times. For example, the same excitation scheme used earlier in this report to image CO₂ in flames could also be used (with different timing) to image H₂O (in fact, it could be used to image any species. H₂O's broad band structure would make rejection of broadband luminosity more difficult

5.2 Future Work: IR PLIF in Varying Environments

Since future work using IR PLIF will most likely involve other environments, including high- or low-pressure systems with windowed enclosures, this section briefly summarizes the major issues related to applying IR PLIF in those environments.

5.2.1 Varying Pressures

This dissertation has focused on atmospheric-pressure applications, although many applications at other pressures exist. A large fraction of combustion processes occur at elevated pressures, including combustion in IC engines, for which CO₂ PLIF may be applied to study exhaust reinduction. Regardless of the excitation scheme, increased pressure brings challenges due to laser attenuation and fluorescence attenuation due to radiative trapping. However, the dependence of LIF signal on pressure depends on the strength of the excitation process.

The dependence of LIF signal in the linear and saturated limits can be determined by examining the fluorescence equation in its varying forms. Recall that the fluorescence equation for linear excitation may be written as:

$$S_{f,\text{lin}} = N_{p,\text{inc}} n_{\text{abs}} \sigma \ell \phi_{\text{lin}} \eta_c . \quad (5.1)$$

The dependence of important terms on P is as follows: n_{abs} is proportional to P . The peak of the Lorentzian lineshape function is inversely proportional to P in the collisionally broadened limit, therefore σ is inversely proportional to P . Fluorescence quantum yield is proportional to a limiting time (camera exposure time or vibrational relaxation time) that scales inversely with VET rates and therefore scales inversely with pressure; therefore ϕ_{lin} is inversely proportional to P . In total, then, signal levels for IR PLIF using linear excitation can be expected to scale to first order as $1/P$.

For saturated excitation the fluorescence equation is as follows:

$$S_{f,\text{sat}} = \psi_{\text{sat}} n_{\text{abs}} V \eta_c . \quad (5.2)$$

The dependence of signal on pressure in the saturated limit is straightforward, since saturation implies that ψ_{sat} is independent of pressure. The only effect on PLIF signal is that of number density which scales linearly with P . Signal levels for IR PLIF using saturated excitation can thus be expected to scale linearly with P . This feature makes saturated excitation schemes attractive for higher-pressure applications. As pressure increases, the laser energy required to saturate the transition will increase; however saturated excitation with

Material	Knoop Hardness [kg/mm ²]	Thermal Expansion Coefficient [1/K]
ZnS	210	5e-6
Fused Silica	500	14e-6
Sapphire	1370	6e-6

Table 5.1: Material properties for several optical materials.

typical CO₂ laser sources is feasible below 5 atm.

5.2.2 Windows

Applications at non-atmospheric pressure require enclosures that allow laser access via windows. For applications using OPO techniques, this may easily be achieved using sapphire windows, which transmit to 6 μm , are strong, and are resistant to chemical reaction. For applications using CO₂ laser excitation, sapphire absorbs at 10.6 μm and is unsuitable; ZnS windows are the most likely window material since ZnS is non-hygroscopic, much harder than ZnSe, and, due to its moderate thermal expansion coefficient, resistant to thermal shock. Properties of materials are summarized in Table 5.1.

Regardless of the material used, windows attenuate laser light and increase the inhomogeneity of the incident laser sheet. However, successful use of ZnS windows to enable IR PLIF in non-atmospheric conditions appears feasible.

5.2.3 Hot Surfaces

Combustion enclosures can be expected to be hot and therefore emit at IR wavelengths. While this contributes to the noise of an IR PLIF technique, the use of narrowband filters which is typical for IR PLIF measurements will minimize this effect, and emission from hot surfaces should dominate over gas emission only if the walls are hotter than the gas.

5.3 Conclusions

IR PLIF of CO

The IR PLIF technique has been demonstrated using model calculations and IR PLIF imaging of CO. Design procedures for excitation schemes as well as analysis required to interpret IR PLIF imaging of CO have been presented. A model four-level system is used to conceptually describe the behavior of IR PLIF signal, highlighting differences in the functional form of IR PLIF signal depending on the relative length of time scales for camera exposure, V-T transfer, and V-V transfer. Integration of vibrational level populations as calculated with a rate equation analysis is used to quantify fluorescence quantum yield and its dependence on bath gas temperature and species constituents.

For CO, excitation at $2.35\ \mu\text{m}$ followed by a $1\ \mu\text{s}$ camera integration at $4.7\ \mu\text{m}$ generates high signal levels while eliminating laser scattering, laser attenuation, radiative trapping, and fluorescence quantum yield variations. The vibrational energy transfer is slow enough in CO that microsecond-scale integration times provided by modern IR camera systems effectively freeze the vibrational populations and make the fluorescence quantum yield approximately independent of the collisional environment. The $R(12)$ and $R(24)$ lines are demonstrated to generate nearly temperature-independent signal within the 300–800 K and 800–2200 K regions, respectively. A detailed rate equation analysis of the transient absorption process and collisional RET shows that typical experimental fluences reside within the linear regime and standard PLIF post-processing techniques may be used. While a detailed MEG scaling law analysis is required to properly predict LIF signal at very high fluences, a simple four-level (two-rate) model is sufficient to confirm linearity of LIF signal for the moderate fluences relevant to planar imaging. Predictions of signal and noise levels indicate that IR PLIF is sensitive enough to enable single-shot imaging of nascent CO in flames. Results have been presented for room-temperature mixing flows and fuel visualization of laminar diffusion flames, showing the potential for IR PLIF for imaging of CO.

IR PLIF of CO₂

New IR PLIF imaging techniques for CO₂ have been demonstrated using OPO (2.0 μm) or CO₂ laser (10.6 μm) excitation. For CO₂, 2.0 μm excitation (followed by collection at 4.3 μm) is the best option for linear fluorescence measurements, as it avoids laser attenuation from H₂O and CO₂ (which is observed at 2.7 μm) and nonlinear absorption (which is predicted for typical experimental fluences at 2.7 μm , 9.6 μm , and 10.6 μm). Preliminary results are presented with 2.0 μm excitation for a 300 K mixing flow; however, the quantitative accuracy of CO₂ images following linear excitation is limited by the rapid temperature variation of the CO₂ partition function and spatial variation of fluorescence quantum yield due to inhomogeneous H₂O and N₂ mole fractions. The complexity of image interpretation for CO₂ using linear excitation motivates consideration of high-pulse-energy excitation and saturated fluorescence [48].

To simplify CO₂ IR PLIF image interpretation and increase signal levels at flame conditions, saturated IR PLIF imaging techniques for CO₂ are presented using a high-pulse-energy TEA CO₂ laser. An examination of energy transfer rates shows that all rotational states of several vibrational levels (10^0_0I , 10^0_0II , and 02^2_0) are pumped indirectly by the TEA laser, since its 2 μs pulse length is long enough to allow substantial RET and VET to occur during the laser pulse. This energy redistribution along with fast intramodal transfer justifies the use of a simple three-temperature model for analyzing state distributions. When combined with short exposure times provided by our infrared cameras, the long, high-energy pulse makes the fluorescence signal easily interpretable in the context of the three-temperature model. Imaging results from a 425 K unsteady transverse CO₂ jet and a laminar coflowing CO/H₂ diffusion flame are presented, with minimum detectable concentrations of 2.7×10^{17} and 1.4×10^{17} molecules/cm³ respectively. IR PLIF images of a benchmark lifted, CH₄/N₂-fueled laminar coflow diffusion flame compare well with previous computational and Raman scattering results, and highlight the ability of simple, inexpensive CO₂ lasers to generate high IR PLIF signals suitable for single-shot, high-SNR imaging in a variety of flows.

IR PLIF schemes based on TEA laser excitation alone generate signal that increases with temperature. Calculations are confirmed by single-point LIF measurements over the

300–900 K range and show that the addition of an OPO excitation step at $2.0 \mu\text{m}$ which pumps the $20^0 1_{II} \leftarrow 00^0 0$ transition may be implemented to generate a fluorescence yield that is nearly independent of temperature over the 300–2200 K range.

Indirect Excitation Schemes

The theoretical framework and preliminary results for new IR PLIF imaging strategies for CO and CO₂ are presented using laser excitation of one species followed by rapid V-V transfer to excite another species vibrationally. Indirect excitation schemes require rapid V-V transfer stemming from near-resonance in the vibrational frequencies of the acceptor and donor species, but they open up possibilities for sub-resolution measurement of mixing, reaction rate imaging, multispecies imaging, and saturated excitation of species not resonant with high pulse-energy lasers. Fortunately for combustion applications, CO and CO₂ exhibit this near-resonance, enabling either species to serve as an acceptor or donor for indirect excitation.

Depending on the type of excitation scheme (linear or saturated), ϕ or ψ need be modified to account for changes in the fluorescence signal owing to collection of fluorescence from the acceptor rather than the donor molecule. In both cases, this modification is relatively straightforward in common limits. Linear excitation schemes that excite CO and collect CO₂ fluorescence give signal proportional to the quantity $\chi_{\text{CO}}\chi_{\text{CO}_2}/(\chi_{\text{CO}} + \chi_{\text{CO}_2})$; this quantity has been shown to match well the relative distribution of χ_{CO} in the lifted laminar diffusion flame studied in Chapter 3. Saturated schemes that excite CO₂ and collect CO fluorescence can be explained using vibrational arguments analogous to the three-temperature model of Section 3.3.3. Such schemes give the potential for straightforward measurements of CO mole fraction in certain flames.

Results are presented in two room-temperature mixing flows that show the ability of indirect excitation schemes to generate high signal and to provide sub-resolution measurements of molecular mixing. A laminar coflow diffusion flame fueled by a 50%CO/50%Ar mixture is also used to demonstrate visualization of fuel (directly excited CO) and the fuel-product interface (indirectly excited CO₂).

5.4 Summary of Results

The results of Chapters 3–5 can be summarized as follows: despite the small Einstein A coefficients associated with vibrational transitions and nonzero excited state populations present at combustion temperatures, IR PLIF is shown to be a straightforward and effective tool for visualization of CO and CO₂ in flows pertinent to combustion. The slow equilibration observed for some vibrational nonequilibria and the large mole fractions for CO and CO₂ in typical flows enable high IR PLIF signal despite low emission rates.

Analyses of RET and VET show that excitation schemes in either linear (weak) or saturated (strong) limits may be developed, and fluorescence may be collected directly from the laser-excited species or indirectly from bath gases in vibrational resonance with the laser-excited species. Use of short ($\sim 1 \mu\text{s}$) exposures (for CO) or short exposures combined with long-pulse, high-pulse-energy excitation (for CO₂) minimizes unwanted signal variation due to spatially-dependent VET rates.

Results have first been presented for near-room-temperature flows, where Boltzmann fractions are high, backgrounds are negligible, and VET rates are typically lowest. Images using OPO excitation show high SNR (up to 200) and minimum detectable mole fractions near 1000 ppm for both CO and CO₂. CO₂ images using a CO₂ laser are less effective near room-temperature due to the low population in the 10^0_1 vibrational level.

Results are also presented for high temperature flows, which are more challenging due to smaller Boltzmann fractions, flame luminosity, and higher VET rates. Linear excitation is suitable for CO due to CO's slow V-T and V-V relaxation and has been demonstrated in a CO-fueled laminar diffusion flame; however, linear excitation is not well-suited for CO₂ imaging due to the complexity of CO₂ signal interpretation. Saturated excitation using CO₂ laser (or combined CO₂ laser-OPO) excitation is most appropriate for CO₂, as it generates high signal and combats spatial variations in fluorescence quantum yield stemming from the effect of H₂O on VET rates. IR PLIF of CO₂ using CO₂ laser excitation is demonstrated in CO- and CH₄-fueled laminar diffusion flames.

Since IR PLIF may, in principle, be used for any species with IR transitions, it has the potential to enable imaging of many species that at present have no suitable imaging diagnostics via UV/visible excitation.

Appendix A

IR PLIF Instrumentation

The equipment and techniques in this report are unique to IR PLIF experiments. Hence, the instrumentation is summarized in this appendix in some detail. Particular attention is paid to the OPO/OPA system, since (a) it has been discontinued and is no longer supported by the vendor; (b) it has been modified in-house; and (c) it is reasonably complicated to operate. This chapter focuses on equipment and techniques associated with the equipment itself; IR PLIF experimental techniques are left for later chapters.

A.1 Infrared Imaging Test Bed

Equipment related to IR PLIF imaging is housed on two optical tables ($4' \times 10'$ and $4' \times 8'$). The $4' \times 10'$ table houses the two laser sources, their power supplies and control equipment, diagnostic equipment for the OPO, an oscilloscope and data acquisition system, and timing equipment. The $4' \times 8'$ table houses the experimental flow, gas handling, exhaust, and camera systems, as well as the majority of the optics for controlling and shaping the laser beams.

A.2 Nd:YAG-pumped OPO/OPA Tunable Infrared Source

This section discusses the OPO source in use at Stanford, but is not a replacement for a background in nonlinear optics, which is extremely useful for anyone using this system.¹

A.2.1 System Overview

The tunable laser source (Figure A.1) is a three-stage OPO/OPA system² pumped by the fundamental and second harmonic outputs of an Nd:YVO₄-injection-seeded Nd:YAG laser.³ The system generates high energies (>20 mJ/pulse near 2.0 μm) in 6 ns pulses at 10 Hz with single-longitudinal-mode (400 MHz) linewidth. Optical parametric ampli-

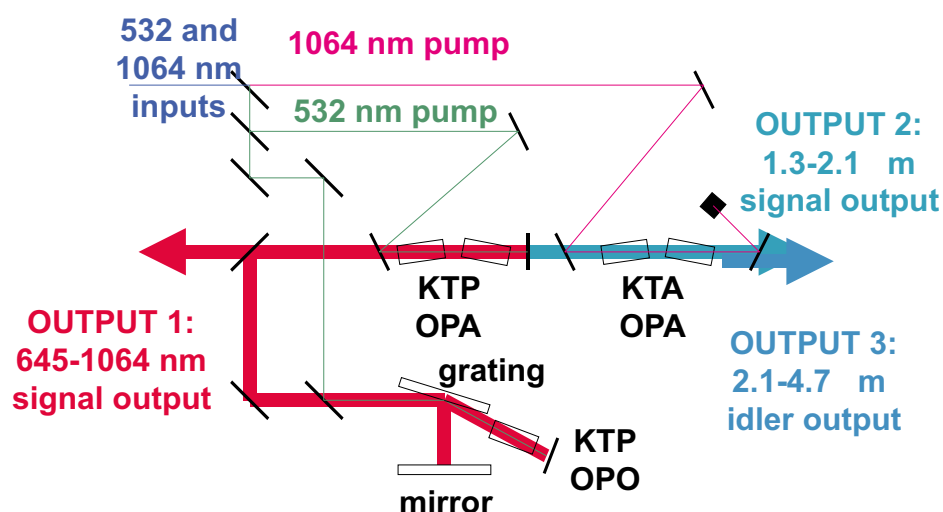


Figure A.1: Tunable infrared source consisting of modified Continuum Mirage 3000 OPO with KTA optical parametric amplifier stages added for increased conversion.

fiers [65] are chosen for this system over laser or stimulated Raman amplifiers owing to their high conversion efficiency, wide tuning range, insensitivity of parametric gain to the spectral properties of the input beams, and absence of parasitic oscillations. This system

¹Useful overviews of the physics of nonlinear conversion using optical parametric processes can be found in Refs. [64, 65]. At Stanford, useful courses include Applied Physics 305, Nonlinear Optics Laboratory and Applied Physics 346, Introduction to Nonlinear Optics.

²Continuum Mirage 3000

³Continuum Powerlite 9000

generates three outputs: (1) the signal output⁴ of the second stage (645–1064 nm), (2) the signal output of the third stage (1300–2128 nm), and (3) the idler output of the third stage (2128–4700 nm). Outputs 2 and 3 are manipulated using dielectric high-reflectors and used for IR PLIF imaging; output 1 is split and monitored with both a Fabry-Perot interferometer and a power meter.

A.2.2 Nd:YAG Pumping

The flashlamps and Q-switch of the Nd:YAG laser are triggered⁵ by a programmable digital delay generator⁶ that is set to trigger internally at 10 Hz. The delay between the flashlamp and Q-switch triggers is set at 450 μ s to maximize the Nd:YAG pulse energy, and the KD*P frequency-doubling crystal is aligned to maximize the 532 nm output. Output triggers from the laser system are recorded by a pulse counter⁷ so as to monitor the number of pulses fired on the flashlamps.⁸ The output pulse energy at the fundamental is approximately 40% of the specified output pulse energy⁹ because the flashlamp energy of the Nd:YAG system is set at a low level. Under-filling the Nd:YAG rods improves the spatial uniformity of the inversion in the rods and also stabilizes the rod temperature distribution. Inversion uniformity and thermal stability is necessary to maintain precise pointing stability and phase coherence in the Nd:YAG output. Oscillation threshold of the OPO is highly sensitive to any deterioration in pointing stability or phase coherence in the Nd:YAG beam. For this reason, experience also shows that Nd:YAG flashlamps should be replaced every 20 million pulses, more often than is specified in the manual. Close attention to the Nd:YAG maintenance schedule (changing cooling water, changing water filters, killing algae in the lines by flushing with hydrogen peroxide) is also required to maintain OPO performance.

⁴Note that standard jargon describes the short-wavelength and long-wavelength beams generated in an optical parametric oscillator as the *signal* and *idler* respectively.

⁵TTL standard trigger

⁶Stanford Research Systems DG535

⁷Fluke 7250A

⁸The laser system records pulses only when triggered internally but not when triggered externally by the DG 535.

⁹specified pulse energy: 2 J; typical output: 800 mJ

The Nd:YAG laser pulses have more energy than can be tolerated by the nonlinear crystal anti-reflection (AR) coatings; therefore a beamsplitter¹⁰ is used to separate 50% of the residual 1064 nm energy and approximately 20% of the 532 nm energy. The residual beam is passed into the OPO/OPA system. Inside the OPO/OPA housing, a dichroic beamsplitter splits the 532 nm and 1064 nm beams which are individually attenuated with half-wave plates and Brewster angle polarizers. 25% of the 532 nm beam (typically 18-22.5 mJ) is split off and passes through a two-lens telescope into the oscillator cavity. The remaining 75% of the 532 nm beam (typically 54-90 mJ) passes through a two-lens telescope into the weakly resonant second stage OPO/OPA. The 1064 nm input passes through a two-lens telescope and spatial filter into the third stage OPA.

A.2.3 In-house modifications

The OPO/OPA system has been modified in-house in four ways: (1) a flipper mirror has been added between the first and second stages, enabling the oscillator output to be outcoupled and analyzed quantitatively with a Fabry-Perot interferometer; (2) the beam waist used in the oscillator cavity has been increased 15%, which improves the spatial homogeneity of injection seeding in the second stage; (3) the third stage KTP (potassium titanyl phosphate) crystals have been replaced with KTA (potassium titanyl arsenate) crystals to reduce idler absorption in the region beyond $\sim 3.5 \mu\text{m}$ [66]; (4) two additional manually-tuned KTA crystals have been added to the third stage to increase the parametric gain.

A.2.4 OPO Performance Diagnostics

The OPO performance is monitored using power meters and Fabry-Perot interferometers. A portion of the oscillator (stage 1) output is fiber-coupled to a lens-etalon interferometer and the interference fringes are recorded by a video rate CCD and interpreted qualitatively via a monitor. In addition, a separate Fabry-Perot interferometer¹¹ is used in either wedged-etalon or lens-etalon¹² configurations to quantitatively monitor the output of either

¹⁰CVI part no. BS1-1064-50-2037-45P

¹¹Burleigh WA-4500

¹²The wedged-etalon configuration is referred to as etalon A, and the lens-etalon configuration is referred to as etalon B, consistent with the Burleigh software and manual.

the oscillator (stage 1) or oscillator/amplifier (stage 2). Here again, fringes are recorded on a CCD and are communicated to a computer for display. The software uses real-time calibration with fixed-wavelength reference lasers to calculate absolute wavelength. The Burleigh interferometer can measure wavelength accurate to 0.02 cm^{-1} . The lens-etalon configuration (etalon B) has the best resolution and can be used to confirm injection-locking of the second stage. After injection-locking has been confirmed, two thermopile power meters are used to measure the energy of the second¹³ and third¹⁴ stages and optimize crystal tuning for maximum pulse energy.

A.2.5 Alignment Techniques

This section discusses alignment techniques that are covered poorly in the equipment manuals or that are specific to the setup at Stanford. The equipment manuals should of course be consulted in addition to the material presented here.

Stage 1: 532-nm Grating-Tuned Oscillator

The first (OPO) stage is a grating-tuned optical parametric oscillator pumped by 532 nm output of the Nd:YAG. The attenuator on the 532 nm input should be used to ensure that the pump pulse energy does not exceed 22.5 mJ as measured by a pyroelectric pulse energy meter;¹⁵ exceeding this level can lead to crystal damage, typically in the form of a damaged AR coating. Once the pump laser is aligned (see manual), the grating should be set to a visible wavelength ($<750 \text{ nm}$), and the KTP crystal can be rotated until the red signal beam can be seen on a card. Laser goggles which block the 532 nm pump beam and effectively pass red wavelengths are needed for this step. Alignment is very temperature-sensitive, so the room temperature should be controlled and changes in room temperature will require realignment. Crystal performance will deteriorate after about a year due to gray tracking [67–69], requiring crystal reorientation or replacement.

¹³Scientech model 360203 head; model 362 readout

¹⁴Scientech model 380101 head; model 362 readout

¹⁵Ophir pyroelectric head model PE-50-BB-DIF, serial no. 37420; NOVA readout, serial no. 38031; visible wavelength calibration

Stage 2: 532-nm Weakly-Resonant Oscillator/Amplifier

The second stage is designed to operate as an amplifier, but the pump pulse energy (~ 90 mJ) is above oscillation threshold for the cavity. Thus the second stage will oscillate independently if it is decoupled from the first stage, and near-IR output will be generated by the second stage regardless of whether it is injection-locked to the first stage. Because the second stage can oscillate, it is important to examine the spectrum of the second stage output to ensure that the second stage is injection-locked before maximizing pulse energy.

Injection-locking of the second stage is confirmed by observing its response to crystal tuning and addition/removal of the first stage seed pulse. When the second stage is decoupled from the first stage (if the system is misaligned or an object is placed to block the first stage output), will be unaffected by the presence or absence of the injection seeding output from the first stage; also the second stage output energy will be only a very weak function of the absolute angles of the second stage crystals, rather will be a function only of the relative angle of the two crystals. Because the second stage is weakly resonant, the cavity mode structure is poorly defined; the linewidth of the second-stage output without injection seeding is controlled by the wavelength acceptance of the phasematching process and is dictated by dispersion. Typical linewidths in this case are 10 cm^{-1} . Output with such a broad linewidth will be correctly measured by the Burleigh interferometer in wedged-etalon mode (etalon A) but not in lens-etalon mode (etalon B).

When the first two stages are operating properly, the second stage amplifies the narrow-linewidth output of the first stage. With proper operation, both the second stage pulse energy (as measured by power meter) and the second stage output spectrum (as measured by the Burleigh interferometer on etalon B setting) are clearly affected by the injection-seeding oscillator pulse. By alternately blocking and unblocking the oscillator pulse (for example, with a business card), an increase in pulse energy of about 20% should be observed due to the seeding pulse. Also, with the seed pulse blocked, the wavelength spectrum that the Burleigh software calculates from the etalon B fringes will be diffuse (*i.e.*, peak heights less than half of FWHM). With the seed pulse unblocked, the wavelength spectrum should show clear peaks (*i.e.*, peak heights more than twice FWHM). Coupling of the first and second stages may also be confirmed by examining the wavelength of the oscillator stage

alone (by using the flipper mirror to outcouple the oscillator output) as compared to the second stage alone (by examining its output with the oscillator blocked). By using the low-resolution (*i.e.*, etalon A) mode of the Burleigh interferometer, both outputs can be alternately monitored. If the system is properly tuned, both wavelengths will be the same. Once it is confirmed that the second stage is amplifying the first stage output, the second stage pulse energy can be peaked by aligning the crystals and monitoring the pulse energy.

Stage 3: 1064-nm Amplifier

The third stage is straightforward since it is configured as a single-pass amplifier. Pump pulse energies of 300 mJ at 1064 nm¹⁶ are typical. Two KTA crystals are actuated by stepper-motor and are controlled by the software. Two manually-tuned KTA crystals have been added and are mounted in Spectra-Physics WEX housings. These crystals may be moved out of the beam path if desired.

Maximum conversion for a parametric amplifier is typically realized through careful collimation of all beams and precise phasematching; however, with the addition of extra crystals, the third stage is effective enough to undergo pump reconversion at beam center during the peak of the pulse. Because of this, the peak output pulse energy is rather insensitive to the degree of collimation. By using slightly expanding or focusing beams, this misalignment (along with the Poynting vector walkoff of the parametric process) can be used to generate a beam which is highly divergent (high M^2 value) and focuses loosely. Loose focusing (and the attendant long Rayleigh range) is desirable for PLIF experiments as it minimizes errors due to focusing-induced irradiance nonuniformity.

A.2.6 OPO Performance—pulse energy

Figure A.2 shows maximum OPO output energy as a function of wavelength as achieved at Stanford following modification. These pulse energies are significantly higher than the energy specifications of the original system. Pulse energies drop away from the degeneracy primarily due to idler absorption in the KTA crystal. When the OPO is used for IR PLIF

¹⁶as measured at the lens telescope, before the spatial filter

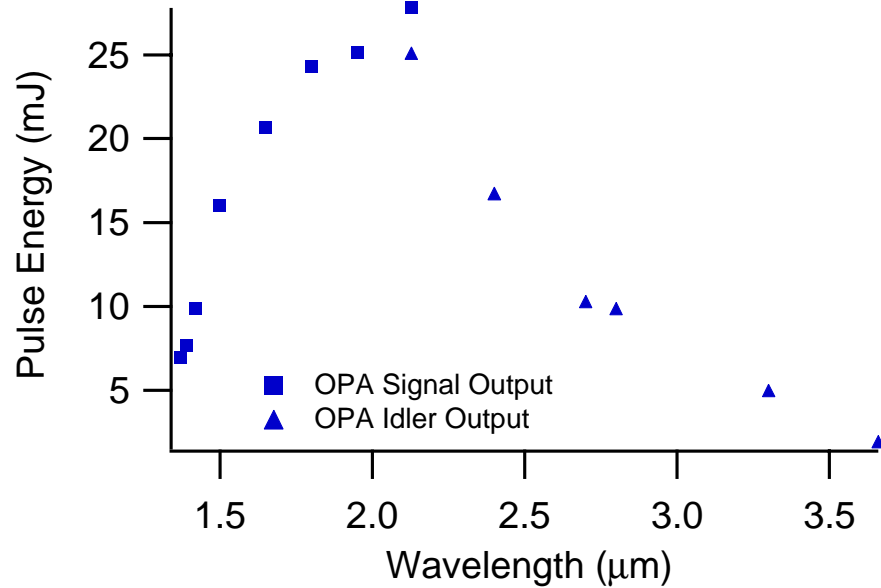


Figure A.2: Optimized output power for modified OPO system. All results are for system optimized for maximum energy.

measurements, priority is placed on pulse stability and spatial performance and typically the pulse energies used are 50-80% of maximum.

A.3 CO₂ Laser

A TEA (transversely-excited atmospheric) CO₂ laser¹⁷ generates pulses at 10.6 μm with energy up to 5 J. These pulses correspond primarily to the P(20) transition of the 00⁰₁ → 10⁰₁ emission band at 944.194 cm⁻¹, with small contributions (10%) from the P(18) and P(22) transitions at 945.980 and 942.383 cm⁻¹ respectively. Contributions from the P(18) and P(22) lines are observed early in the pulse before the P(20) line builds up enough intensity to dominate the cavity gain. The pulse length is typical of TEA lasers, with an early 100 ns FWHM peak followed by a slowly decaying (2 μs) tail (Figure A.3). The output is gain-narrowed to 300 MHz.

¹⁷Lasertechnics Blazer 2000

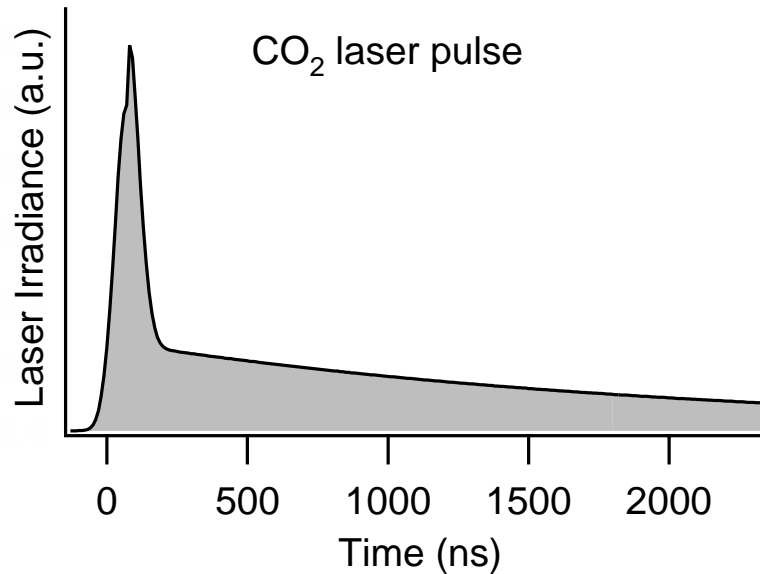


Figure A.3: Typical CO₂ laser pulse shape.

The thyatron (and therefore the laser light) is triggered externally using a pulse generator¹⁸ at rates ranging from 0.6–15 Hz. The performance of the thyatron, which controls the timing of the high-voltage pulse, tends to deteriorate if the laser is not used for a few weeks. In this case the laser will be observed to fire inconsistently, either not firing or firing multiple times with one trigger pulse. This can be improved simply by running the laser for a period of hours to condition the thyatron.

A.4 Infrared Cameras

One or two identical two-channel, LN₂-cooled infrared cameras¹⁹ are used to collect fluorescence. These cameras employ 256×256 InSb focal plane arrays with 30 μm pixels and a quantum efficiency in the 1.0–5.3 μm region of 85–95%. These cameras use a proprietary circuit to achieve enhanced performance for short integration times. Each camera has a four-filter wheel which is also maintained at LN₂ temperature and can be used to switch

¹⁸HP Model 3311A function generator; square wave; 1.5 V amplitude; 0 V offset

¹⁹Santa Barbara Focalplane SBF 134

between different filters without otherwise changing the collection optics. The cameras are each controlled by an independent computer using software from the manufacturer.

A.4.1 Camera Timing

The internal clock rate of the camera system is controlled via the software, and frame rates range from 1–315 Hz. External triggering may be selected via the software so as to synchronize the camera exposures to the laser pulse. When triggering externally, the camera clock rate must be set at a rate *higher* than the external triggering rate.²⁰ When synchronized to the OPO output, the camera is triggered with a 300 ns width TTL pulse from the DG 535 delay generator, and the camera integration begins approximately 750 ns after the rising edge of the input trigger. When synchronizing to the CO₂ laser, the camera is triggered using the current-preamplified antenna response of an open BNC cable placed close to the CO₂ laser so as to respond to the EMF spikes associated with the high-voltage discharge. This triggering approach is used because the jitter in delay between laser trigger and laser pulse can be large.

A.4.2 Camera Noise Performance

The noise performance of the cameras is dependent on framing rate. Since the laser systems used here operate at frequencies between 1–20 Hz, a camera framing rate of 20.1 Hz was typical. At clock rates of 30 Hz and below, typical pixel read noise levels were not a function of clock rate and were approximately 500 photoelectrons per pixel. Noise levels increase beyond 30 Hz and are larger by approximately one order of magnitude as the camera framing rate approaches 300 Hz. Pixel signals are digitized to 16 bits, although the noise level at moderate frame rates corresponds typically to about 6 counts (photoelectrons/count ~ 80), leading to camera bit depth between 13 and 14 bits.

²⁰This has not been quantified extensively, however, it has been observed in general that a camera clock rate which is 0.1 Hz faster than the external trigger rate is sufficient to work.

A.4.3 Camera Calibration

Images of uniform-temperature solid (Lambertian) graybody emitters at different temperatures are used to calibrate individual pixel responsivity, and an on-line correction is applied to the measured signal. Errors caused by approximating the Lambertian emitters as isotropic sources were negligible for the collection optics used here but could be important if extremely fast optics are used.

The camera software allows for a two-point calibration of pixel response, which corrects on-line for responsivity variations due to pixel-specific bias variations or nonuniform collection efficiency. This correction also eliminates pixel offset variations. Some nonlinearities in the camera response can be observed; in particular the response to input signal is not the same on the two channels of the camera. If left uncorrected, every other row will show varying signal levels due to the difference in nonlinearity between odd rows (channel 1) and even rows (channel 2). This can be corrected for by performing a three-point calibration with graybody emission sources of varying temperatures. The correction from the three-point calibration can be applied during image post-processing to eliminate these nonlinearities.

Pixel response could be calibrated with an accuracy of one part in 1000, *i.e.*, errors in pixel calibration lead to an apparent noise source with standard deviation equal to 0.001 times the pixel signal levels. This is in addition to read and shot noise sources. Achieving such accuracy requires that the camera electronics have thermally equilibrated and typically requires an hourly calibration. Daily calibrations lead to pixel responsivity errors around 0.005. High quality calibration is most important when using dual-camera techniques.

A.4.4 Camera Temporal Response

The temporal response of the camera was measured in two ways: (1) with a constant IR source, by measuring the variation of recorded signal levels with software-selected integration time; and (2) with a pulsed source, by measuring the variation of recorded signal levels with delay time. Typical results are shown in Figure A.4, along with estimated responsivity as a function of the software-selected integration time. Camera response was consistent between the two cameras and was independent of triggering method (external vs. internal).

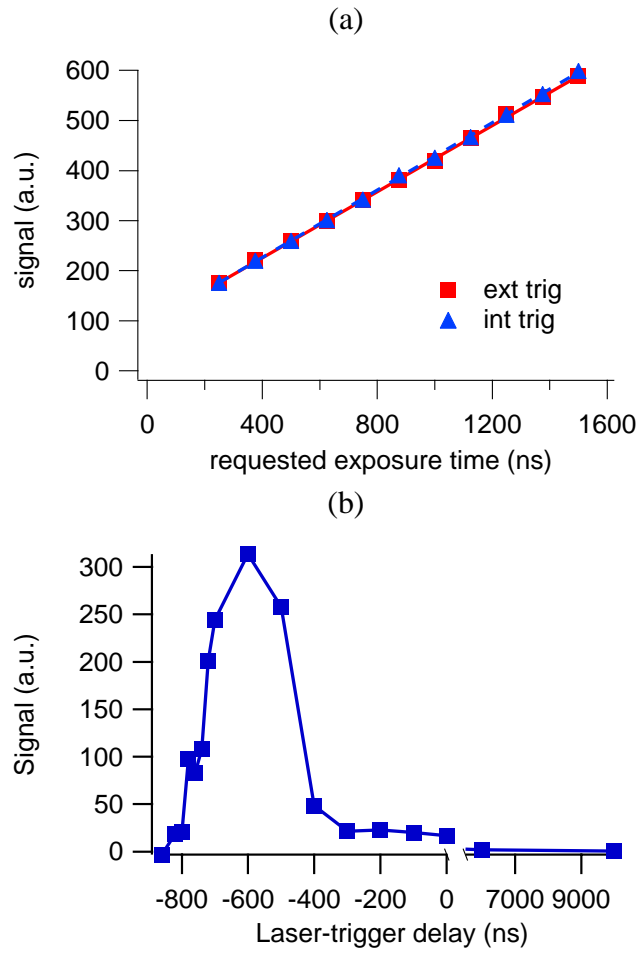


Figure A.4: Camera temporal response. (a) Response to cw source as function of time. (b) Response to delta-function source as function of delay.

From the cw source experiment, it is observed that the camera response is linear for the short ($\sim 1 \mu\text{s}$) integration times typically used for IR PLIF. An offset is present which corresponds to $275 \pm 10 \text{ ns}$. Nonlinearities become apparent after $10 \mu\text{s}$ but do not affect IR PLIF measurements. From the pulsed source experiments, it can be seen that the camera responsivity ramps up to maximum and down to zero in approximately 275 ns . Therefore a simple model for the camera responsivity with time is a trapezoid with 275 ns ramps on either side of a constant-responsivity period whose length is given by the software-selected exposure time. From the figure, it can be seen that the camera response is nonzero even at long delays ($< 5 \mu\text{s}$); thus a small error might be expected if a strong signal exists just outside the camera exposure time. This effect was never observed in experiments reported here.

A.4.5 Camera Resolution

As is typical of 100% fill-factor cameras, the IR cameras do not provide idealized resolution, *i.e.*, charge leaks between nearby pixels and this crosstalk limits resolution. Images of wire meshes taken using slow collection optics (to eliminate aberration as an error source) give a spatial dynamic range of about 80. Camera resolution in the absence of optical aberrations is thus given by $1/80$ times the image size. For image regions smaller than 5 cm , optical aberrations caused by fast singlet lenses can dominate over pixel crosstalk in the outer regions of the images.

A.4.6 Collection Optics

Singlet CaF_2 optics are used to image the fluorescence on the focal plane arrays. Cassegrainian optics were used in some initial studies but perform poorly with this camera system due to the large back focal lengths ($> 2 \text{ inches}$) of the InSb cameras. The large back focal lengths stem from the cold filter wheel, which adds approximately 1 inch to the b.f.l. The diameter of the cold stops on the camera (1 inch) limit the diameter of the collection optics to 1 inch ; in all cases 1 inch optics were used.

Most singlet lenses used were plano-convex; however, $f/1$ and $f/1.5$ lenses, when used, were biconvex to minimize aberrations. Improved performance would be achieved (just

as in visible photography) through the use of multi-element CaF_2 lenses. Such lenses would be simple to design but expensive due to CaF_2 's high cost and bulky due to its low refractive index. For luminous systems (in which lossy lenses do not significantly decrease SNR), Germanium camera lenses are common and would perform well.

A.5 IR Detectors

Four IR detectors are available for point measurements: a 3 mm diameter photoconductive InSb detector²¹ with amplifier²² and three 0.1 mm \times 0.1 mm photoconductive HgCdTe detectors²³ with amplifiers.²⁴ The InSb detector has a 300 kHz bandwidth and a sensitivity range from 1–5 μm , while the HgCdTe detectors have approximately a 70 MHz bandwidth and have sensitivity ranges from 3–6 μm , 3–9 μm , and 3–12 μm respectively.

A.6 DAQ System

The data acquisition system consists of an oscilloscope,²⁵ a boxcar-averager system,²⁶ BNC-DAQ card interface,²⁷ two PCI data acquisition cards,²⁸ and a computer²⁹ running LabView. Fast signals (typically from IR detectors) may be captured on the scope and downloaded via GPIB interface to the computer, or they may be boxcar-averaged and recorded by the 1 kHz, 16-bit DAQ card.

²¹EG&G Judson J10D-M204-R02M-30

²²EG&G Judson PA-9

²³Fermionics models PV-6-100, PV-9-100, PV-12-100

²⁴all model PVA-500-100

²⁵Tektronix 620B

²⁶Stanford Research Systems model SR250

²⁷National Instruments BNC-2090

²⁸National Instruments PCI-MIO-16XE-50, National Instruments PCI-GPIB

²⁹Dell Pentium II 233 MHz

Appendix B

Rotational Energy Transfer

B.1 Introduction

Because laser excitation occurs between specific rovibrational states and induces a nonequilibrium rotational state population distribution, the rate at which this nonequilibrium population distribution equilibrates with the rotational bath affects IR PLIF signal levels. Most notably, IR PLIF techniques often use laser fluences which depart to some degree from the small-perturbation limit. The magnitude of this departure is strongly affected by RET.

To address these issues, this appendix describes rotational states and their notation, rotational energy transfer processes, relations between RET and spectroscopic parameters, and the integration technique and rates used to model RET.

B.2 Rotational States and Notation

For linear molecules such as CO and CO₂, the rotational state is specified by the quantum number j , and the rotational energy to first order is proportional to $j(j + 1)$. To distinguish from vibrational state notation, rotational states are here denoted by specifying j and its value in parentheses. For example, CO in the $j = 14$ state is denoted as CO($j = 14$). Orientation of the angular momentum (as specified by the quantum number m_j) is ignored here, as angular momentum reorientation is assumed to be fast as compared

to other processes.

B.3 RET processes

For the purposes of this discussion, collisional processes are separated into three categories: elastic dephasing collisions, R-T transfer, and R-R transfer. It should be noted that, while energy transfer is described as resulting from “collisions”, this term is used in this context to imply any intermolecular interaction that results in energy transfer and whose rate scales with pressure and translational temperature like a hard-sphere collision rate. The following sections describe the three RET processes in detail.

B.3.1 Elastic Dephasing

Elastic dephasing collisions are collisions that temporarily perturb the wavefunctions of the colliding molecules, but do not change their states. The result of this perturbation (which does not introduce any transfer of energy) is that the phase of oscillation of the wavefunctions is changed. While this process does not involve the transfer of energy, it does have the potential to affect spectroscopic parameters used later in this appendix to infer RET rates.

B.3.2 R-T Transfer

R-T transfer processes allow rotational energy to be exchanged with translational energy. In this case, two molecules collide and one of the molecules undergoes a change of rotational state. The small energy defect is taken up by the translational mode. An example of R-T equilibration is $\text{CO}(j = 12) + \text{M} \leftrightarrow \text{CO}(j = 7) + \text{M}$.

B.3.3 R-R Transfer

R-R transfer processes equilibrate the rotational distribution independent of the translational temperature. In this case, two molecules collide and both of the molecules undergoes a change of rotational state such that the energy defect approaches zero. An example of

R-R equilibration is $\text{CO}(j = 8) + \text{CO}(j = 9) \leftrightarrow \text{CO}(j = 9) + \text{CO}(j = 8)$. R-R transfer implies that the state change each molecule undergoes is dependent on the initial and final rotational states of its collisional partner.

B.3.4 Relative significance of RET mechanisms

RET mechanisms differ from VET mechanisms (cf. Appendix C) in that most RET processes involve internal energy changes that are small compared to the average translational energy of the molecules. Because of this, energy resonances play an insignificant role in rotational relaxation of CO and CO₂ at all but cryogenic temperatures. Furthermore, as will be mentioned later in this appendix, elastic dephasing processes tend to be insignificant for CO and CO₂ at the temperatures relevant here. Consequently, RET processes for CO and CO₂ are well described by ignoring resonance-enhancement (*i.e.*, R-R transfer) or elastic dephasing and using only R-T processes.

B.4 Relation between RET and Spectroscopic Parameters

RET processes are typically measured in one of two ways: (1) state-to-state rate constants may be measured by observing the equilibration of a nonequilibrium rotational distribution prepared by chemical reaction or laser pumping [70–72]; or (2) state-to-state rate constants may be inferred by measuring spectroscopic parameters such as line broadening, line shift, and line mixing [39, 52–54]. The latter will be discussed here.

For simple molecules, a spectral feature (Raman, absorption, stimulated Raman, etc.) caused by N lines can be described in the impact approximation (binary collisions, negligible collision duration) by a relaxation matrix equation [73]. This relaxation matrix W is a complex matrix of dimension $N \times N$ and describes pressure broadening and shift as well as line mixing effects such as Q -branch collapse [39] and super-Lorentzian behavior in bandhead regions [74].

With the additional assumptions that (1) vibrational energy transfer is slow as compared to rotational energy transfer, (2) rotational energy transfer rates are independent of vibrational level, and (3) elastic dephasing is insignificant as compared to rotationally inelastic

collisions, the relaxation matrix formalism provides relations between rotational energy transfer rates and line broadening and mixing. Most notably, line mixing is proportional to rotational energy transfer between individual rotational states, while line broadening is proportional to the summed transfer into or out of a rotational state.

Line broadening can be related to summed rotational transfer rates through Heisenberg uncertainty principle arguments, which give the total uncertainty of a transition in terms of the sum of upper and lower state lifetimes τ' and τ'' :

$$\Delta\nu = \frac{1}{2\pi c} \left(\frac{1}{\tau'} + \frac{1}{\tau''} \right) \quad (\text{B.1})$$

For systems in which the homogeneous (Lorentzian) broadening can be assumed independent of molecular velocity class, *i.e.*, for systems in which the homogeneous and inhomogeneous broadenings can simply be convolved, the Lorentzian broadening FWHM is given by $\Delta\nu$ as specified above. Hence measurements of line broadening translate directly to summed RET rates.

Since RET tends to be fast, many different energy transfer pathways are prominent, and any experiment tends to underconstrain the state-to-state rates, solving for state-to-state rate constants typically requires reducing the dimensions of the optimization through the use of a transfer rate scaling law. Two scaling laws will be discussed in the next section.

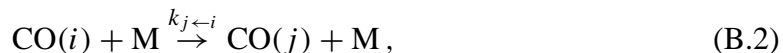
While line mixing and line broadening both relate to RET rates, they are used differently for the purposes of inferring RET rates for analysis of the pulsed excitation process associated with IR PLIF. Line mixing is dependent on specific transition rates, and is therefore the most rigorous available spectroscopic benchmark against which to compare RET scaling laws and the attendant parameters. Because of this, extensive work has been presented in the literature using line mixing to establish the relative usefulness of line broadening in conjunction with the established scaling laws. However, once the applicability of scaling laws have been determined, using scaling laws to infer RET rates is the most straightforward approach, due to the availability of line broadening values for a variety of colliding species.

B.5 RET Scaling Models

Since experimental data are not typically constrained by individual rotational transition rates and computational efforts to describe each rotational transition independently are unwieldy, scaling laws are used to reduce the number of calculated or measured parameters. Two important RET scaling models are discussed here, namely the modified exponential-gap (MEG) and energy-corrected sudden (ECS). This discussion will motivate the use of the MEG scaling for IR PLIF analysis, but also note the limitations of MEG and the potential need for ECS scaling in future efforts.

B.5.1 Modified Exponential-Gap

The modified exponential-gap law is a phenomenological exponential-gap law with energy correction terms applied to the initial and final levels. In the form implemented here, it gives a general form for collisionally-induced endothermic rotational state changes:



through the use of the equation:

$$k_{j \leftarrow i} = A \left(\frac{296}{T} \right)^n \left(\frac{1 + E_i/k_B T \delta}{1 + E_j/k_B T} \right)^2 \exp(-\beta \Delta E/k_B T). \quad (\text{B.3})$$

Here $k_{j \leftarrow i}$ is the transition rate from rotational state i to j ; E_i is the energy of state i [J]; T is temperature [K]; $\Delta E \equiv E_j - E_i$, k_B is Boltzmann's constant [J/K]; and A [s^{-1}], β , δ , and n are fitting parameters. Exothermic reaction rates follow from detailed balance.

The MEG model does not distinguish between dipolar (Δj odd) and quadrupolar (Δj even) selection rules, so any means for distinguishing between the two must be added in an *ad hoc* fashion. This is a major limitation of the MEG model; in particular, CO_2 RET rates in Π and Γ vibrational levels clearly show propensity differences for dipolar and quadrupolar transitions [52–54, 70, 75–85].

B.5.2 Energy-Corrected Sudden

ECS is not used here since for the vibrational levels considered MEG is suitable and computationally more efficient; however, for IR PLIF techniques which involve transitions between levels with odd axial spin moments an ECS formalism would be more appropriate. Since the ECS model is not used here, it will be summarized only briefly. The energy-corrected sudden (ECS) model [86, 87] expresses the relaxation matrix W in terms of “base rates” by accounting for transition-dependent angular momentum coupling. The base rates are thermally-averaged inelastic cross sections for downwards transitions to the ground state, and are modeled quasi-classically or matched to experimental data using exponential power law scaling.

Since the ECS formalism accounts properly for angular momentum coupling, it can correctly model, using one set of base rates, RET in vibrational levels with different axial spin momenta each of which have different probabilities for odd- and even-parity transitions. The ECS model is more complicated to implement since the generality of its functional form leads to sums over $6-j$ symbols which are time-consuming to calculate, but would be necessary if Π or Γ states of CO_2 were used for excitation.

B.6 Integration Technique and Scaling Law Parameters

MEG scaling was used for all calculations since it is efficient to implement and is quite suitable for modeling RET in Σ vibrational levels. For CO and CO_2 , MEG has been shown to be successful in predicting Raman Q branch collapse [39, 40, 53].

For CO_2 , MEG is in general limited by its inability to predict propensity differences between odd- and even- Δ_j collisions or changes in RET rates with the axial spin momentum of the vibrational level; however, all CO_2 excitation schemes discussed in this report involve levels with zero axial spin momentum (species Σ^+ ; axial spin momentum quantum number $l=0$). For these levels (in $^{12}\text{C}^{16}\text{O}_2$), half of the rotational states ($j=\text{odd}$ or $j=\text{even}$) have zero populations due to the nuclear symmetry and the Pauli exclusion principle. Because of this, MEG is also suitable for CO_2 for IR PLIF calculations.

Gas	Collisional Partner	A [s^{-1}]	β	δ	n
CO	CO	4.2×10^8	1.35	1.17	0.69
CO ₂	CO ₂	5.3×10^8	1.42	1.30	0.63
CO ₂	N ₂	3.6×10^8	1.22	1.32	0.64
CO ₂	Ar	3.0×10^8	1.22	1.41	0.65

Table B.1: MEG parameters for several gas mixtures.

For each RET calculation, MEG parameters were calculated so as to match the collisional linewidths for the given temperature and bath gas mixture. Fitting collisional linewidths in and of itself is not enough to guarantee the accuracy of the individual state-to-state rates [39]; however, the ability of the MEG scaling law to accurately predict line mixing in CO and in Σ^+ levels of CO₂ indicates that rates generated by a MEG scaling law that matches collisional linewidths are suitable for predicting phenomena that depend on state-to-state transfer processes, such as line mixing and the dependence of IR PLIF signal on laser fluence. Previous work has confirmed the accuracy of the linewidth-fitting technique [52–54, 70, 75, 79, 88–93], as well as the validity of using one set of RET rates for all vibrational levels [94, 95]. MEG parameters are summarized in Table B.1. Since the number of rate equations is modest, rate equations for RET are integrated using MATLAB. As needed for CO₂, fast VET processes are included.

Appendix C

Vibrational Energy Transfer

C.1 Introduction

As discussed in Chapters 2–4, the magnitude of fluorescence generated by an IR PLIF technique may be quantified only through integration of the excited vibrational level populations over the detector integration time. Performing this integration requires understanding of the vibrational levels of these species, the level energies, and rates of transfer between the levels. Along with this, a numerical integration scheme must be carefully chosen, since the number of vibrational levels and energy transfer mechanisms are quite numerous and the computations can quickly become unwieldy. To address these issues, this appendix describes the vibrational manifolds of the molecules in question, vibrational energy transfer processes, the rate equation model and integration technique used to model fluorescence yield or fluorescence quantum yield, and the rates used to perform the calculations.

C.2 Vibrational Manifolds and Notation

Vibrational energy levels for diatomics (N_2 , O_2 , and CO) are straightforward since they each have only one vibrational mode, and the vibrational energy levels can be numbered with one quantum number, v . In the harmonic oscillator approximation, the energy of level v is given by $e_v = vk_{\text{B}}\Theta$, where k_{B} is the Boltzmann constant and Θ is the characteristic temperature of the vibration [36]. Since the energy spacing between levels is uniform, it

is natural to refer to the quantum number as an indicator of the number of units or quanta of vibrational energy above the absolute zero (half-point) energy. Molecules in a specific vibrational level are denoted here with the vibrational level in parentheses; for example, an N_2 molecule with one quantum of vibrational energy is listed as $\text{N}_2(1)$.

The vibrations of triatomics have three vibrational frequencies (ν_1 through ν_3), which correspond (for H_2O and CO_2) to the symmetric stretching vibration (ν_1), the bending vibration (ν_2), and the asymmetric stretching vibration (ν_3). For simplicity, the vibrations are in this dissertation considered to be independent and harmonic, in which case the vibrations may be decomposed into orthogonal modes whose wavefunctions may be multiplied to generate the total vibrational wavefunction [51]. In this case, one quantum number per degree of freedom is enough to describe the wavefunction and energy of a vibrational level.

H_2O is nonlinear, and therefore all of its vibrational modes are nondegenerate. The vibrational quantum state of an H_2O molecule can be described with three quantum numbers (ν_1 , ν_2 , and ν_3), which indicate the number of vibrational energy quanta at the ν_1 , ν_2 , and ν_3 frequencies, respectively. For example, an H_2O molecule with one quantum of symmetric stretch (ν_1) energy and one unit of bend (ν_2) energy is listed as $\text{H}_2\text{O}(110)$. The harmonic oscillator wavefunction solutions (*i.e.*, solutions of the Schrödinger equation with a harmonic potential) are good approximations of the real eigenfunctions of this system.

CO_2 is linear; therefore the ν_2 bending mode is doubly degenerate, and four quantum numbers are required to describe the vibrational quantum state. One set of quantum numbers that could be used is ν_1 , ν_{2a} , ν_{2b} , ν_3 , in which ν_{2a} and ν_{2b} correspond to units of bend energy along two orthogonal axes. However, the most useful descriptors of the ν_2 bending energy (*i.e.*, the eigenvalues of the system) are the magnitude of the bending energy and its axial spin momentum. Therefore, following Ref. [47], the four quantum numbers ν_1 , ν_2 , ν_3 , and l are used for the vibrations of a linear triatomic molecule, where ν_2 is proportional to the total bending energy and l is proportional to the axial spin momentum.

CO_2 is furthermore complicated by the accidental (Fermi) resonance of ν_1 and $2\nu_2$. Because of this Fermi resonance, the harmonic oscillator wavefunctions are no longer good approximations of the system eigenfunctions, and the use of ν_1 and ν_2 quantum numbers to describe the energy levels is no longer particularly meaningful [96]. Accordingly, CO_2

vibrational levels are labeled following Ref. [47]: v_2 is by convention set equal to l , and the Fermi-resonant states are ranked (using an index r) in order of decreasing energy. r ranges from 1 to v_1+1 , and is typically omitted when $v_1=0$. CO_2 levels are then listed in the form $\text{CO}_2(v_1, v_2^l, v_3)_r$. Note that, using this notation, the four independent quantum numbers are now v_1, l, v_3 , and r .

While the similarity (or lack) between vibrational eigenfunctions and harmonic oscillator wavefunctions is important for spectroscopy and notation, it is not particularly important for evaluating energy transfer. Because of this, while the more quantum-mechanically rigorous notation is used here to describe vibrational levels, the energy transfer rates in CO_2 are treated as independent of the axial spin momentum of the vibrational levels. For example, the rates into and out of the $10^0 0_{\text{I}}$ and $02^2 0$ levels are assumed to be the same. This is consistent with the results of Refs. [50, 70, 97] for exchange between the $10^0 0_{\text{I}}$, $10^0 0_{\text{II}}$, and $02^2 0$ levels of CO_2 , and greatly reduces the number of individual reactions and vibrational levels which must be incorporated when the vibrational transfer is modeled numerically.

C.3 VET processes

For the purposes of this discussion, collisional VET processes are separated into four categories: V-T equilibration, intermodal V-V equilibration, intramodal V-V equilibration, and intermolecular V-V equilibration. It should be noted that, while energy transfer is described as resulting from “collisions”, this term is used in this context to imply any intermolecular interaction that results in energy transfer and whose rate scales with pressure and translational temperature like a hard-sphere collision rate. Also, since calculations of the fluorescence quantum yield require analysis of the vibrational cooling of a vibrationally hot system, the processes will typically be discussed in the translationally exothermic direction. Of course, the reverse processes occur at rates consistent with detailed balance. The following sections describe the four VET processes in detail.

C.3.1 V-T equilibration

V-T (vibration-to-translation) equilibration processes allow vibrational modes to equilibrate their temperature with the translational modes. V-T processes occur when two molecules collide, causing one of the molecules to lose a vibrational energy quantum while the other molecule's vibrational level remains unchanged. An example of this is the V-T equilibration of CO: $\text{CO}(1) + \text{M} \leftrightarrow \text{CO}(0) + \text{M}$. In this appendix, as is convention [46], M indicates any species. The lost vibrational energy from these processes takes the form of increased velocities, which are very quickly equilibrated and result in a higher translational temperature.

C.3.2 Intermodal V-V equilibration

Intermodal V-V (vibration-to-vibration) equilibration processes allow different vibrational modes within a specific molecule to equilibrate with each other. In this case, a collision perturbs the motion of the nuclei of a molecule such that, after the collision, the vibrational energy is stored in different vibrational modes. Again, the collisional partner does not experience a vibrational quantum number change. For example, the ν_1 and ν_2 modes in CO_2 exchange energy via $\text{CO}_2 10^0 0_1 + \text{M} \leftrightarrow \text{CO}_2 02^2 0 + \text{M}$ and similar processes. The ν_3 mode equilibrates with the other modes via non-resonant processes such as $\text{CO}_2 00^0 1 + \text{M} \leftrightarrow \text{CO}_2 11^0 0_1 + \text{M}$.

C.3.3 Intramodal V-V equilibration

Intramodal V-V equilibration processes allow an individual vibrational mode to achieve a Boltzmann distribution. In this case, two molecules of the same species collide and exchange a vibrational quantum, with the total number of vibrational quanta in that mode unchanged. Because the vibrations are nearly harmonic, these transfer processes are always near-resonant and tend to be rapid. An example of intramodal V-V equilibration is $\text{CO}(2) + \text{CO}(0) \leftrightarrow \text{CO}(1) + \text{CO}(1)$.

C.3.4 Intermolecular V-V equilibration

Intermolecular V-V equilibration processes allow vibrational energy to be exchanged directly between species without coupling to the translational modes. In this case, two molecules of different species collide. If the vibrational energy quanta of the two molecules are of similar energy, one molecule may lose a vibrational quantum and the other molecule may gain a vibrational quantum, with only a small net vibrational energy change which must be taken up by the translational mode. An example of intermolecular V-V equilibration is $\text{N}_2(1) + \text{CO}(0) \leftrightarrow \text{N}_2(0) + \text{CO}(1)$.

C.4 VET model, Integration Technique

The vibrational level distribution induced by laser excitation is evaluated as a function of time using a rate equation formulation and the CHEMKIN interface [46]. Codes for implementation are recorded in Ref. [98]. The model assumes translational and rotational equilibrium, since these modes equilibrate very quickly as compared to the camera integration time. Vibrational energy transfer occurs based on collisional processes and, in some cases, laser excitation. The elements of this model are described in the following sections.

C.4.1 Thermodynamic Database

Since the thermodynamic database that is used as an input to CHEMKIN is designed to assume vibrational equilibrium, the database has been modified to treat vibrational levels as individual species. The thermodynamic entry for a species (*e.g.*, CO) has been replaced by a set of entries, one for each level (CO(0), CO(1), CO(2), etc.). This process is performed by the FORTRAN77 code MKTHERM.F [98]. Since vibrational levels are treated as individual species, the specific heat of each level contains contributions only from translational and rotational energy modes. Thus the polynomial fit [46] for the specific heat c_p is replaced with a constant value ($2.5k_B T$ for monatomic species, $3.5k_B T$ for linear di- or triatomic species, $4k_B T$ for nonlinear triatomic species). The energies of each level are modified to account for the differences in vibrational energy; this is necessary to properly account for translational temperature changes associated with V-T processes and to

enable CHEMKIN to properly calculate reverse rates for VET processes. These energies are chosen to correctly account for VET but are not correct if chemical reactions occur. Harmonic oscillators are assumed for simplicity, since preliminary calculations including anharmonicities had insignificant effect on vibrational energy transfer results.

C.4.2 Initial Condition

An initial condition is set that corresponds primarily to an equilibrium vibrational distribution. If a nanosecond laser excitation pulse is being modeled, this perturbation is assumed instantaneous with time and the laser-induced perturbation on the lower and upper vibrational levels of the laser transition is treated as part of the initial condition. Ar, CO, CO₂, N₂, O₂, H₂, He, and H₂O may be specified as bath gases. In total, roughly 80 vibrational levels and 14,000 energy transfer processes are used. This operation is performed by the FORTRAN77 code MKINP.F [98].

C.4.3 Energy Transfer Rates and CHEMKIN

To enable implementation using the CHEMKIN interface and solver, and vibrational energy transfer rates are given by curves fit to experimental or computational transfer rate data from a variety of references. Rates of stimulated absorption and stimulated emission are also fit to curves. The CHEMKIN interface provides reverse reaction rates for collisional processes so as to satisfy detailed balance.

Since thousands of energy transfer processes are needed to accurately describe the energy transfer resulting from the numerous collision combinations, the curve-fitting process is applied only to transfer processes involving low-lying levels, and SSH theory [30] is used to scale the curve-fit rates for processes involving higher levels. Using this approach, curve fitting need only occur for a relatively small set of energy transfer processes (~ 25), but rates are generated for thousands of combinations of colliding molecules. The FORTRAN77 code MKTHERM.F [98] also performs the SSH scaling and generates a .MEC mechanism file which is used by the CHEMKIN interface. The CHEMKIN interpreter and solver [46] has also been modified to account for the large number of species and reactions [98].

In general, when there are multiple processes which cause energy transfer of a certain nature, mechanisms that are always negligibly slow are omitted. For example, since multi-quantum transitions tend to be slow in the low-lying vibrational levels of diatomics [99], they may be ignored and it may be safely assumed that changes of multiple quanta occur as a multi-step process. For example, the process $\text{CO}(5) + \text{CO}(0) \leftrightarrow \text{CO}(3) + \text{CO}(2)$ would not be treated as occurring in one collision, but rather as a two step process: $\text{CO}(5) + \text{CO}(0) \leftrightarrow \text{CO}(4) + \text{CO}(1)$, followed by $\text{CO}(4) + \text{CO}(1) \leftrightarrow \text{CO}(3) + \text{CO}(2)$.

C.4.4 Vibrational Energy Base Transfer Rates

This section lists the sources and curve fit parameters for the base energy transfer processes.

V-T and intermodal V-V Energy Transfer Rates

These rates are for collisional processes where the vibrational energy of one molecule changes, but the vibrational energy of the other molecule does not.

V-T equilibration of N_2 Rates calculated in Ref. [100] (using $M = \text{N}_2$) are used for the $\text{N}_2(v) + M \leftrightarrow \text{N}_2(v - 1) + M$ process. These rates are consistent with the experiments in Ref. [101].

V-T equilibration of CO Rates calculated in Ref. [102] (using $M = \text{CO}$) are used for the $\text{CO}(v) + M \leftrightarrow \text{CO}(v - 1) + M$ process. These rates are consistent with the experiments in Refs. [101, 103].

V-T equilibration of O_2 Rates calculated in Ref. [104] (using $M = \text{O}_2$) are used for the $\text{O}_2(v) + M \leftrightarrow \text{O}_2(v - 1) + M$ process. These rates are consistent with the experiments in Ref. [101].

V-T equilibration of the asymmetric stretch mode of CO_2 Rates calculated in Ref. [50] (using $M = \text{N}_2$) are used for the $\text{CO}_2(v_1, v_2^l, v_3)_r + M \leftrightarrow \text{CO}_2(v_1, v_2^l, v_3 - 1)_r + M$ process.

V-T equilibration of the symmetric stretch mode of CO₂ The $\text{CO}_2(v_1, v_2^l, v_3)_r + \text{M} \leftrightarrow \text{CO}_2(v_1 - 1, v_2^l, v_3)_r + \text{M}$ process for direct V-T equilibration of the symmetric stretch is ignored, with the assumption that the close coupling between v_1 and v_2 modes combined with the fast V-T equilibration of the v_2 mode makes indirect V-T equilibration through the v_2 mode (*e.g.*, $10^00_1 \rightarrow 02^20 \rightarrow 01^10 \rightarrow 00^00$) much faster than direct equilibration ($10^00_1 \rightarrow 00^00$) [50].

V-T equilibration of the bend mode of CO₂ Experimental rates from Refs. [105–107] for the $\text{CO}_2(v_1, v_2^l, v_3)_r + \text{M} \leftrightarrow \text{CO}_2(v_1, v_2 - 1^{l-1}, v_3)_r + \text{M}$ process match well with Ref. [50] and the results from [105] are used. Rates are similar for collisions with O₂, N₂, and CO [106], but the Ar V-T rate is approximately 8 times slower [105] and the H₂O V-T rate is modeled as being 90 times faster. The water enhancement is estimated based on the water enhancement of the equilibration of the bend mode of H₂O [49].

Near-resonant exchange between Fermi-resonant and other near-resonant levels of CO₂ The temperature dependence of the rates calculated in Ref. [50] (using $\text{M} = \text{N}_2$) for the $\text{CO}_2(v_1, v_2^l, v_3)_r + \text{M} \leftrightarrow \text{CO}_2(v_1, v_2^l, v_3)_{r+1} + \text{M}$ process is used, but the magnitude of the rates in Ref. [50] is divided by two so as to better match the experimental values of Refs. [70, 97].

Intermodal deexcitation of the asymmetric stretch mode of CO₂ Rates calculated in Ref. [50] (using $\text{M} = \text{N}_2$) are used for a number of $\Delta v_3 = -1$ processes, the fastest of which is $\text{CO}_2(v_1, v_2^l, v_3)_r + \text{M} \leftrightarrow \text{CO}_2(v_1 + 1, v_2^{l+1} + 1, v_3 - 1)_r + \text{M}$. Rates for collisions with Ar are ten times slower [55] and collisions with H₂O are modeled as 90 times faster. The water enhancement is estimated based on the water enhancement of the equilibration of the bend mode of H₂O [49].

V-T equilibration of the asymmetric stretch mode of H₂O The $\text{H}_2\text{O}(v_1, v_2, v_3) + \text{M} \leftrightarrow \text{H}_2\text{O}(v_1, v_2, v_3 - 1) + \text{M}$ process is modeled as having the same rate as the equivalent process for CO₂.

V-T equilibration of the symmetric stretch mode of H₂O The $\text{H}_2\text{O}(v_1, v_2, v_3) + \text{M} \leftrightarrow \text{H}_2\text{O}(v_1 - 1, v_2, v_3) + \text{M}$ process is modeled as having the same rate as the $\Delta v_3 = -1$ process for CO₂.

V-T equilibration of the bend mode of H₂O Experimental rates from Refs. [49] for the $\text{H}_2\text{O}(v_1, v_2, v_3) + \text{M} \leftrightarrow \text{H}_2\text{O}(v_1, v_2 - 1, v_3) + \text{M}$ process (using $\text{M} = \text{Ar}$) are used. Rates for collisions with N₂ and H₂O are enhanced by factors of 1.4 and 125, respectively [49].

Intermodal V-V equilibration between symmetric and asymmetric stretch modes of H₂O Due to the near-resonance of the v_1 and v_3 states of H₂O, the $\text{H}_2\text{O}(v_1, v_2, v_3) + \text{M} \leftrightarrow \text{H}_2\text{O}(v_1 + 1, v_2, v_3 - 1) + \text{M}$ process is modeled as having the same rate as the exchange of energy between Fermi-resonant states in CO₂.

Intermodal V-V equilibration between stretch and bend modes of H₂O Data in the literature is sparse for the V-V processes which equilibrate the stretch modes of H₂O with the bend mode; however, Ref. [49] indicates that these processes are on the same order as V-T relaxation of the bend mode. Thus the rates of the $\text{H}_2\text{O}(v_1, v_2, v_3) + \text{M} \leftrightarrow \text{H}_2\text{O}(v_1 - 1, v_2 + 2, v_3) + \text{M}$ and $\text{H}_2\text{O}(v_1, v_2, v_3) + \text{M} \leftrightarrow \text{H}_2\text{O}(v_1, v_2 + 2, v_3 - 1) + \text{M}$ processes are assumed equal to the rate of V-T relaxation of the bend mode.

V-V Energy Transfer Rates

These rates are for processes in which both colliding molecules undergo a change in vibrational level, typically because of a near-resonance between energy gaps. In this section, v is used as before to denote vibrational quantum numbers, l is used to denote axial spin momentum, and r is a ranking index for Fermi-resonant levels; for clarity, the level of the second molecule will be described using w , ℓ , and q to denote vibrational quantum number, axial spin momentum, and ranking index respectively.

Intramodal Relaxation of CO Rates calculated in Ref. [102] are used for the $\text{CO}(v) + \text{CO}(w) \leftrightarrow \text{CO}(v - 1) + \text{CO}(w + 1)$ process. These rates are consistent with the experiments in Refs. [108, 109].

Intramodal Relaxation of N₂ Rates calculated in Ref. [100] are used for the $N_2(v) + N_2(w) \leftrightarrow N_2(v-1) + N_2(w+1)$ process.

Intramodal Relaxation of O₂ Rates calculated in Ref. [104] are used for the $O_2(v) + O_2(w) \leftrightarrow O_2(v-1) + O_2(w+1)$ process.

Intramodal Relaxation of the asymmetric stretching mode of CO₂ Rates measured in Refs. [34, 35, 110] are used for the $CO_2(v_1, v_2^l, v_3)_r + CO_2(w_1, w_2^l, w_3)_q \leftrightarrow CO_2(v_1, v_2^l, v_3+1)_r + CO_2(w_1, w_2^l, w_3-1)_q$ process.

Intramodal Relaxation of the symmetric stretching mode of CO₂ Rates for the $CO_2(v_1, v_2^l, v_3)_r + CO_2(w_1, w_2^l, w_3)_q \leftrightarrow CO_2(v_1+1, v_2^l, v_3)_r + CO_2(w_1-1, w_2^l, w_3)_q$ process are assumed equal to the intramodal relaxation rates for the asymmetric stretch [110].

Intramodal Relaxation of the bending mode of CO₂ Rates for the $CO_2(v_1, v_2^l, v_3)_r + CO_2(w_1, w_2^l, w_3)_q \leftrightarrow CO_2(v_1, v_2+1^{l+1}, v_3)_r + CO_2(w_1, w_2-1^{l-1}, w_3)_q$ process are assumed equal to the intramodal relaxation rates for the asymmetric stretch [110].

Intramodal Relaxation of the modes of H₂O Because the V-T rates for H₂O are so large, intramodal relaxation may be safely ignored.

CO-N₂ V-V transfer Rates calculated in Ref. [111] are used for the $CO(v) + N_2(w) \leftrightarrow CO(v-1) + N_2(w+1)$ process. These rates are consistent with the experiments in Refs. [112, 113].

CO-O₂ V-V transfer The $CO(v) + O_2(w) \leftrightarrow CO(v-1) + O_2(w+1)$ process for CO-O₂ V-V transfer may safely be ignored due to its low rate [114].

CO-H₂ V-V transfer The $CO(v) + H_2(w) \leftrightarrow CO(v-1) + H_2(w+1)$ process for CO-H₂ V-V transfer may safely be ignored due to its low rate [101, 115–117].

N₂-CO₂ V-V transfer Rates calculated in Ref. [50] are used for the $\text{CO}_2(v_1, v_2^l, v_3)_r + \text{N}_2(w) \leftrightarrow \text{CO}_2(v_1, v_2^l, v_3 + 1)_r + \text{N}_2(w - 1)$ process.

CO-CO₂ V-V transfer Experimental rates from Refs. [33, 109, 118, 119] are used for the $\text{CO}_2(v_1, v_2^l, v_3)_r + \text{CO}(w) \leftrightarrow \text{CO}_2(v_1, v_2^l, v_3 + 1)_r + \text{CO}(w - 1)$ process.

CO-H₂O V-V transfer Experimental rates from Refs. [112, 120] are used for the $\text{H}_2\text{O}(v_1, v_2, v_3) + \text{CO}(w) \leftrightarrow \text{H}_2\text{O}((v_1, v_2 + 1, v_3)) + \text{CO}(w - 1)$ process.

C.4.5 Vibrational Energy Transfer Rates—Curve Fits

The rate k [cm^3/s] of all vibrational energy transfer processes were fit to the following form:

$$k = AT_{\text{tr}}^B \exp(-C/T_{\text{tr}}), \quad (\text{C.1})$$

where A [cm^3/s], B [unitless], and C [K] are fitting parameters. In all cases the translational temperature T_{tr} dictates the VET rates. The curve fit values for base V-T reactions are summarized in Table C.1, and the curve fit values for base V-V reactions are summarized in Table C.2.

C.4.6 Integration and Fluorescence Yield Calculation

The CHEMKIN interface creates output files for each vibrational level, which are then post-processed into a single file by the FORTRAN77 code COMBINE.F [98]. Once the excited state populations have been collected, fluorescence quantum yield or fluorescence yield (depending on the nature of the laser-induced excitation) can be straightforwardly calculated as a function of temperature by the FORTRAN77 code CONSOLIDATE.F [98] according to Equation 2.4 or Equation 3.2.

V-T Process	A [cm ³ /s]	B	C [K]
N ₂ (1) + M ↔ N ₂ (0) + M	2.8e-44	8.72	588
O ₂ (1) + M ↔ O ₂ (0) + M	1.4e-32	5.31	-331
CO(1) + M ↔ CO(0) + M	1.3e-22	2.57	-1389
CO ₂ 00 ⁰ 1 + M ↔ CO ₂ 00 ⁰ 0 + M	2.5e-20	1.25	75
CO ₂ 01 ¹ 0 + M ↔ CO ₂ 00 ⁰ 0 + M	8.6e-25	3.77	144
CO ₂ 10 ⁰ 0 _I + M ↔ CO ₂ 02 ² 0 + M	9.4e-14	0.57	-138
CO ₂ 00 ⁰ 1 + M ↔ CO ₂ 11 ⁰ 0 _I + M	2.5e-19	1.43	-473
CO ₂ 00 ⁰ 1 + M ↔ CO ₂ 10 ⁰ 0 _I + M	4.3e-20	1.48	240
CO ₂ 00 ⁰ 1 + M ↔ CO ₂ 01 ¹ 0 + M	6.0e-19	0.68	131
H ₂ O(001) + M ↔ H ₂ O(000) + M	2.5e-20	1.25	75
H ₂ O(100) + M ↔ H ₂ O(000) + M	2.5e-20	1.25	75
H ₂ O(010) + M ↔ H ₂ O(000) + M	4.0e-13	0.00	0
H ₂ O(100) + M ↔ H ₂ O(001) + M	9.4e-14	0.57	-138
H ₂ O(001) + M ↔ H ₂ O(020) + M	4.0e-13	0.00	0
H ₂ O(100) + M ↔ H ₂ O(020) + M	4.0e-13	0.00	0

Table C.1: Base rates for various V-T energy transfer processes.

V-V Process	A [cm ³ /s]	B	C [K]
CO(1) + CO(0) ↔ CO(0) + CO(1)	1.2e-11	-0.38	-142
N ₂ (1) + N ₂ (0) ↔ N ₂ (0) + N ₂ (1)	5.0e-18	1.35	-58
O ₂ (1) + O ₂ (0) ↔ O ₂ (0) + O ₂ (1)	2.9e-17	1.12	37
CO ₂ 00 ⁰ 1 + CO ₂ 00 ⁰ 0 ↔ CO ₂ 00 ⁰ 0 + CO ₂ 00 ⁰ 1	1.2e-10	0.00	0
CO ₂ 10 ⁰ 0 + CO ₂ 00 ⁰ 0 ↔ CO ₂ 00 ⁰ 0 + CO ₂ 10 ⁰ 0	1.2e-10	0.00	0
CO ₂ 01 ¹ 0 + CO ₂ 00 ⁰ 0 ↔ CO ₂ 00 ⁰ 0 + CO ₂ 01 ¹ 0	5.7e-11	0.00	0
N ₂ (1) + CO(0) ↔ N ₂ (0) + CO(1)	7.5e-18	1.35	-5
CO ₂ 00 ⁰ 1 + N ₂ (0) ↔ CO ₂ 00 ⁰ 0 + N ₂ (1)	9.9e-12	-0.41	-46
CO ₂ 00 ⁰ 1 + CO(0) ↔ CO ₂ 00 ⁰ 0 + CO(1)	3.0e-18	1.84	173
CO(1) + H ₂ O(000) ↔ CO(0) + H ₂ O(010)	5.7e-16	1.00	0

Table C.2: Base rates for various V-V energy transfer processes.

References

- [1] J.M. Seitzman and R.K. Hanson. Planar fluorescence imaging in gases. In A. Taylor, editor, *Experimental Methods for Flows with Combustion*. Academic Press, London, 1993.
- [2] W. P. Partridge, J. R. Reisel, and N. M. Laurendeau. Laser-saturated fluorescence measurements of nitric-oxide in an inverse diffusion flame. *Combustion and Flame*, 116(1-2):282–290, 1999.
- [3] M. Alden, P. Grafstrom, H. Lundberg, and S. Svanberg. Spatially resolved temperature measurements in a flame using laser-excited two-line atomic fluorescence and diode array detection. *Optics Letters*, 8(5):241–243, 1983.
- [4] B. Hiller and R. K. Hanson. Simultaneous planar measurements of velocity and pressure fields in gas flows using laser-induced fluorescence. *Applied Optics*, 27(1):33–48, 1988.
- [5] J. Rehm and P.H. Paul. Reaction rate imaging. *Proceedings of the Combustion Institute*, 28, 2000, in press.
- [6] K. Kohse-Hoinghaus. Laser techniques for the quantitative detection of reactive intermediates in combustion systems. *Progress in Energy and Combustion Science*, 20(3):203–279, 1994.
- [7] M. Alden. Laser spectroscopic techniques for combustion diagnostics. *Combustion Science and Technology*, 149(1-6), 1999.

- [8] A. Lozano, S. H. Smith, M. G. Mungal, and R. K. Hanson. Concentration measurements in a transverse jet by planar laser-induced fluorescence of acetone. *AIAA Journal*, 32(1):218–221, 1994.
- [9] B. K. McMillin, J. L. Palmer, and R. K. Hanson. Temporally resolved, two-line fluorescence imaging of NO temperature in a transverse jet in a supersonic crossflow. *Applied Optics*, 32(36):7532–7545, 1993.
- [10] J. L. Palmer and R. K. Hanson. Shock tunnel flow visualization using planar laser-induced fluorescence imaging of NO and OH. *Shock Waves*, 4(6):313–323, 1995.
- [11] N. T. Clemens and P. H. Paul. Effects of heat release on the near-field flow structure of hydrogen jet diffusion flames. *Combustion and Flame*, 102(3):271–284, 1995.
- [12] M. G. Allen, R. D. Howe, and R. K. Hanson. Digital imaging of reaction zones in hydrocarbon air flames using planar laser-induced fluorescence of CH and C₂. *Optics Letters*, 11(3):126–128, 1986.
- [13] H. N. Najm, P. H. Paul, C. J. Mueller, and P. S. Wyckoff. On the adequacy of certain experimental observables as measurements of flame burning rate. *Combustion and Flame*, 113(3):312–332, 1998.
- [14] C. Schulz, B. Yip, V. Sick, and J. Wolfrum. A laser-induced fluorescence scheme for imaging nitric oxide in engines. *Chemical Physics Letters*, 242(3):259–264, 1995.
- [15] G. Kychakoff, R. D. Howe, R. K. Hanson, and J. C. McDaniel. Quantitative visualization of combustion species in a plane. *Applied Optics*, 21(18):3225–3227, 1982.
- [16] G. Kychakoff, K. Knapp, R. D. Howe, and R. K. Hanson. Flow visualization in combustion gases using nitric oxide fluorescence. *Aiaa Journal*, 22(1):153–154, 1984.
- [17] M. P. Lee, P. H. Paul, and R. K. Hanson. Laser fluorescence imaging of O₂ in combustion flows using an ArF laser. *Optics Letters*, 11(1):7–9, 1986.

- [18] M.B. Long, D.C. Fourquette, and M.C. Escoda. Instantaneous Ramanography of a turbulent diffusion flame. *Optics Letters*, 8(5):244–246, 1983.
- [19] D. F. Marran, J. H. Frank, M. B. Long, S. H. Starner, and R. W. Bilger. Intracavity technique for improved Raman/Rayleigh imaging in flames. *Optics Letters*, 20(7):791–793, 1995.
- [20] J. M. Seitzman, J. Haumann, and R. K. Hanson. Quantitative two-photon LIF imaging of carbon monoxide in combustion gases. *Applied Optics*, 26(14):2892–2899, 1987.
- [21] K. Nyholm, R. Fritzon, and M. Alden. Two-dimensional imaging of OH in flames by use of polarization spectroscopy. *Optics Letters*, 18(19):1672–1674, 1993.
- [22] B. A. Mann, S. V. O'Leary, A. G. Astill, and D. A. Greenhalgh. Degenerate four-wave mixing in nitrogen-dioxide: Application to combustion diagnostics. *Applied Physics B-Photophysics and Laser Chemistry*, 54(4):271–277, 1992.
- [23] R.H. Barlow, J.H. Frank, and G.J. Fiechtner. Comparison of CO measurements by Raman scattering and two-photon LIF in laminar and turbulent methane flames. *Spring Meeting of the Western States Section of the Combustion Institute*, Paper No. WSS/CI 98S-19, 1998.
- [24] J. Haumann, J. M. Seitzman, and R. K. Hanson. 2-photon digital imaging of CO in combustion flows using planar laser-induced fluorescence. *Optics Letters*, 11(12):776–778, 1986.
- [25] B.J. Kirby and R.K. Hanson. Planar laser-induced fluorescence imaging of carbon monoxide using vibrational (infrared) transitions. *Applied Physics B*, 69(5/6):505–507, 1999.
- [26] B.J. Kirby and R.K. Hanson. Imaging of CO and CO₂ using infrared planar laser-induced fluorescence. *Proceedings of the Combustion Institute*, 2000, in press.
- [27] N. Georgiev and M. Aldén. Two-dimensional imaging of flame species using two-photon laser-induced fluorescence. *Applied Spectroscopy*, 51(8):1229–1237, 1997.

- [28] G. Juhlin, H. Neij, M. Versluis, B. Johansson, and M. Alden. Planar laser-induced fluorescence of H₂O to study the influence of residual gases on cycle-to-cycle variations in SI engines. *Combustion Science and Technology*, 132(1-6):75–97, 1998.
- [29] L. S. Rothman, C. P. Rinsland, A. Goldman, S. T. Massie, D. P. Edwards, J. M. Flaud, A. Perrin, C. Camy-Peyret, V. Dana, J. Y. Mandin, J. Schroeder, A. McCann, R. R. Gamache, R. B. Wattson, K. Yoshino, K. V. Chance, K. W. Jucks, L. R. Brown, V. Nemtchinov, and P. Varanasi. The HITRAN molecular spectroscopic database and HAWKS(HITRAN atmospheric workstation): 1996 edition. *Journal of Quantitative Spectroscopy & Radiative Transfer*, 60(5):665–710, 1998.
- [30] J.T. Yardley. *Introduction to Molecular Energy Transfer*. Academic Press, New York, 1980.
- [31] P. H. Paul, M. P. Lee, and R. K. Hanson. Molecular velocity imaging of supersonic flows using pulsed planar laser-induced fluorescence of NO. *Optics Letters*, 14(9):417–419, 1989.
- [32] B.J. Kirby and R.K. Hanson. Linear excitation schemes for IR PLIF imaging of CO and CO₂. submitted to *Applied Optics*, 2001.
- [33] D. F. Starr and J. K. Hancock. Vibrational energy transfer in CO₂-CO mixtures from 163 to 406 °K. *Journal of Chemical Physics*, 63(11):4730–4734, 1975.
- [34] Jack Finzi and C. Bradley Moore. Relaxation of CO₂(10⁰1), CO₂(02⁰1), and N₂O(10⁰1) vibrational levels by near-resonant $V \rightarrow V$ energy transfer. *Journal of Chemical Physics*, 63(6):2285–2288, 1975.
- [35] L. Doyennette, M. Margottin-Maclou, A. Chakroun, H. Gueguen, and L. Henry. Vibrational energy transfer from (00⁰1) level of ¹⁴N₂O and ¹²CO₂ to ($m,n^l,1$) levels of these molecules and of their isotopic species. *Journal of Chemical Physics*, 62(2):440–447, 1975.
- [36] W.G. Vincenti and C.H. Kruger, Jr. *Introduction to Physical Gas Dynamics*. Krieger Publishing Company, Malabar, 1965.

- [37] A.C. Eckbreth. *Laser Diagnostics for Combustion Temperature and Species*. Abacus Press, Cambridge, 1988.
- [38] R. P. Lucht, D. W. Sweeney, and N. M. Laurendeau. Balanced cross-rate model for saturated molecular fluorescence in flames using a nanosecond pulse length laser. *Applied Optics* ;, 19(19):3295–3300, 1980.
- [39] J. P. Looney, G. J. Rosasco, L. A. Rahn, W. S. Hurst, and J. W. Hahn. Comparison of rotational relaxation rate laws to characterize the Raman Q-branch spectrum of CO at 295 K. *Chemical Physics Letters*, 161(3):232–238, 1989.
- [40] G. J. Rosasco, L. A. Rahn, W. S. Hurst, R. E. Palmer, and S. M. Dohne. Measurement and prediction of Raman Q-branch line self-broadening coefficients for CO from 400 to 1500 K. *Journal of Chemical Physics*, 90(8):4059–4068, 1989.
- [41] T. Nakazawa and M. Tanaka. Measurements of intensities and self- and foreign-gas-broadened half-widths of spectral lines in the CO fundamental band. *Journal of Quantitative Spectroscopy & Radiative Transfer*, 28(5):409–416, 1982.
- [42] J. M. Hartmann, L. Rosenmann, M. Y. Perrin, and J. Taine. Accurate calculated tabulations of CO line broadening by H₂O, N₂, O₂, and CO₂ in the 200–3000-K temperature range. *Applied Optics*, 27(15):3063–3065, 1988.
- [43] J.-P. Bouanich. *Journal of Quantitative Spectroscopy and Radiative Transfer*, 12:1609, 1972.
- [44] J. J. Belbruno, J. Gelfand, and H. Rabitz. Collision dynamical information from pressure broadening measurements: Application to carbon monoxide. *Journal of Chemical Physics*, 78(6):3990–3998, 1983.
- [45] P. L. Varghese and R. K. Hanson. Room-temperature measurements of collision widths of CO lines broadened by H₂O. *Journal of Molecular Spectroscopy*, 88(1):234–235, 1981.

- [46] R.J. Kee, F.M. Rupley, and J.A. Miller. Chemkin-II: A Fortran chemical kinetics package for the analysis of gas phase chemical kinetics. Technical Report SAND89-8009B, Sandia National Laboratories, 1992.
- [47] L. S. Rothman and L. D. G. Young. Infrared energy levels and intensities of carbon dioxide—II. *Journal of Quantitative Spectroscopy & Radiative Transfer*, 25(6):505–524, 1981.
- [48] B.J. Kirby and R.K. Hanson. CO₂ imaging using saturated planar laser-induced vibrational fluorescence. submitted to *Applied Optics*, 2001.
- [49] R. T. V. Kung and R. E. Center. High temperature vibrational relaxation of H₂O by H₂O, He, Ar, and N₂. *Journal of Chemical Physics*, 62(6):2187–2194, 1975.
- [50] G. D. Billing. Semiclassical calculation of energy transfer in polyatomic molecules. VII. Intra- and inter-molecular energy transfer in N₂ + CO₂. *Chemical Physics*, 67(1):35–47, 1982.
- [51] Gerhard Herzberg. *Molecular Spectra and Molecular Structure II. Infrared and Raman Spectra of Polyatomic Molecules*. Krieger, Malabar, 1945.
- [52] F. Rachet, M. Margottin-Maclou, A. Henry, and A. Valentin. *Q*-branch line mixing effects in the (20⁰0)_I ← 01¹0 and (12²0)_I ← 01¹0 bands of carbon dioxide perturbed by N₂, O₂, and Ar and in the 13¹0 ← 00⁰0 and 13¹0 ← 01¹0 bands of pure nitrous oxide. *Journal of Molecular Spectroscopy*, 175(2):315–326, 1996.
- [53] M. Margottin-Maclou, F. Rachet, C. Boulet, A. Henry, and A. Valentin. *Q*-branch line mixing effects in the (20⁰0)_I ← 01¹0 and (12²0)_I ← 01¹0 bands of carbon dioxide. *Journal of Molecular Spectroscopy*, 172(1):1–15, 1995.
- [54] R. Rodrigues, Gh. Blanquet, J. Walrand, B. Khalil, R. Le Doucen, F. Thibault, and J.-M. Hartmann. Line-mixing effects in *Q* branches of CO₂. I: Influence of parity in Δ ↔ Π bands. *Journal of Molecular Spectroscopy*, 186(2):256–268, 1997.

- [55] G. D. Billing. Semiclassical calculation of energy transfer in polyatomic molecules. XI. cross sections and rate constants for Ar+CO₂. *Chemical Physics*, 91(3):327–339, 1984.
- [56] C.S. McEnally, L.D. Pfefferle, A.M. Schaffer, M.B. Long, R.K. Mohammed, M.D. Smooke, and M.B. Colket. Characterization of a coflowing methane/air non-premixed flame with computer modeling, Rayleigh-Raman imaging, and on-line mass spectrometry. *Proceedings of the Combustion Institute*, 28, 2000, in press.
- [57] B. Yip, A. Lozano, and R. K. Hanson. Sensitized phosphorescence: a gas phase molecular mixing diagnostic. *Experiments in Fluids*, 17(1-2):16–23, 1994.
- [58] P. H. Paul and N. T. Clemens. Subresolution measurements of unmixed fluid using electronic quenching of NO $A^2\Sigma^+$. *Optics Letters*, 18(2):161–163, 1993.
- [59] G. F. King, R. P. Lucht, and J. C. Dutton. Quantitative dual-tracer planar laser-induced fluorescence measurements of molecular mixing. *Optics Letters*, 22(9):633–635, 1997.
- [60] J.B. Jeffries, R.A. Copeland, G.P. Smith, and D.R. Crosley. Multiple species laser-induced fluorescence in flames. *Proceedings of the Combustion Institute*, 21, 1986.
- [61] L. Doyennette, F. Menard-Bourcin, J. Menard, C. Boursier, and C. Camy-Peyret. Vibrational energy transfer in methane excited to $2\nu_3$ in CH₄-N₂/O₂ mixtures from laser-induced fluorescence measurements. *Journal of Physical Chemistry A*, 102(22):3849, 1998.
- [62] M. C. Thurber, F. Grisch, B. J. Kirby, M. Votsmeier, and R. K. Hanson. Measurements and modeling of acetone laser-induced fluorescence with implications for temperature-imaging diagnostics. *Applied Optics*, 37(21):4963–4978, 1998.
- [63] B.J. Kirby. unpublished data.
- [64] S. J. Brosnan and R. L. Byer. Optical parametric oscillator threshold and linewidth studies. *IEEE Journal of Quantum Electronics*, 15(6):415–431, 1979.

- [65] R. A. Baumgartner and R. L. Byer. Optical parametric amplification. *IEEE Journal of Quantum Electronics*, QE-15(6):432–444, 1979.
- [66] W. R. Bosenberg, L. K. Cheng, and J. D. Bierlein. Optical parametric frequency-conversion properties of KTiOAsO_4 . *Applied Physics Letters*, 65(22):2765–2767, 1994.
- [67] B. Boulanger, I. Rousseau, J. P. Feve, M. Maglione, B. Menaert, and G. Marnier. Optical studies of laser-induced gray-tracking in KTP. *IEEE Journal of Quantum Electronics*, 35(3):281–286, 1999.
- [68] L. Carrion and J. P. GirardeauMontaut. Gray-track damage in potassium titanyl phosphate under a picosecond regime at 532 nm. *Applied Physics Letters* ;, 77(8):1074–1076, 2000.
- [69] A. Deepthy, M. N. Satyanarayan, K. Rao, and H. L. Bhat. Photoluminescence studies on gray tracked KTiOPO_4 single crystals. *Journal of Applied Physics*, 85(12):8332–8336, 1999.
- [70] G. Millot and C. Roche. State-to-state vibrational and rotational energy transfer in CO_2 gas from time-resolved Raman-infrared double-resonance experiments. *Journal of Raman Spectroscopy*, 29(4):313–320, 1998.
- [71] J. L. Cooper and J. C. Whitehead. Rotational and vibrational energy transfer in CH ($\text{B}^2\Sigma^-$). *Journal of Physical Chemistry*, 98(34):8274–8278, 1994.
- [72] J. Luque, R. J. H. Klein-Douwel, J. B. Jeffries, and D. R. Crosley. Collisional processes near the $\text{CH B}^2\Sigma^-v' = 0, 1$ predissociation limit in laser-induced fluorescence flame diagnostics. *Applied Physics B*, 71(1):85–94, 2000.
- [73] M. R. Cherkasov. Broadening of overlapping spectral lines by pressure. I. *Optika I Spektroskopiya*, 40(1):7–13, 1976.
- [74] J.-M. Hartmann, R. Rodrigues, Nguyen-Van-Thanh, C. Brodbeck, C. Boulet, R. Le Doucen, N. Lacombe, and L. Bonamy. Temperature, pressure, and perturber

- dependencies of line-mixing effects in CO₂ infrared spectra. III. second order rotational angular momentum relaxation and coriolis effects in $\Pi \leftarrow \Sigma$ bands. *Journal of Chemical Physics*, 110(16):7733–7744, 1999.
- [75] B. Lavorel, G. Millot, R. Saint-Loup, H. Berger, L. Bonamy, J. Bonamy, and D. Robert. Study of collisional effects on band shapes of the $\nu_1/2\nu_2$ Fermi dyad in CO₂ gas with stimulated Raman spectroscopy. I. Rotational and vibrational relaxation in the $2\nu_2$ band. *Journal of Chemical Physics*, 93(4):2176–2184, 1990.
- [76] R. Rodrigues, B. Khalil, R. Le Doucen, L. Bonamy, and J.-M. Hartmann. Temperature, pressure, and perturber dependencies of line-mixing effects in CO₂ infrared spectra. I. $\Sigma \leftarrow \Pi$ Q branches. *Journal of Chemical Physics*, 107(11):4118–4132, 1997.
- [77] J. Boissoles, F. Thibault, R. Le Doucen, V. Menoux, and C. Boulet. Line mixing effects in the $00^0_3-00^0_0$ band of CO₂ in helium. II. Theoretical analysis. *Journal of Chemical Physics*, 100(1):215–223, 1994.
- [78] C. Boulet, J.-P. Bouanich, J.-M. Hartmann, B. Lavorel, and A. Deroussiaux. Line mixing in the ν_1 and $2\nu_2$ isotropic Raman Q-branch of CO₂ perturbed by argon and helium. *Journal of Chemical Physics*, 111(20):9315–9324, 1999.
- [79] J.-M. Hartmann and C. Boulet. Line mixing and finite duration of collision effects in pure CO₂ infrared spectra: Fitting and scaling analysis. *Journal of Chemical Physics*, 94(10):6406–6419, 1991.
- [80] F. Thibault, J. Boissoles, C. Boulet, L. Ozanne, J. P. Bouanich, C. F. Roche, and J. M. Hutson. Energy corrected sudden calculations of linewidths and line shapes based on coupled states cross sections: the test case of CO₂-argon. *Journal of Chemical Physics*, 109(15):6338–6345, 1998.
- [81] L. Bonamy, J. Bonamy, D. Robert, A. Deroussiaux, and B. Lavorel. A direct study of the vibrational bending effect in line mixing: the hot degenerate $11^1_0 \leftarrow 01^1_0$ transition of CO₂. *Journal of Quantitative Spectroscopy & Radiative Transfer*, 57(3):341–348, 1997.

- [82] B. Khalil, O. Cisse, G. Moreau, F. Thibault, R. Le Doucen, and J. Boissoles. Line mixing and line broadening in CO₂ bands perturbed by helium at 193 K. *Chemical Physics Letters*, 263(6):811–816, 1996.
- [83] J. Boissoles, C. Boulet, L. Bonamy, and D. Robert. Calculation of absorption in the microwindows of the 4.3 μm CO₂ band from an ECS scaling analysis. *Journal of Quantitative Spectroscopy & Radiative Transfer*, 42(6):509–520, 1989.
- [84] L. Bonamy, D. Robert, J. Boissoles, and C. Boulet. Determination of ECS scaling parameters for CO₂–CO₂ and CO₂–N₂. *Journal of Quantitative Spectroscopy & Radiative Transfer*, 45(5):305–308, 1991.
- [85] N. N. Filippov, J.-P. Bouanich, J.-M. Hartmann, L. Ozanne, C. Boulet, M. V. Tonkov, F. Thibault, and R. Le Doucen. Line-mixing effects in the 3ν₃ band of CO₂ perturbed by Ar. *Journal of Quantitative Spectroscopy & Radiative Transfer*, 55(3):307–320, 1996.
- [86] M. H. Alexander and A. E. DePristo. Adiabatically corrected sudden approximation for rotationally inelastic collisions between polar molecules. *Journal of Physical Chemistry*, 83(11):1499–1505, 1979.
- [87] S. Green, D. L. Cochrane, and D. G. Truhlar. Accuracy of the energy-corrected sudden (ECS) scaling procedure for rotational excitation of CO by collisions with Ar. *Journal of Chemical Physics*, 84(7):3865–3869, 1986.
- [88] L. L. Strow and B. M. Gentry. Rotational collisional narrowing in an infrared CO₂ Q-branch studied with a tunable-diode laser. *Journal of Chemical Physics*, 84(3):1149–1156, 1986.
- [89] M. Margottin-Maclou, A. Henry, and A. Valentin. Line mixing in the Q-branches of the ν₁ + ν₂ band of nitrous oxide and of the (11¹0)_I ← (02²0) band of carbon dioxide. *Journal of Chemical Physics*, 96(3):1715–1723, 1992.
- [90] T. Huet, N. Lacome, and A. Lévy. Line mixing effects in the Q branch of the 10⁰ ← 01¹0 transition of CO₂. *Journal of Molecular Spectroscopy*, 138(1):141–161, 1989.

- [91] R. Berman, P. Duggan, P. M. Sinclair, A. D. May, and J. R. Drummond. Direct measurements of line-mixing coefficients in the $\nu_1 + \nu_2$ Q branch of CO_2 . *Journal of Molecular Spectroscopy*, 182(2):350–363, 1997.
- [92] C. P. Rinsland and L. L. Strow. Line mixing effects in solar occultation spectra of the lower stratosphere: Measurements and comparisons with calculations for the 1932-cm^{-1} CO_2 Q branch. *Applied Optics*, 28(3):457–464, 1989.
- [93] B. Gentry and L. L. Strow. Line mixing in a N_2 -broadened CO_2 Q branch observed with a tunable diode laser. *Journal of Chemical Physics*, 86(10):5722–5730, 1987.
- [94] E. Arié, N. Lacome, P. Arcas, and A. Levy. Oxygen- and air-broadened linewidths of CO_2 . *Applied Optics*, 25(15):2584–2591, 1986.
- [95] L. Rosenmann, J. M. Hartmann, M. Y. Perrin, and J. Taine. Collisional broadening of CO_2 IR lines. II. Calculations. *Journal of Chemical Physics*, 88(5):2999–3006, 1988.
- [96] B. J. Orr and I. W. M. Smith. Collision-induced vibrational energy transfer in small polyatomic molecules. *Journal of Physical Chemistry*, 91(24):6106–6119, 1987.
- [97] C. Dang, J. Reid, and B. K. Garside. Detailed vibrational population distributions in a CO_2 laser discharge as measured with a tunable diode laser. *Applied Physics B-Photophysics and Laser Chemistry*, 27(3):145–151, 1982.
- [98] B.J. Kirby. FATKIN: Vibrational energy transfer database and solver using CHEMKIN. Technical Report 2001-001-1.0, Stanford University HTGL, 2001.
- [99] G. D. Billing and M. Cacciatore. On the importance of multiquantum VV transitions in CO. *Chemical Physics Letters*, 94(2):218–221, 1983.
- [100] G. D. Billing and E. R. Fisher. VV and VT-rate coefficients in N_2 by a quantum-classical model. *Chemical Physics*, 43(3):395–401, 1979.
- [101] R.C. Millikan and D.R. White. Systematics of vibrational relaxation. *Journal of Chemical Physics*, 39(12):3209–3213, 1963.

- [102] M. Cacciatore and G. D. Billing. Semiclassical calculation of VV and VT rate coefficients in CO. *Chemical Physics*, 58(3):395–407, 1981.
- [103] M.A. Kovacs and M.E. Mack. *Applied Physics Letters*, 20:487, 1972.
- [104] G. D. Billing and R. E. Kolesnick. Vibrational relaxation of oxygen. State to state rate constants. *Chemical Physics Letters*, 200(4):382–386, 1992.
- [105] D. C. Allen, T. J. Price, and C.J.S.M. Simpson. Vibrational deactivation of the bending mode of CO₂ measured between 1500 K and 150 K. *Chemical Physics Letters*, 45(1):183–187, 1977.
- [106] J. Taine, F. Lepoutre, and G. Louis. Photoacoustic study of collisional deactivation of CO₂ by N₂, CO, and O₂ between 160 K and 375 K. *Chemical Physics Letters*, 58(4):611–615, 1978.
- [107] F. Lepoutre, G. Louis, and J. Taine. Photoacoustic study of intra-molecular energy transfer in CO₂ deactivated by monatomic gases between 153 K and 393 K. *Journal of Chemical Physics*, 70(5):2225–2235, 1979.
- [108] H. T. Powell. Vibrational relaxation of carbon monoxide using a pulse discharge. II. T=100, 300, 500 K. *Journal of Chemical Physics*, 63(6):2635–2645, 1975.
- [109] Stephenson and Moore. 1972.
- [110] T. G. Kreutz, J. A. O’Neill, and G. W. Flynn. Diode laser absorption probe of vibration-vibration energy transfer in CO₂. *Journal of Physical Chemistry*, 91(22):5540–5543, 1987.
- [111] M. Cacciatore, M. Capitelli, and G. D. Billing. Theoretical semiclassical investigation of the vibrational relaxation of CO colliding with ¹⁴N₂. *Chemical Physics*, 89(1):17–31, 1984.
- [112] J. C. Stephenson and E. R. Mosburg. Vibrational energy transfer in CO from 100 to 300 °K. *Journal of Chemical Physics*, 60(9):3562–3566, 1974.

- [113] D. C. Allen and C.J.S.M. Simpson. Vibrational energy exchange between CO and the isotopes of N₂ between 300 K and 80 K. *Chemical Physics* ;, 45(2):203–211, 1980.
- [114] T. C. Price, D. C. Allen, and C.J.S.M. Simpson. Vibrational deactivation of CO ($v = 1$) by O₂ measured between 300 and 80 K. *Chemical Physics Letters*, 53(1):182–184, 1978.
- [115] R. G. Miller and J. K. Hancock. V-V energy transfer in H₂-additive gas mixtures using a stimulated raman vibrational fluorescence technique. *Journal of Chemical Physics*, 66(11):5150–5158, 1977.
- [116] A. J. Andrews and C.J.S.M. Simpson. Vibrational deactivation of CO by *n*-H₂, by *p*-H₂ and by HD measured down to 77 K using laser fluorescence. *Chemical Physics Letters*, 41(3):565–569, 1976.
- [117] H. Matsui, E. L. Resler, and S. H. Bauer. Vibrational relaxation in H₂-CO and D₂-CO mixtures, measured via stimulated Raman-IR fluorescence. *Journal of Chemical Physics*, 63(10):4171–4176, 1975.
- [118] G. E. Caledonia, B. D. Green, and R. E. Murphy. Study of the vibrational level dependent quenching of CO($v = 1-16$) By CO₂. *Journal of Chemical Physics*, 71(11):4369–4379, 1979.
- [119] B. S. Wang, Y. S. Gu, and F. N. Kong. Multilevel vibrational-vibrational (V-V) energy transfer from CO(v) to O₂ and CO₂. *Journal of Physical Chemistry A*, 102(47):9367–9371, 1998.
- [120] B. Wang, Y. Gu, and F. Kong. Rapid vibrational quenching of CO(V) by H₂O and C₂H₂. *Journal of Physical Chemistry A*, 103(37):7395–7400, 1999.